Università degli Studi di Cagliari

Facoltà di Ingegneria
Dipartimento di Ingegneria Meccanica

Dottorato di Ricerca in Progettazione Meccanica
XXI ciclo – SSD: ING-IND/14

Esame finale – A.A. 2007/2008

SIMULATION OF DELAMINATION IN COMPOSITE MATERIALS UNDER STATIC AND FATIGUE LOADING BY COHESIVE ZONE MODELS

Tesi di dottorato di:
Agostino Cerioni

Relatori:
Prof. Ing. Pierluigi Priolo
Prof. Ing. Francesco Aymerich

Coordinatore del dottorato:
Prof. Ing. Filippo Bertolino

Abstract

This thesis is a dissertation focussing on the mechanics of delamination in laminated composites. Delamination, which is one of the most critical forms of failure in composite materials, may occur as a result of many causes and different types of loading, such as, for example, static or cyclic loading.

This work presents an examination of the potential of cohesive interface elements for the prediction of delamination propagation under quasi-static mode I, mode II and mixed mode (I and II) loading, by a comparison between experimental tests and parametric analyses in order to evaluate the sensitivity of the elements to some parameters. The results of the comparison show that a rather good accordance may be obtained between experimental data and numerical simulations with a proper choice of the main model parameters.

Moreover, a simplified mathematical model (cylinder model) for the study of fatigue driven delamination is described. This model is particularly useful for investigating the performance of various formulations of interface elements that are used to simulate delamination under cyclic loading, because of its simplicity and efficiency that allow evaluating a large number of sets of parameter values. The model has been studied with different static constitutive laws and damage definitions, coupled with a particular fatigue degradation strategy. In particular, the sensitivity of the model, with the different proposed constitutive laws, has been evaluated with respect to some key parameters, such as the distance between the springs and the size of the increment in the number of loading cycles.

Acknowledgements

I wish to thank my tutor Prof. Pierluigi Priolo for guiding my attempts to develop this PhD work. I have learned a lot from his suggestions.

I wish to express my sincere gratitude for my tutor Prof. Francesco Aymerich for his constant support and confidence in my work in the hard times too.

I would like to thank Prof. Ugo Galvanetto and Prof. Paul Robinson who have offered me the opportunity to work for seven months at the Department of Aeronautics at the Imperial College of London. This placement has been very important for my PhD working and for my forming.

I am grateful to the Course Coordinator Prof. Filippo Bertolino and to all the staff of the Department of Mechanical Engineering at the University of Cagliari for its helpfulness and kindness.

Contents

Chapter 1

Introduction

1.1 Motivation and scope

The use of composite materials for structural applications is widely common and advanced composite materials have progressively replaced traditional materials due to their better specific properties. Initially, these materials were exclusively used in advanced applications, like aerospace and aeronautical industries. Successively, these materials started to be used in many different applications, due to technological developments and reduction of manufacturing costs. Some of these applications, besides aircraft and space vehicles, include biomedical implants, pipes, components of automotive vehicles, small boats, etc..

Over the past twenty years, in the general industrial sector, an important increase in the use of this type of materials -especially polymeric matrix materials reinforced with glass or carbon fibres- has taken place, since they offer excellent stiffness to weight and strength to weight ratios, which make them very attractive for many applications.

The wide use and diffusion of composite materials require a good knowledge of their behaviour and of their failure mechanisms, which are quite complex and need to be carefully investigated.

One of the most critical forms of failure in laminated composites is delamination, which is a separation between the layers that can occur as a result of many causes, such as manufacturing defects, geometric discontinuities, plies drop-offs, free-edge stress singularities and transverse impact.

Delamination can be the result of quasi-static or cyclic loading and different approaches are usually required for its study depending on the type of involved loadings.

One of the most used current approaches for the study of the delamination under quasi-static loading is the modelling by cohesive interface elements.

One aim of this work is to examine the potential of cohesive interface elements for the prediction of delamination propagation under quasi-static mode I, mode II and mixed mode (I and II) loading, by a comparison between experimental tests and parametric analyses in order to evaluate the sensitivity of the elements to some parameters.

Cyclic loading may induce fatigue-driven delamination in laminate composite structures. Simulation of fatigue-driven delamination in laminated composites can be performed with different strategies based on the use of interface finite elements. Usually, when a strategy has to be studied, a large number of finite element simulations are required in order to evaluate the sensitivity of the strategy to the main parameters.

A simplified mathematical model for the study of delamination under fatigue loading has been developed [LGR07] to investigate the effect of the cohesive law parameters without interaction with other parts of a mesh and without the complications of a finite element model. The aim is to implement this model in a programming language and to evaluate its response with respect to different constitutive laws, damage formulations and other key parameters.

1.2 Outline of the thesis

In this thesis different aspects of the delamination in laminated composites are presented: generalities, modes of delamination, experimental tests, approaches to the study of delamination under quasi-static and fatigue loading. The dissertation is divided in chapters, each of which examines one of the previous topics.

In chapter 2 a brief introduction on laminates made of composite materials is presented. Their general properties are described and the main modalities of failure, in particular delamination, under quasi-static and fatigue loading are presented.

Chapter 3 examines the possible approaches to study delamination under quasi-static and fatigue loading.

In order to predict the propagation of interlaminar damage under quasi-static loading, the most adopted fracture mechanics approach is the Virtual Crack Closure Technique (VCCT), proposed by Rybicki and Kanninen [RK77]. The use of the VCCT technique has however several disadvantages. First of all it requires some previous knowledge on the shape and location of the initial crack. Moreover complex procedures must be applied to regenerate the mesh at the crack front during delamination growth in real-life structures [T03].

To overcome these disadvantages, other approaches have been proposed, like interface finite elements based on cohesive damage models [CD02]. It is based on the cohesive approach proposed by Dugdale [D60] and Barenblatt [B62] and used by Needleman [N87].

The cohesive damage model assumes the presence of a process zone ahead of the physical crack tip. This zone is delimited by upper and lower cohesive surfaces, held together by cohesive tractions.

The relative displacements of the cohesive surfaces are related to the cohesive tractions by a constitutive law. The constitutive law describes the accumulation of damage through the delamination growth in the process area. Cohesive zone models combine the application of a strength criterion, used to predict the onset of decohesion, with energy-based fracture mechanics tools, utilized to model the progression of damage up to complete fracture. The formulation of the cohesive elements of Camanho and Davila is the one that is implemented in the finite element code Abaqus, used in this thesis and quickly described in this chapter.

In this chapter some generalities on the approaches to study delamination under fatigue loading are also exposed. The most common approach is represented by the Paris law [PGA61], [PE63], which is a semi-empirical approach. This law has been used for some strategies to study the fatigue as the one described in the chapter 6 of this thesis [RGTBV05].

Chapter 4 describes some typical experimental tests of fracture mechanics carried out under quasi-static loading in order to have a comparison with the finite element modelling adoptive the cohesive elements.

Unidirectional 24-ply graphite/epoxy laminates, manufactured by a vacuum bag-hot press technique, were tested. In particular, DCB (Double Cantilever Beam) [A94], 4ENF (4-points End Notched Flexure) [ACB02] and SLB (Single Leg Bending) [DS96] fracture tests were conducted in order to achieve stable propagation of delamination under pure mode I, pure mode II and mixed mode, respectively. The DCB and the 4ENF test were also conducted in order to calculate the interlaminar fracture toughness for the pure mode I and mode II, respectively.

In chapter 5 the results of the experimental data collected during the series of experimental analyses described in the previous chapter are finally compared to a numerical analysis in order to assess the quality of numerical predictions.

The modelling of the same tests carried out by experimental analyses (DCB, 4ENF and SLB) has been performed for comparison with experiments under pure mode I, pure mode II and mixed mode, respectively. The analyses were carried out with the commercial finite element software Abaqus 6.5, and the explicit solver available in Abaqus was chosen in order to obtain the finite element solution avoiding convergence problems and numerical instabilities typical of implicit solutions in the presence of significant material nonlinearities.

A two-parameter bilinear cohesive law was used in the study to define the interfacial behaviour under both mode I and mode II loadings. A stress-based quadratic criterion was used to identify the onset of the decohesion phase, while a linear interaction criterion was assumed to describe the dependence of the fracture energy on the mixed-mode ratio.

The analyses showed that a rather good accordance may be obtained between experimental data and numerical simulations with a proper choice of the main model parameters, in particular critical fracture energies for the mode I and mode II, interface stiffness and mesh density.

Finally, chapter 6 describes the implementation in a programming language of a simple mathematical model [LGR07] developed in order to permit a fast and rational evaluation of the performance of interface elements for fatigue induced delamination. This model, implemented in this thesis (not involved in any finite element mesh) allows to isolate the interface element from the interaction with the rest of the model and to focus the attention on the most important aspects of modelling fatigue-driven delamination, which are the constitutive laws, the damage definitions and the fatigue degradation strategies.

The model consist in two zero-thickness layers, initially coincident, one fixed and one adhered to a cylinder, to which the load, or displacement, is applied. The two layers are connected with springs with a chosen constitutive law. It is then possible to apply both static and cyclic loads to the cylinder and also to apply different constitutive laws to the springs. This simple mathematical model is extremely efficient, from a computational point of view, and then it is possible to perform a large number of runs in a short time. This allows making parametric studies with a large number of parameters or combinations of them.

First of all the behaviour of the model under quasi-static loading has been studied, in particular with respect to the sensitivity of the model to different constitutive laws, to different formulations of the damage and to some key parameters, such as the distance between the springs.

Finally, the strategy of study of the fatigue proposed by Robinson et al. [RGTBV05] has been implemented in the model and the sensitivity of the model has been evaluated, with respect to the constitutive law, to the formulation of the damage and to the sensitivity of the model to the distance between the springs and the increment of the number of cycle until the total applied number of cycles.

Chapter 2

Introduction to composite materials, delamination and fatigue

2.1 Composite materials

This section explains the general characteristics of the composite materials. An unambiguous definition of composite materials does not exist, but they can be defined as materials, obtained from the combination of two or more materials, whose properties are different from the single components. These materials consist of two or more physically and/or chemically distinct, suitably arranged or distributed phases, with an interface separating them.

Most commonly, composite materials have a bulk phase, which is continuous, called the matrix, and one dispersed phase, non-continuous, called the reinforcement, which is usually harder and stronger and with smaller dimensions.

The essence of the concept of composites is this: the bulk phase accepts the load over a large surface area, and transfers it to the reinforcement, which, being stiffer, increases the strength of the composite. The significance here lies in that there are numerous matrix materials and as many fibre types, which can be combined in countless ways to produce just the desired properties.

The shape and dimensions of the reinforcement constituent are very important in order to determine the mechanical properties of the composite. The properties of composites are strongly influenced by the proportions and properties of its constituents and also by the interface between the constituents.

The fibres of a fibrous composite material are embedded into the matrix. In this case the reinforcement has a very small cross-section respect to its length. The ratio between the length and a cross section dimension is called aspect ratio.

The aspect ratio of the reinforcement permits the classification of a fibrous composite material. It can be defined continuous, for long fibres with high aspect ratios, and discontinuous, for short fibres with low aspect ratios. Fibres can be natural or synthetic and the synthetic fibres can be organic or inorganic.

It is very important the orientation of the fibres, that can be random or preferred. This last case, in the eventuality of long fibres, is called unidirectional. The fibres can be also used, as reinforcement, like a fabric, and in this case they are called bidirectional. Unidirectional and woven fibre composites are usually manufactured in single-layered sheets or lamina that can be flat or curved.

Often the fibrous material is made of a group of laminas, which are superimposed in a particular sequence and bonded together, by using the same matrix material of the lamina, and they are then called laminates. In the laminates the orientation of the fibres can change from layer to layer to give the structural element particular properties.

2.2 Delamination

2.2.1 Characterisation of delamination

Composite laminates are subjected to different types of failure. The fracture process is quite complex and it involves intralaminar damage mechanisms, like matrix cracking or fibre fracture, and interlaminar damage, which is the delamination.

Delamination is a frequent type of failure in laminated composite.

The reason of this is that in those materials there is not any reinforcement in the direction of the thickness. Delamination can happens in consequence of an impact or a manufacturing defect and can cause a remarkable reduction of the capacity of a structure to carry a load.

The study of delamination is usually approached by the analysis of its two components: the onset of delamination and its propagation when already started. The analysis of the first point is based on the study of the interaction of the interlaminar stresses, whereas, in the prediction of the propagation, fracture mechanic approaches are usually considered, in order to avoid problems due to the singularity of the stresses in the tip of the crack. The study of both the previous components of delamination will be explained in chapter 3.

After the onset of delamination, the fracture can propagate in different modes, as shown in figure 2.1.

These failure modes can be classified as mode I, which is the opening component, mode II, the shear component perpendicular to the delamination front and mode III, which is the shear component parallel to the delamination front.

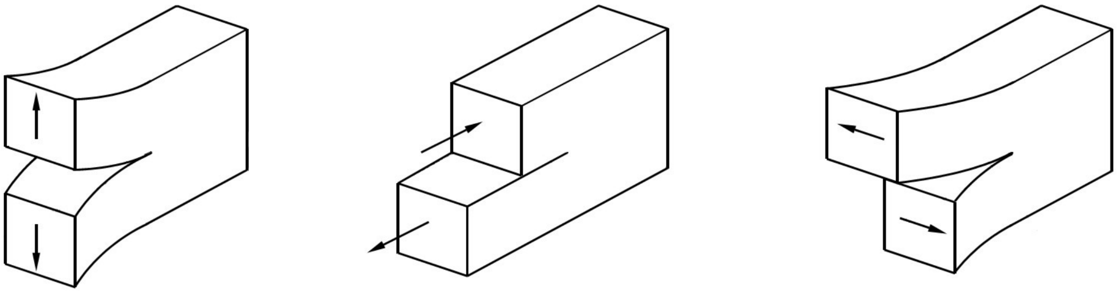

Mode I **Mode II** **Mode III**

Figure 2.1 – Mode I, mode II and mode III crack propagation modes

A fracture not necessarily propagates as a single fracture mode but it can do it as a combination of them. When more than one mode of fracture is present, this is known as mixed mode.

2.2.2 Fatigue loading

Delamination can happen also when a structure is subjected to cyclic loading. In this case the damage and fracture of the material is called fatigue failure.

Delamination under fatigue conditions basically involves the same micro mechanisms and processes that happen under static loading, that means that there is also an initiation or onset process of the delamination and a crack growth or propagation process due to the fatigue loading.

Usually cyclic loading is assumed as sinusoidal stress or strain cycles of constant amplitude. The parameters that describe these cycles, as shown in figure 2.2, are the frequency, which is the inverse of the period *T*, the maximum stress (σ_{max}), the minimum stress (σ_{min}), the mean stress (σ_m) and the amplitude (σ_a).

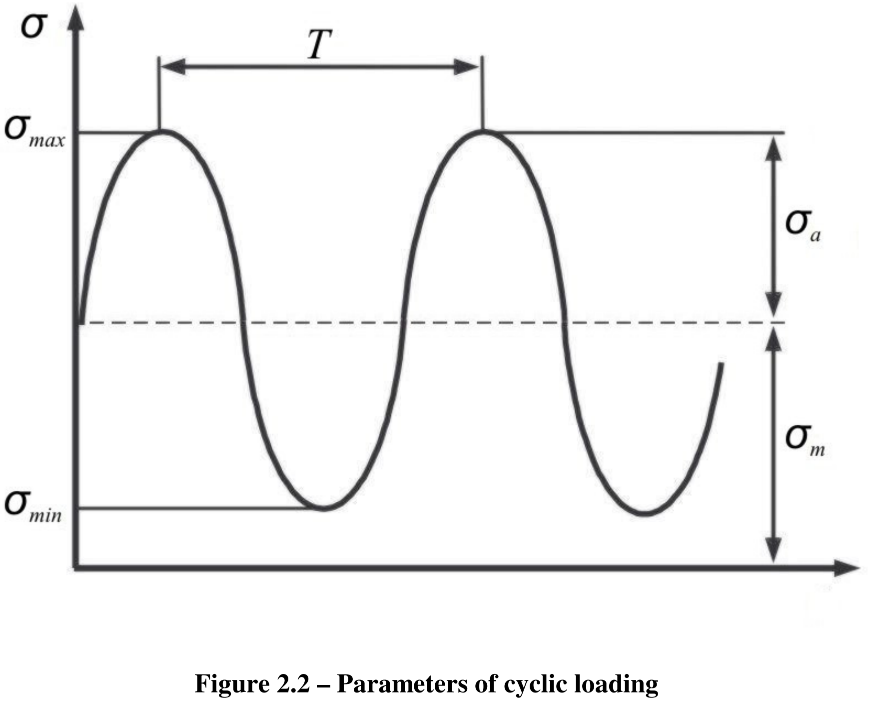

Figure 2.2 – Parameters of cyclic loading

Another parameter that has to be defined is the stress ratio (*R*), which is defined as the ratio of the minimum to the maximum stress during a load cycle.

Two different regimes are possible in the cyclic loading:

- Low-cycle fatigue
- High-cycle fatigue

In the low-cycle fatigue the level of the stress is high and the number of cycles to failure is quite low, that means from hundreds to thousands.

The high-cycle fatigue, instead, is characterised by low stress level and a large number of cycles to failure, usually millions.

Under fatigue loading, composites materials go through various stages.

The first stage is characterised by matrix cracking and fibre breaking. The second stage has coupling of cracks with interfacial debonding as well as fibre breaking. The third stage is where delamination appears in addition to fibre breaking. In the fourth stage delamination growth is present along with localised fibre breaking. The fifth and last stage is where there is gross fracture of the entire material.

Chapter 3

Cohesive interface elements in the finite element method

3.1 Approaches to delamination

3.1.1 Fracture mechanics

The approach to delamination of the Linear Elastic Fracture Mechanics (LEFM) has been proven to be reliable in predicting the propagation of delamination when the nonlinearities are negligible.

One of the methods of the Linear Elastic Fracture Mechanics used to predict the crack growth after the onset of the delamination is the Virtual Crack Closure Technique (VCCT), proposed by Rybicki and Kanninen [RK77]. This technique is based on Irwin's assumption that when the crack increases of a small quantity, the energy used to let the crack propagate is equal to the work required to close the crack to its initial length, and the energy release rate can therefore be calculated from the nodal forces and displacements evaluated with a finite element model. This method becomes more effective and reliable when the mesh is refined enough and when the elements at the tip of the crack have the same dimension in the direction of the propagation of the crack. In this case, the energy release rate can be obtained from one analysis only.

Anyway, this method and other methods of the linear fracture mechanics present difficulties when they are implemented in a finite elements code. The reason is that the parameters necessary to predict the fracture, the release energy rate or the stress intensity factor, have to be evaluated from variable of nodes located before and after the crack front. When the crack is stationary it is not difficult to evaluate these quantities, whereas when progressive crack propagation is studied their calculation becomes complex.

3.1.2 Cohesive zone model

Different approaches were developed in order to be able to study delamination without the limitations of the VCCT method. One of these is the use of interfacial decohesion elements, which are put between the layers of composite materials.

These elements use failure criteria that combine aspects of strength based analysis to predict the onset of the softening process at the interface and fracture mechanics to predict delamination propagation. A difference of the use of decohesion elements, which is an advantage with respect to the VCCT method, is that the cohesive zone model has the capability to predict both onset and propagation of the delamination, without knowing the location of the crack and the direction of propagation.

Many types of decohesion has been proposed before, continuous interface elements and point decohesion elements, but a common feature of all them is that they do not have any interaction criterion to predict the softening onset under mixed-mode loading and they use simplified interaction criteria of the energy release rate for the prediction of the propagation of delamination. However, experimental evidence shows that the fracture toughness for some types of resin depends on the mode ratio and cannot be described with a simplified expression [R92] and then could be better not to use simplified expressions to study the propagation of delamination under mixed-mode loading conditions.

The formulation of the cohesive zone model used in this work is the theory of Camanho and Davila [CD02]. These elements are zero-thickness volumetric decohesion elements that are able to capture delamination onset and propagation under mixed-mode loading conditions. The concept of cohesive element is based on the cohesive approach of Dugdale [D60] and Barenblatt [B62], initially applied to the fracture mechanics, and it was also used by Needleman [N87] in order to describe the fast crack growth in brittle materials.

Needleman considered useful cohesive zone models especially when the strengths of the interface are relatively weak compared with the surrounding material, as in the case of composite laminates. The constitutive equations proposed to describe the behaviour of the interface are phenomenological mechanical relations between the relative separations of the interfaces and the tractions that oppose to these displacements.

The relation between the tractions and the displacements is such that, increasing the separation between the interfaces, the tractions reach a maximum, then decrease, and finally they become equal to zero. This behaviour is shown in figure 3.1.

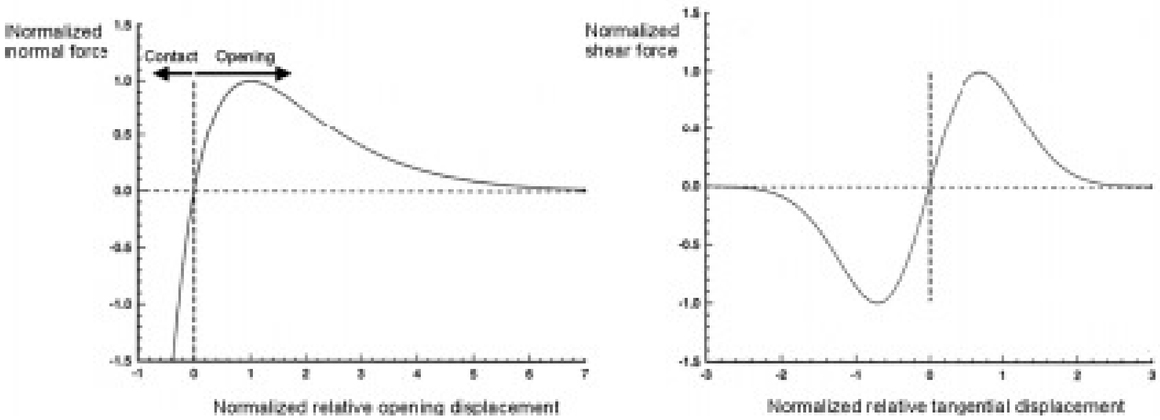

Figure 3.1 – Normal and shear stress in the cohesive interface versus the relative displacement

The work done of normal separation and tangential separation can be related to the critical values of energy release rates. In fact, the cohesive zone formulation is identical to Griffith's theory of fracture. It is possible to consider the integral J proposed by Rice [R68], that it is represented by the following equation.

$$J = \int_{\Gamma} \left(w dy - T \frac{\partial u}{\partial x} ds \right) \tag{3.1}$$

In the equation 3.1, Γ is a curve that surrounds the tip of the crack; *u* is the vector of the displacements; *T* is the traction vector defined accordingly to the outward normal along Γ; *w*, finally, is the strain energy density.

Considering as Γ the contour of the cohesive zone it s possible to write the equation 3.1 in the following way:

$$J = \int_{\Gamma} \left(w dy - \sigma(\delta) \frac{d\delta}{dx} dx \right) \tag{3.2}$$

Considering that $dy = 0$ in the chosen contour Γ, the equation 3.2 becomes:

$$J = -\int_{\Gamma} \left(\sigma(\delta) \frac{d\delta}{dx} dx \right) = -\int_{\Gamma} \frac{d}{dx} \left(\int_{0}^{\delta} \sigma(\delta) d\delta \right) dx = \int_{0}^{\delta_t} \sigma(\delta) d\delta \tag{3.3}$$

The displacement δ_t is the relative displacement at the tip of the crack.

It is demonstrable that, for cracks with the same characteristics of growth and negligible cohesive zone, it is possible to express the *J*-integral as the rate of decrease of the potential energy with respect to the crack length and this is equivalent to the energy release rate [R68], as shown in the following equation:

$$J = -\frac{\partial \Pi}{\partial a} = G \tag{3.4}$$

where Π is the potential energy of the system. By equating the 3.3 and the 3.4:

$$G = \int_{0}^{\delta_t} \sigma(\delta) d\delta \tag{3.5}$$

If a displacement $\delta_t = \delta_{max}$ is considered, the value of the energy release rate is $G = G_C$, and the equation 3.5 become:

$$G_C = \int_0^{\delta_{\max}} \sigma(\delta) d\delta \tag{3.6}$$

The cohesive zone, after the onset of the delamination, which in figure 3.2 is shown as point 3, is still able to transfer load until the critical value of the release energy rate is reached. This is represented by the point 4 in the figure 3.2.

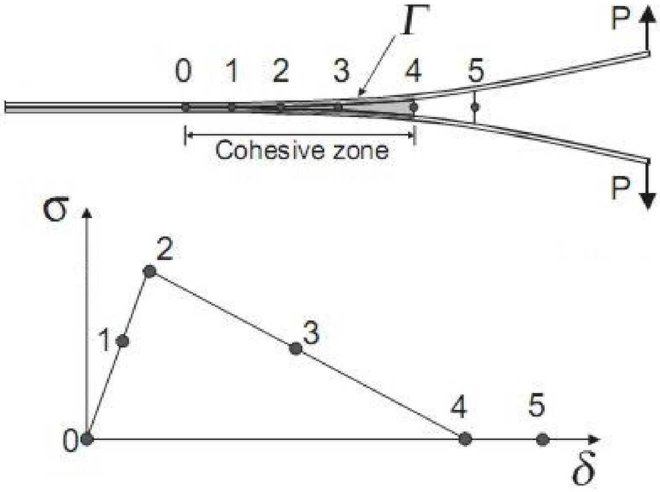

Figure 3.2 – Cohesive zone around the tip crack

Constitutive law under single mode delamination

In the formulation of the cohesive elements it is fundamental the choice of the constitutive law. Many laws have been proposed, other than the one proposed by Needleman [N87] and shown in figure 3.1. One of the most used is the bilinear constitutive law shown in figure 3.2, which presents linear elastic and linear softening behaviour.

The linear elastic branch has usually a steep slope, given in order to avoid big separations between the two faces of the crack in the elastic field. As figure 3.3 shows, after that the interlaminar or tensile or shear strength is reached, the stiffness decrease until the stress become equal to zero. The area under the curve is, for the mode I, II and III, respectively, the critical value of the release energy rate.

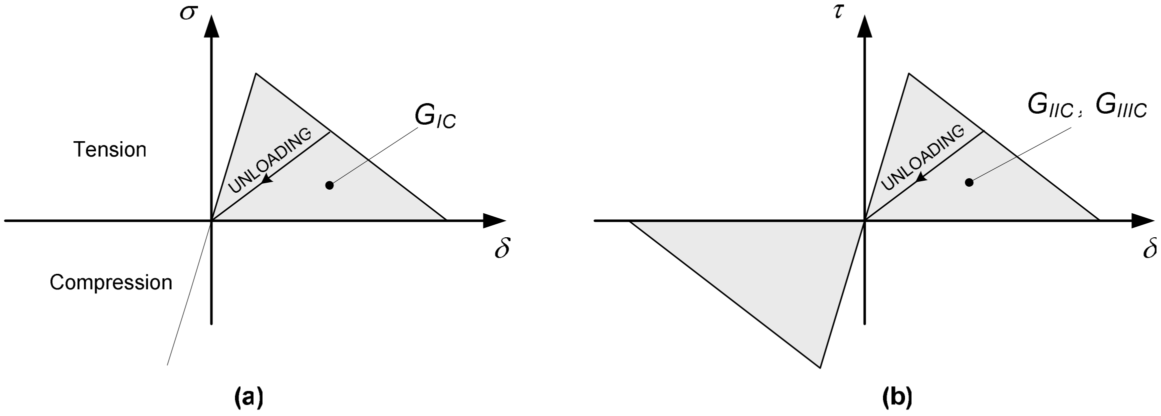

Figure 3.3 – Cohesive law for the mode I, mode II and mode III

These quantities are named, respectively, G_{IC}, G_{IIC} and G_{IIIC}, and they can be evaluated by the following expressions:

$$G_{IC} = \int_{0}^{\delta_{\max,3}} \sigma_{33}(\delta) d\delta_3 \tag{3.7}$$

$$G_{IIC} = \int_{0}^{\delta_{\max,2}} \tau_{13}(\delta) d\delta_2 \tag{3.8}$$

$$G_{IIIC} = \int_{0}^{\delta_{\max,1}} \tau_{23}(\delta) d\delta_1 \tag{3.9}$$

In the previous equations, σ_{33}, τ_{13} and τ_{23} are the stress in the relevant mode. To completely define the response of the model it is therefore necessary to define, for each mode, the slope of the elastic branch, the maximum stress and the energy release rate.

Once the penalty stiffness has become equal to zero and then the crack is not able to react to any load, the penetration between the two faces of the crack has to be avoided.

This is a contact problem that can be solved by applying again the normal penalty stiffness when contact between the two faces is detected.

The constitutive law, shown in figure 3.4, can be expressed as following.

- For $\delta_i < \delta_{0,i}$ the constitutive law is given by:

$$\sigma = \begin{bmatrix} K_P & 0 & 0 \\ 0 & K_P & 0 \\ 0 & 0 & K_P \end{bmatrix} \delta = K\delta \tag{3.10}$$

- For $\delta_{0,i} \le \delta_i < \delta_{\max,i}$ the constitutive law is given by:

$$\sigma = (I - E)K\delta \tag{3.11}$$

  where *I* is the identity matrix *E* is a diagonal matrix defining the position of the integration point in the softening curve.

- For $\delta_i \ge \delta_{\max,i}$ the penalty stiffness become equal to zero and, as said before, if there is again compenetration between parts the initial stiffness is re-applied.

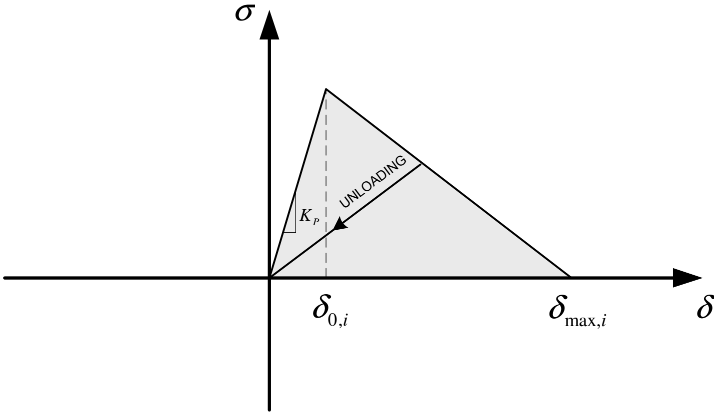

Figure 3.4 – Bilinear constitutive law

The application of the normal stiffness, in case of penetration between the faces, is typical of solution procedures of contact problems that use penalty methods in a constrained variational formulation.

The accuracy of this type of analysis depends on the value of penalty stiffness K_P chosen for the linear-elastic branch of the constitutive law. If the value is high, there will be not penetration between the faces of the crack, but probably there will be numerical problems. The problem of finding a relation between the value of K_P and the characteristics of the interface has been studied by many authors. For example, Daudeville et al. [DAL95] assumed that the interface was a zone of small thickness and rich of resin. Indicating with e_i the thickness of the interface, the expression of the interface stiffness, for each mode, is the following:

$$K_P^I = \frac{E_3}{e_i} \qquad K_P^{II} = \frac{2G_{13}}{e_i} \qquad K_P^{III} = \frac{2G_{23}}{e_i} \tag{3.12}$$

where G_{13}, G_{23} and E_3 are the elastic modules of the interface.

The last thing that has to be defined is the response of the constitutive law with respect to the unloading. One assumption that looks reasonable, proposed by many authors, for example Crisfield [CCKBMQ99], is assuming that, with reversing strains, the material unloads directly toward the origin, as shown in figure 3.4.

Constitutive law under mixed mode delamination

Delamination growth, in the most common structural applications of the composite materials, usually happens under mixed mode loading. For this reason could be useful a formulation of the cohesive interface elements that is able to predict the crack growth under mixed mode. Some formulations have been proposed, like the one of O'Brien et al. [O98]. This formulation proposes using a cubic equation obtained from least square regression curve fit of the experimental data.

The development of a theory like this usually requires expensive tests, or the analysis of lots of empirical expressions, in order to be considered reliable.

A study of failure criteria under mixed-mode delamination in brittle epoxy, tough epoxy and thermoplastic composites under the full mixed-mode loading was performed by Reeder [R92, R93]. Some of the evaluated criteria are shown below.

- Linear criterion:

$$\left(\frac{G_I}{G_{IC}}\right)+\left(\frac{G_{II}}{G_{IIC}}\right)=1 \tag{3.13}$$

- Power law criterion:

$$\left(\frac{G_I}{G_{IC}}\right)^{\alpha}+\left(\frac{G_{II}}{G_{IIC}}\right)^{\beta}=1 \tag{3.14}$$

- Bilinear criterion:

$$G_I=\xi G_{II}+G_{IC} \tag{3.15}$$

The previous criteria were assessed by using experimental data from mixed-mode bending tests, which were used to measure the mixed-mode delamination toughness of the composites. The linear model appears to be the most advisable in order to in predict the failure of thermoplastic PEEK matrix composites, because the results were close to more sophisticated criteria. The linear criterion was instead found to be not very accurate in order to predict the failure in epoxy composite materials [CDA01].

3.2 Fatigue crack growth

The approach of the fracture mechanic to the fatigue consists in relating the energy release rate (G) or the stress intensity factor (K) with the growth of the delamination.

It is possible to define the stress intensity factor range and the energy release rate range as following:

$$\Delta K = K_{\max} - K_{\min} = (1 - R)K_{\max} \tag{3.16}$$

$$\Delta G = G_{\max} - G_{\min} = (1 - R^2)G_{\max} \tag{3.17}$$

where R is the stress ratio, as defined in the paragraph 2.2.2, K_{max} and G_{max} are the values of the stress intensity factor and of the release energy rate, respectively, related to the maximum value of the stress in the loading cycle (σ_{max}), as defined in the paragraph 2.2.2, and K_{min} and G_{min} are related to the minimum value of the stress in the loading cycle (σ_{min}).

The fatigue crack growth rate is defined as the crack extension per number of cycles (N), and it is defined by dA/dN, where A indicates the area of the crack.

The correlation between the release energy ratio, or the stress intensity factor, and the growth of the crack has been found experimentally and it is possible to represent it in a log-log diagram. This diagram, as shown in figure 3.5, has a sigmoidal behaviour and can be considered divided in three regions. The first region from the left, the Region I, is characterised from a threshold value of G, or K, which are respectively named G_{th} and K_{th}. Under these values there is not any propagation of the crack, whereas immediately after there is a quick growth of the crack. At this point the Region II starts. This region is characterised by a stable propagation of the crack and the curve, in this region, is generally linear. In the Region III, instead, the curve rises to an asymptote corresponding to the critical value of the fracture toughness, that can be expressed as G_c or K_c.

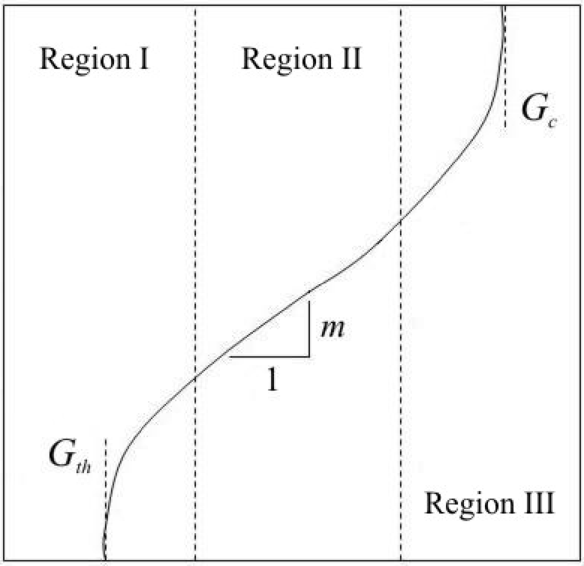

Figure 3.5 – Correlation between energy release rate and crack growth rate

Different empirical or semi-empirical laws have been developed in order to describe this curve. The most actually used is the Paris law [PGA61, PE63], which describes only the linear part of the curve, and correlates the crack growth rate to the energy release rate range as following:

$$\frac{dA}{dN} = C\left(\frac{\Delta G}{G_c}\right)^m \tag{3.18}$$

where C and m are constants that depend on the material and on the stress ratio, and are usually experimentally determined. The exponent m describes the slope of the curve, whereas ΔG and G_c are the ones just defined above. The equation 3.18 can also be expressed in terms of stress intensity factor range ΔK.

Another fatigue damage evolution law has been proposed by Peerlings et al. [PBDG00], called Paris law. This law is exponential and requires the definition of three parameters that can be adjusted to fit with experimental data. This law allows the damage to grow after a certain number of cycles. It will be described better and used in chapter 6.

3.3 Numerical implementation

3.3.1 Analysis type

All the finite element analyses presented in this work are performed with the element finite code ABAQUS 6.5, of the ABAQUS Inc.

The ABAQUS code is formed by different parts. The first is an interactive environment, ABAQUS/CAE, utilized to create finite element models, submit ABAQUS analyses, monitor and diagnose jobs, and evaluate results. There is also a visualization module, ABAQUS/Viewer, which is a subset of ABAQUS/CAE that contains only the postprocessing capabilities. Finally, there are two different solvers, ABAQUS/Standard and ABAQUS/Explicit.

ABAQUS/Standard is a general-purpose solver using a traditional implicit integration scheme to solve finite element analyses.

ABAQUS/Explicit, instead, the only utilized in this work, uses an explicit integration scheme to solve highly nonlinear transient dynamic and quasi-static analyses.

The explicit dynamics procedure performs efficiently a large number of small time increments, using an explicit central-difference time integration rule. Each increment is therefore relatively less expensive than the direct-integration dynamic analysis procedure used by ABAQUS/Standard, because there is not the necessity to solve a set of simultaneous equations. The explicit central-difference operator satisfies the dynamic equilibrium equations at the beginning of the increment t and the accelerations calculated at the time t are used to advance the velocity solution to time $t+\Delta t/2$ and the displacement solution to time $t+\Delta t$.

In particular, the explicit dynamics analysis procedure is based upon the implementation of an explicit integration rule together with the use of diagonal element mass matrices. The equations of motion for the body are integrated using the explicit central-difference integration rule

$$\dot{u}^N_{(i+1/2)} = \dot{u}^N_{(i-1/2)} + \frac{\Delta t_{(i+1)} + \Delta t_{(i)}}{2} \ddot{u}^N_{(i)} \tag{3.19}$$

$$u^N_{(i+1)} = u^N_{(i)} + \Delta t_{(i+1)} \dot{u}^N_{(i+1/2)} \tag{3.20}$$

where u^N is a degree of freedom, which can be a displacement or a rotation component, and the subscript i refers to the increment number in an explicit dynamics step.

The central-difference integration operator is explicit in the sense that the kinematic state is advanced using known values of $\dot{u}^N_{(i-1/2)}$ and $\ddot{u}^N_{(i)}$ from the previous increment.

The explicit integration rule is quite simple but it is not the only reason of the computational efficiency of the explicit dynamics procedure. The main reason of the computational efficiency of the explicit procedure is the use of diagonal element mass matrices, because the accelerations at the beginning of the increment are computed by

$$\ddot{u}^N_{(i)} = \left(M^{NJ}\right)^{-1}\left(P^J_{(i)} - I^J_{(i)}\right) \tag{3.21}$$

where M^{NJ} is the mass matrix, P^J is the applied load vector, and I^J is the internal force vector.

A lumped mass matrix is used because its inverse is simple to compute and because the vector multiplication of the mass inverse by the inertial force requires only n operations, where n is the number of degrees of freedom in the model. The explicit procedure requires no iterations and no tangent stiffness matrix. The internal force vector (I^J) is assembled from contributions from the individual elements such that a global stiffness matrix need not be formed.

The stability of this procedure requires some explanations. The explicit procedure integrates through time by using many small time increments. The central-difference operator is conditionally stable, and the limit of stability Δt_{cr} for the operator is given in terms of the highest frequency of the system. Without considering damping, the expression of the limit of stability is the following:

$$\Delta t_{cr} \leq \frac{2}{\omega_{\max}} \tag{3.22}$$

An approximation to the stability limit is often written as the smallest transit time of a dilatational wave across any of the elements in the mesh:

$$\Delta t_{cr} \approx \frac{L_e}{C_d} \tag{3.23}$$

where L_e is the characteristic element dimension in the mesh and C_d is the dilatational wave speed in the element, defined, for an isotropic elastic material, as

$$C_d = \sqrt{\frac{\lambda_0 + 2\mu_0}{\rho}} \tag{3.24}$$

In the equation 3.24, ρ is the density of the material, whereas λ_0 and μ_0 are the effective Lamé's constants, which for an isotropic elastic material are defined as following:

$$\lambda_0 = \frac{E\nu}{(1+\nu)(1-2\nu)} \tag{3.25}$$

$$\mu_0 = \frac{E}{2(1+\nu)} \tag{3.26}$$

where E is the Young's modulus and v is the Poisson's ratio.

Replacing the 3.25 and the 3.26 in the 3.24, and considering a material with Poisson's ratio equal to zero, the expression of C_d became:

$$C_d = \sqrt{\frac{E}{\rho}} \tag{3.27}$$

Finally, the equation 3.27 of the stability limit can be rewritten as following:

$$\Delta t_{cr} \approx L_e \sqrt{\frac{\rho}{E}} \tag{3.28}$$

The time increment used in an analysis must be smaller than the stability limit of the central-difference operator. Failure to use a small enough time increment will result in an unstable solution. When the solution becomes unstable, the time history response of solution variables such as displacements will usually oscillate with increasing amplitudes and the total energy balance will also change significantly. Anyway the estimate value for Δt_{cr} obtained from equation 3.28 is only approximate and in most cases is not a safe estimate. ABAQUS/Explicit offers many possibilities to manage the time increment: it is possible to let the code decide or vary it automatically or it is possible to introduce a value.

3.3.2 Constitutive cohesive law for the mixed mode

This paragraph describes the constitutive law related to the cohesive elements implemented in ABAQUS.

A cohesive zone consists of an upper and a lower surface held by cohesive tractions existing ahead of the crack tip. The cohesive tractions are related to the separation displacement between the cohesive surfaces by a constitutive law.

The following description is valid for bonded interfaces where the interface thickness is negligibly small, as the ones used in this work.

The constitutive response of the ABAQUS cohesive elements is represented by a traction-separation model that assumes initially linear elastic behaviour followed by the initiation and evolution of damage.

The elastic behaviour is described by an elastic constitutive matrix that relates the nominal stresses to the nominal strains across the interface. The nominal stresses are the force components divided by the initial area at each integration point. The nominal strains, instead, are the separations divided by the initial thickness at each integration point.

The value assigned by default to the initial constitutive thickness is 1.0, which ensures that the nominal strain is equal to the relative displacements of the top and bottom faces of the element. The constitutive thickness used for traction-separation response is typically different from the geometric thickness, which is usually close or equal to zero.

The nominal traction stress vector, t, consists of three components, that became two components in two-dimensional problems: t_N, t_S, and, in three-dimensional problems, t_T.

Those components represent respectively the normal and the two shear tractions and the corresponding separations are δ_N, δ_S and δ_T.

Denoting by T_0 the original thickness of the cohesive element, the nominal strains can be defined as following:

$$\varepsilon_N = \frac{\delta_N}{T_0} \qquad \varepsilon_S = \frac{\delta_S}{T_0} \qquad \varepsilon_T = \frac{\delta_T}{T_0} \tag{3.29}$$

It is clear, from the previous expressions, that, using the initial constitutive thickness $T_0 = 1$, the nominal strain components are equal to the respective components of the relative displacement between the top and bottom of the cohesive layer.

The elastic behaviour can then be expressed with the following:

$$t = \begin{Bmatrix} t_N \\ t_S \\ t_T \end{Bmatrix} = \begin{bmatrix} K_{NN} & K_{NS} & K_{NT} \\ K_{NS} & K_{SS} & K_{ST} \\ K_{NT} & K_{ST} & K_{TT} \end{bmatrix} = \begin{Bmatrix} \varepsilon_N \\ \varepsilon_S \\ \varepsilon_T \end{Bmatrix} = \mathrm{K}\,\varepsilon \tag{3.30}$$

The elasticity matrix (K) gives then the relationships between all components of the traction vector and separation vector.

ABAQUS/Explicit allows modelling of progressive damage and failure in cohesive layers whose response is defined in terms of traction-separation. The details of the damage modelling for traction-separation response are presented below.

Different types of damage are implemented, but they have some points in common. Each failure mechanism consists of three parts: a damage initiation criterion, a damage evolution law, and a choice of element removal when a completely damaged state is reached.

The first part of the failure mechanism is the initiation criterion. The initial response of the cohesive element is assumed to be linear, as discussed above. However, once a damage initiation criterion is met, material damage can occur according to a user-defined damage evolution law. The process of degradation begins when the stresses or strains satisfy certain imposed damage initiation criteria.

One of the available criteria, the one chosen for this work, is the quadratic nominal stress criterion. Denoting by *N*, *S* and *T* the peak values of the nominal stress when the deformation is either purely normal to the interface or purely in the first or the second shear direction respectively, this criterion assumes that the damage initiates when a quadratic interaction function involving the nominal stress ratios, as defined in the equation 3.31, reaches a value of one. This criterion can be represented as

$$\left(\frac{\langle t_N \rangle}{N}\right)^2 + \left(\frac{t_S}{S}\right)^2 + \left(\frac{t_T}{T}\right)^2 = 1 \tag{3.31}$$

where the operator $\langle \ \rangle$ is defined as following:

$$\langle x \rangle = \begin{cases} o & x \le 0 \\ x & x > 0 \end{cases} \tag{3.32}$$

This operator means that the cohesive layer does not undergo damage under pure compression.

The three other criteria available in ABAQUS, not used in this work, are the following:

- Maximum nominal stress criterion.

  The damage is assumed to initiate when the maximum nominal stress ratio, as defined in the equation 3.33, reaches a value of one. This criterion can be expressed by the following relationship:

$$\max\left\{\frac{\langle t_N \rangle}{N}, \frac{t_S}{S}, \frac{t_T}{T}\right\} = 1 \tag{3.33}$$

- Maximum nominal strain criterion.

  The damage is assumed to initiate when the maximum nominal strain ratio, as defined in the equation 3.34, reaches a value of one. This criterion can be expressed by the following relationship:

$$\max\left\{\frac{\langle\varepsilon_N\rangle}{\varepsilon_N^0},\frac{\varepsilon_S}{\varepsilon_S^0},\frac{\varepsilon_T}{\varepsilon_T^0}\right\}=1 \tag{3.34}$$

where ε_N^0, ε_S^0 and ε_T^0 represent the peak values of the nominal strain when the deformation is either purely normal to the interface or purely in the first or the second shear direction, respectively.

- Quadratic nominal strain criterion.

  The damage is assumed to initiate when a quadratic interaction function involving the nominal strain ratios, as defined in the equation 3.35, reaches a value of one. This criterion can be expressed by the following relationship:

$$\left(\frac{\langle\varepsilon_N\rangle}{\varepsilon_N^0}\right)^2+\left(\frac{\varepsilon_N}{\varepsilon_S^0}\right)^2+\left(\frac{\varepsilon_N}{\varepsilon_T^0}\right)^2=1 \tag{3.35}$$

If a damage initiation criterion is specified without a corresponding damage evolution law, the code will evaluate the damage initiation criterion, but there will be no effect on the response of the cohesive element and no damage will occur.

The second part of the failure mechanism is the damage evolution law, which describes the rate at which the material stiffness is degraded once the corresponding initiation criterion is reached.

A scalar damage variable (*D*) represents the overall damage in the material and captures the combined effects of all the active mechanisms. It initially has a value equal to 0. If damage evolution is modelled, *D* monotonically evolves from 0 to 1 upon further loading after the initiation of damage. The way in which the damage operates on the stress components of the traction-separation model is described by the following expressions:

$$t_N = \begin{cases} (1-D)\bar{t}_N & \bar{t}_N \geq 0 \\ \bar{t}_N & otherwise \end{cases} \tag{3.36}$$

$$t_S = (1-D)\bar{t}_S \tag{3.37}$$

$$t_T = (1-D)\bar{t}_T \tag{3.38}$$

where $\bar{t}_N$, $\bar{t}_T$ and $\bar{t}_T$ are the stress components predicted by the elastic traction-separation behaviour for the current strains without damage.

To describe the evolution of damage under a combination of normal and shear deformation across the interface, it is useful to introduce an effective displacement [CD02] defined as following:

$$\delta_m = \sqrt{\left\langle \delta_N^2 \right\rangle + \delta_S^2 + \delta_T^2} \tag{3.39}$$

Another variable is introduced, which give a measure of the mode mix of the deformation fields in the cohesive zone, in order to quantify the relative proportions of normal and shear deformation. One of the methods available in ABAQUS is based on energy. Denoting by G_I, G_{II} and G_{III} the work done by the tractions and their conjugate relative displacements in the normal, first, and second shear directions, respectively, and defining $G_T = G_I + G_{II} + G_{III}$, it is possible to express the mode-mix definitions as following, remembering that two only of the three quantities are independent:

$$m_1 = \frac{G_I}{G_T} \qquad m_2 = \frac{G_{II}}{G_T} \qquad m_3 = \frac{G_{III}}{G_T} \tag{3.40}$$

In order to completely describe the evolution of damage two components have to be defined.

The first component that has to be specified is either the effective displacement at complete failure, δ_m^f, relative to the effective displacement at the initiation of damage, δ_m^0, both defined in reference [CD02], or the energy dissipated due to failure, G_C, defined later by the equation 3.42. All the previous quantities are shown in figure 3.6.

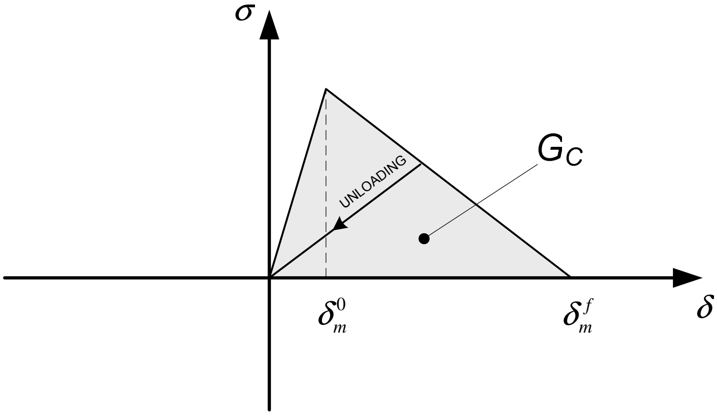

Figure 3.6 – Typical traction-separation response

In the eventuality that the energy dissipated is chosen to define the first component, there are some criteria to describe the dependence of the fracture energy on the mode mix.

One of those is the 'power law criterion', which states that failure under mixed-mode conditions is governed by a power law interaction of the energies required to cause failure in the individual, normal and two shear, modes. The expression of the law is the following:

$$\left\{\frac{G_I}{G_{IC}}\right\}^{\alpha}+\left\{\frac{G_{II}}{G_{IIC}}\right\}^{\alpha}+\left\{\frac{G_{III}}{G_{IIIC}}\right\}^{\alpha}=1 \qquad (3.41)$$

where the exponent is chosen typically equal to $\alpha=1$ or $\alpha=2$.

In the equation 3.41 the quantities G_I, G_{II} and G_{III}, refer to the work done by the traction and its conjugate relative displacement in the normal, the first, and the second shear directions, respectively. The quantities G_{IC}, G_{IIC} and G_{IIIC} are the critical fracture energies required to cause failure in the normal, the first, and the second shear directions, respectively.

When the condition expressed by the equation 3.41 is satisfied, the energy dissipated due to failure in the mixed mode is given by the following:

$$G_C = G_I + G_{II} + G_{III} \tag{3.42}$$

The second component that have to be defined is the specification of the evolution of the damage variable, *D*, between the onset of the damage and final failure. This can be done by either defining linear or exponential softening laws.

For linear softening, as shown in figure 3.6, ABAQUS uses an evolution of the damage variable, *D*, that reduces, in the case of damage evolution under a constant mode mix, to the expression proposed by Camanho and Davila, expressed by

$$D = \frac{\delta_m^f \left(\delta_m^{\max} - \delta_m^0\right)}{\delta_m^{\max}\left(\delta_m^f - \delta_m^0\right)} \tag{3.43}$$

In the above expression, $\delta_m^{\max}$ refers to the maximum value of the effective displacement attained during the loading history.

Figure 3.7 shows a schematic representation of the dependence of damage initiation and evolution on the mode mix, for a traction-separation response with isotropic shear behaviour. The figure shows the traction on the vertical axis and the magnitudes of the normal and the shear separations along the two horizontal axes. The unshaded triangles in the two vertical coordinate planes represent the response under pure normal and pure shear deformation, respectively. All intermediate vertical planes, that contain the vertical axis, represent the damage response under mixed mode conditions with different mode mixes.

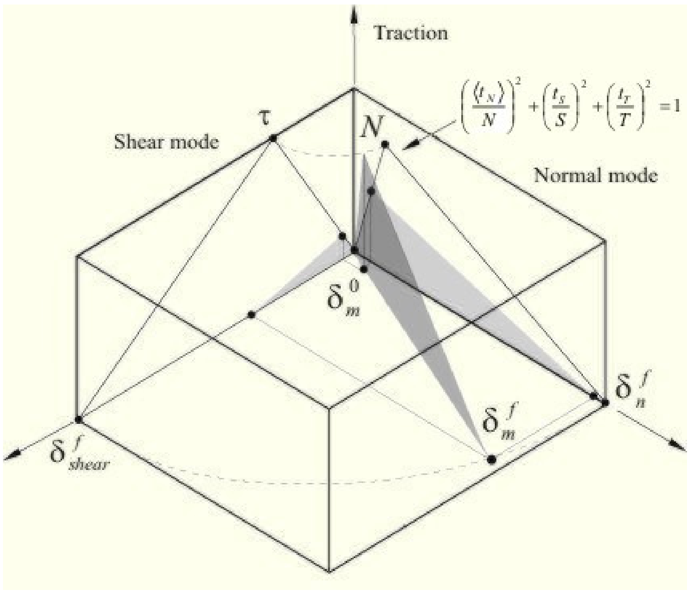

Figure 3.7 – Mixed mode response in cohesive elements

The third and last part of the failure mechanism is the choice of element removal, or deletion, when a completely damaged state is reached. The upper limit to the overall damage variable for the mixed mode at a material point is, by default of ABAQUS, $D = 1$, and once this maximum overall damage variable is reached at all of its material points and none of its material points are in compression, the cohesive elements are removed, that means deleted. Once removed, the cohesive elements offer also no more resistance to subsequent penetration of the components.

Chapter 4

Experimental tests

4.1 Introduction

The experimental tests were carried out in order to evaluate some parameters of the used materials and in order to have a good starting point for the subsequent comparison with the finite element modelling with cohesive elements.

Three typologies of typical test of fracture mechanics have been carried out, each one related to a particular mode of propagation of the crack.

The first type of test carried out is the DCB (Double Cantilever Beam) test [A94], related to the failure pure mode I. The second type is the 4ENF test [ACB02], a flexural test that let the propagation happen in pure mode II. The last type of test is the SLB test [DS96], a flexural test in which the delamination happens in a mixed mode.

From each test two curves have been obtained: the force versus displacement curve and the displacement versus crack length curve.

The DCB test and the 4ENF test are two of the tests that permit to evaluate the interlaminar toughness of the material for the mode I and mode II respectively, therefore this quantity has been evaluated from each of those tests.

4.2 Materials and specimens manufacturing

This section describes the materials used in the experimental tests and the modalities that were adopted in order to realize the specimens.

The specimens were manufactured from uniaxial pre-preg plies made of carbon fibres and a matrix of epoxy resin.

The mechanical characteristics of each component of the composite material were not known at the beginning of the tests. Thus the characteristic of the entire composite material have been determined directly on the realized specimens.

The specimens were cut from square panels with the side of 200 mm.

The panels were realized using a hand-layup process.

Each panel is made of twenty four plies, all with the fibres oriented in the same direction. The thickness of each ply is 0.15/0.17 mm.

The plies have been laid one above the others manually and after the application of each layer the group of layers has been pressed by hand with a little roller.

The crack, for all the specimens, is in the middle of their thickness, with twelve plies on each side. In order to generate the initial crack a ply of aluminium film has been put between the two groups of twelve plies for the predetermined initial length of the crack. This fact did not allow the two groups of layers to paste each other in that area during the consolidation. The resulting crack can be seen in figure 4.1.

The aluminium film has been ironed in order to eliminate each wrinkle.

As just said, all the plies have the same orientation, except the layers immediately above and under the crack. To those two layers an orientation of ± 5° has been given, in order to avoid that the fibres in the expected propagation area were exactly parallel to each other. This expedient has been used in order to limit the influence of the bridging in the tests.

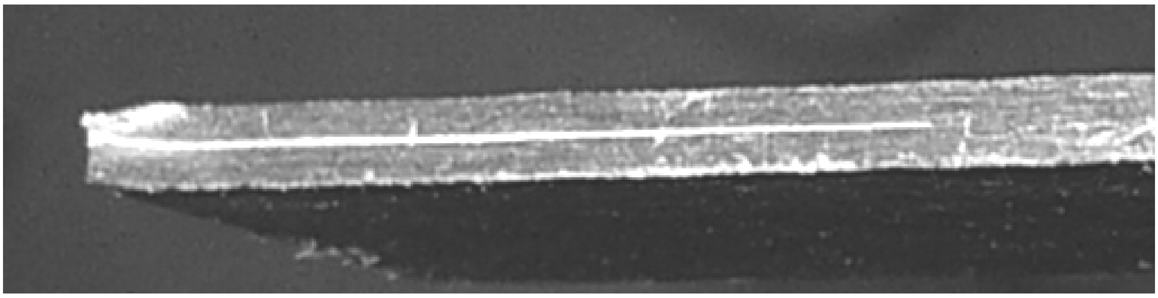

Figure 4.1 – Crack formed with an aluminum insert

After the layup process, each panel was consolidated with a lamination process under hot press and vacuum bag.

The press used for the consolidation, shown in figure 4.2, was a hydraulic press with a heated plate.

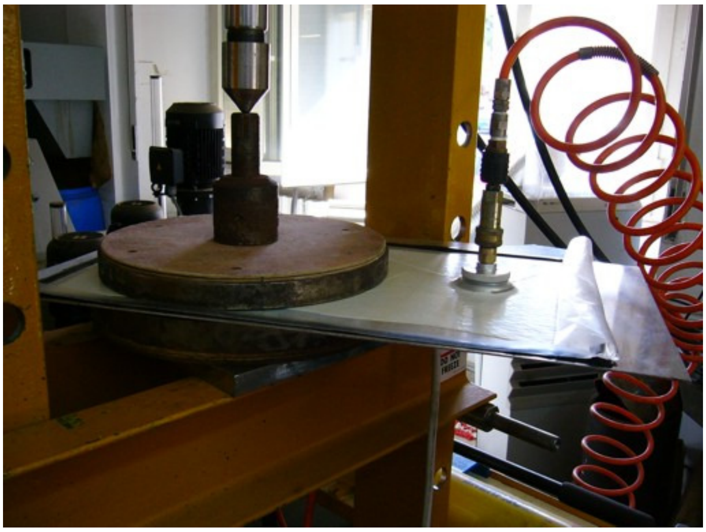

Figure 4.2 – Press used for the consolidation process

A pressure of 8 bar was applied to the panel. Part of this pressure (7 bar) was applied by the press, whereas the remaining pressure (1 bar) was due to the aspiration pump of the vacuum bag.

Figure 4.3 shows the path of the temperature and the pressure that have been used for the consolidation process.

The pressure of the press has been kept constant from the beginning of the consolidation until the end of the cooling. The pump of the vacuum bag has been instead turned off as soon as the beginning of the cooling path. The aim of the aspiration is to avoid the formation of air bubbles inside the matrix, that are not more eliminable after the end of the consolidation process and they make worst the mechanical characteristics of the laminate.

The temperature, instead, firstly has been increased constantly until the value of 90 °C. As soon as it reached this value, it has been kept constant for thirty minutes and then it has been increased again until the maximum value of 125 °C, which has been kept constant for 180 minutes.

The temperature has been checked every fifteen minute, in order to ensure the repeatability of the process.

After this, the heating has been turned off, letting the panel cooling until the temperature reached again the environmental value.

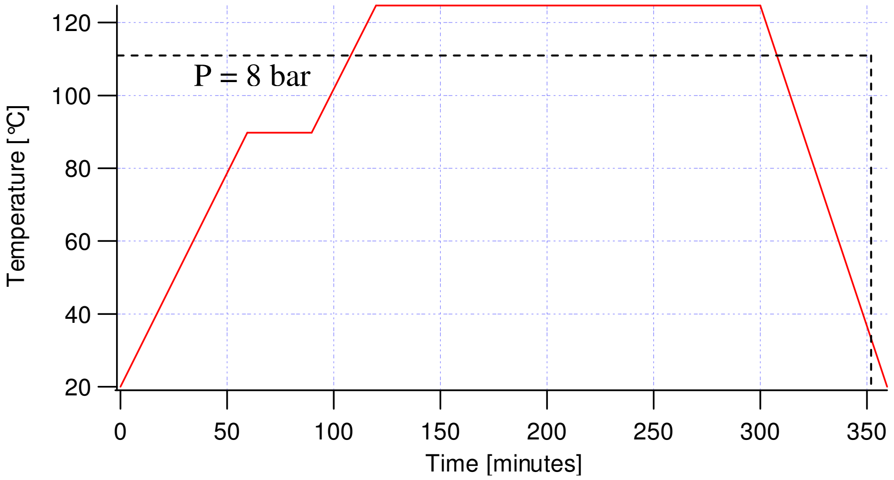

Figure 4.3 - Consolidation path

The duration of the consolidation process was four hours at all.

After the process, the panels were removed from the press and the fringes of resin that went out from the panel due to the pressure were removed.

At this point specimens of the desired measure were cut from the panels, always in the same direction of the fibres, in order to obtain an angle of the fibre of 0°, and catalogued.

Five panels were realized in the previous way. Another panel was realized without the aluminium insert, in order to obtain some specimens without crack, to evaluate, through simple tests, the most important mechanical characteristics of the entire composite material, principally the elastic modulus in the fibres direction.

From the tests made with this last panel without crack, an elastic modulus in the direction of the fibres of 130 GPa was obtained.

4.3 Common aspects of the tests

Aim of each test is to evaluate the length of the crack of a specimen and to correlate it to the load and the displacement of that specimen.

The characteristics of each test will be explained in the relevant paragraph of this chapter. However the tests have some aspects in common that are discussed in this paragraph.

For all the tests the Galdabini test machine shown in the figure 4.4 was used. With this machine it is possible to carry out traction, compression and, with the relevant gear, flexural tests, until a maximum load of 5000 N. The machine is able to give, as output, the load, the displacement of the specimen for an assigned number of intervals and the time related to each of these points.

Figure 4.4 – Galdabini test machine

Correlating the length of the crack with the load was not simple, because the machine is not able to measure directly the length of the crack. The solution was to let the machine measuring the load and the displacement of the specimen and, on the other side, to follow the delamination by recording it with a camcorder.

It was necessary, at the beginning of each test, to take a reference time in order to correlate the time of the test machine and the time of the camcorder. In this way it was possible to examine the result of the test and to correlate the load to the length of the crack in a second time.

The camcorder, with its support, is shown in the figure 4.5.

Figure 4.5 – Camcorder used to follow the propagation of the crack

Another problem was to see the position of the tip of the crack with acceptable precision. The side of each specimen is in fact of a dark colour, making difficult to follow the propagation of the crack.

After many trials, the solution was to put a layer of white paint on the observed side of the specimen and covering both the initial crack and the propagation area. This layer had to be very thin and very brittle. The small thickness allowed the paint to break following exactly the crack of the specimen, making possible to observe the position of the tip of the crack.

In order to evaluate in every instant the distance of the tip of the crack from its initial position, a piece of graph paper was put both on the top and on the bottom of the specimen, as shown in the figure 4.6.

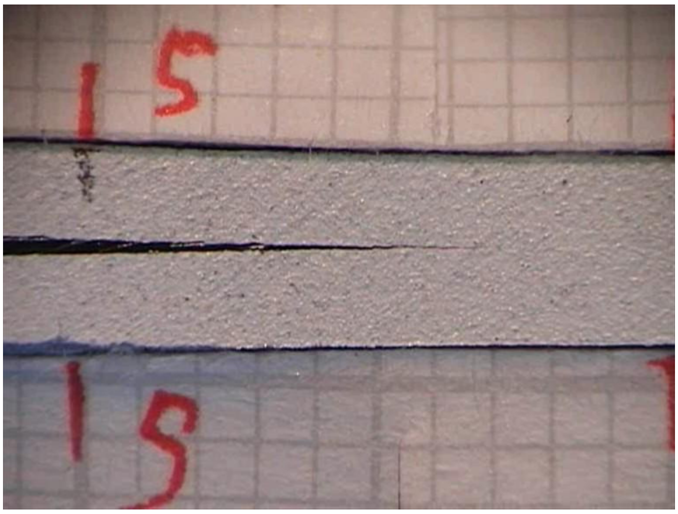

Figure 4.6 – Graph paper and white paint on the side of the specimen

Each specimen, as said in the paragraph 4.2, has 24 layers, unidirectional, with the angle of the orientation of the fibers equal to 0°. Only the two layers above and under the crack have an angle of orientation equal to ± 5°, in order to limit the phenomenon of bridging.

It is important to say something about the denomination of each specimen. For the aim of this work six panels have been done at all, and from each panel have been cut the specimens.

The name of each specimen is formed from the letter P, which means “Panel”, followed by a number, which indicates the number of the panel in the order in which it has been done. The previous abbreviation is followed by a dash and by another number that indicates the order in which the specimen have been cut, starting from the left of the panel after having put the panel on an horizontal plan with its rough surface upward and the side of the panel without the crack toward the person who is looking it.

4.4 Mode I test (DCB)

4.4.1 Generality of the test

The DCB (Double Cantilever Beam) test is one of the most common tests used to evaluate the mode I interlaminar fracture toughness in a composite laminate.

This test is coded from the ASTM D5528-94a [A94] and it considers a composite beam with an initial delamination crack. The initial delamination is forced to open by applying a force or a displacement that pull the two beams of the specimen away from each other. In this way, each arm of the specimen is loaded like a cantilever beam in which the span length increases as the delamination grows.

As it is possible to see in the figure 4.7(a), the test starts with a specimen with an initial crack (a_0) and the two arms of the crack closed.

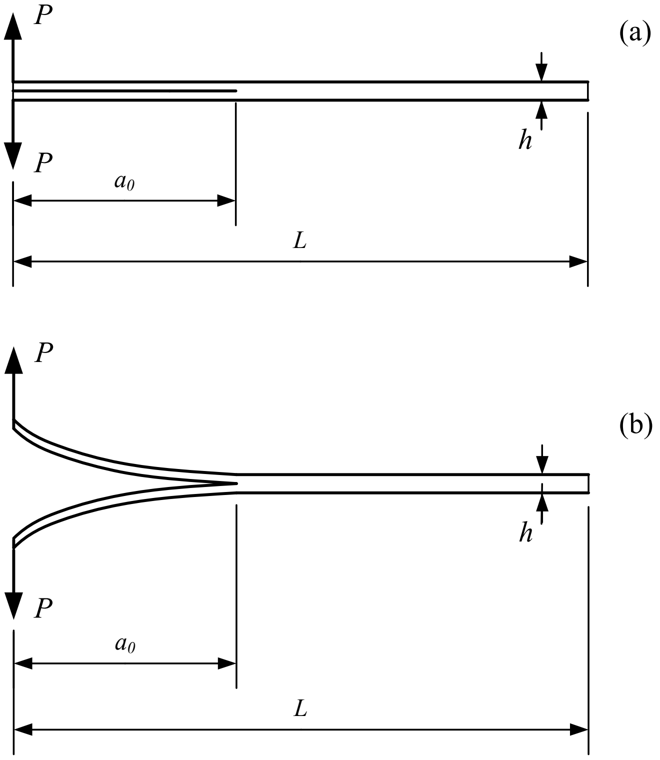

Figura 4.7 – Configuration of the DCB test

Figure 4.7(b) shows the deformed configuration of the specimen during the test.

Aim of this test is the evaluation of the interlaminar fracture toughness for the pure mode I (G_{IC}).

According to the beam theory approach, for any mode of propagation of the crack the following expression is valid:

$$G = \frac{P^2}{2w}\frac{dC}{da} \tag{4.1}$$

The mode I energy release rate, as a function of the applied load, and the compliance for the DCB test can be respectively determined as

$$G_I = \frac{P^2 a^2}{wEI} \tag{4.2}$$

$$C = \frac{\delta}{P} = \frac{2a^3}{3EI} \tag{4.3}$$

where P is the load, δ is the displacement, a is the actual length of the crack, E is the axial modulus of the laminate, I is the inertial modulus, and w is the width of the specimen. Combining the previous both expressions, an expression for the energy release rate as a function of the displacement can be obtained as

$$G_I = \frac{9EI\delta^2}{4wa^4} \tag{4.4}$$

that can also be written as

$$G_I = \frac{3P\delta}{2wa} \tag{4.5}$$

The ASTM D5528 – 94a [A94], the version of the standard used for doing the tests, prescribes three methods, based on the beam theory, to do the data reduction for calculating the fracture toughness.

These methods, described in the standard, are: the modified beam theory (MBT), the compliance calibration method (CC) and the modified compliance calibration method (MCC).

As the ASTM says, none of the three methods is clearly superior to the other and then for the data reduction of the test was chosen the compliance calibration method (CC), which is the most popular in literature.

The compliance calibration (CC) method consist in calculating the fracture toughness as

$$G_I = \frac{nP\delta}{2wa} \tag{4.6}$$

where n is a corrective parameter calculated as following.

The calculation of n starts from evaluating the compliance of the specimen directly from the measured load and displacement values ($C=\delta/P$). The compliance should be determined by using all the visually observed delamination onset values and all the propagation values and then it should be expressed as the function of them. After having done this, the ASTM [A94] prescribes to generate a least squares plot of log (δ_i/P_i) versus log (a_i) and then drawing a straight line through the data which results in the best least-squares fit. The value of the slope of this line is given by

$$n = \frac{\Delta_y}{\Delta_x} \tag{4.7}$$

which is the value of the parameter n to be inserted in the equation 4.6.

At fracture, $P = P_C$ and $G = G_{IC}$. This particular value of G is the mode I interlaminar fracture toughness of the laminate.

4.4.2 Test setup

In this paragraph the DCB test carried out in the laboratory is described, in particular with respect to the characteristics of the specimens and the setup of the test.

Three specimens have been tested with this type of test. Remembering the nomenclature used for the specimens, as described in the paragraph 4.3, the names of the three specimens subjected to the DCB test are P5_1, P5_2 and P5_3.

The main dimensions of each specimen are shown in table 4.1.

The length, for each of them, is 180 mm.

SPECIMEN	WIDTH (average value between five measures)	THICKNESS (average value between five measures on a side of the specimen and five measures on the other side)
P5_1	20.08	3.17
P5_2	20.09	3.24
P5_3	20.17	3.23

Table 4.1 – Dimension of the specimens for the DCB test [mm]

The DCB test is an opening mode test. Therefore, in order to pull the two arms of the specimen, a system to transfer the load is needed. As it is possible to see in the figure 4.8, a couple of hinges were attached to each specimen, one in the upper and one in the lower arm. In order to attach the hinges to the specimens, bi-component glue was used.

In figure 4.8 it is possible to see two of the specimens used for the DCB test, with the hinges and also with the white paint and the graph paper already described in the paragraph 4.3.

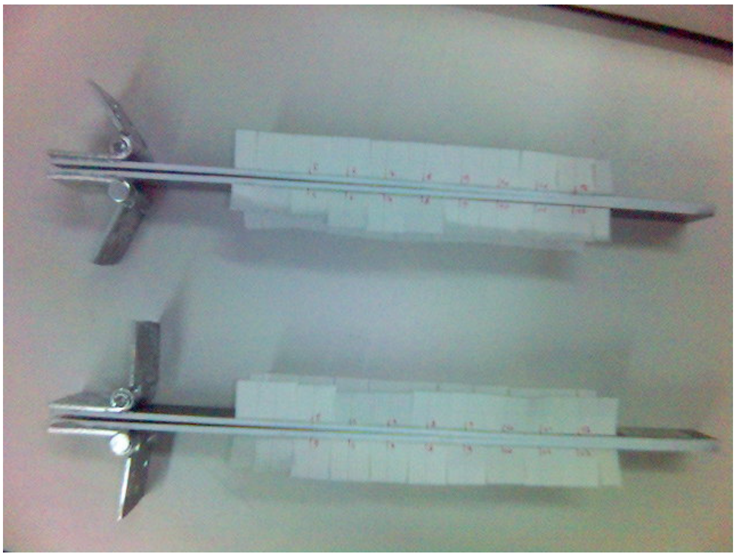

Figure 4.8 – Specimens for the DCB test

The initial length of the crack a_0 was the same for all the three specimens, with the value of 50 mm measured from the center of the hinges to the initial position of the tip of the crack, as it is possible to see in figure 4.9.

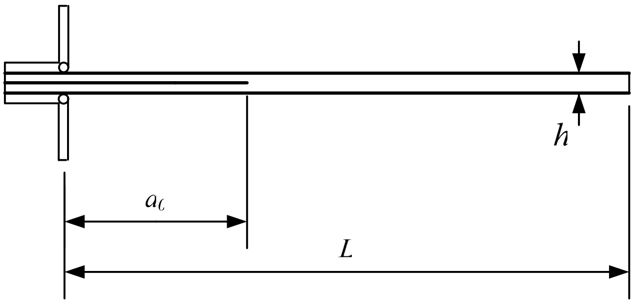

Figure 4.9 – Length of the initial crack measured from the hinges

Each test has been carried on under displacement control, with a constant speed of application of the displacement of 2.5 mm for each minute.

For each specimen the test has been stopped when the propagation of the crack reached about 50 mm, for a total length of the crack of about 100 mm.

This is a value of propagation double of the one that the ASTM D5528-94a prescribes. The ASTM says that it is sufficient a propagation of the crack of 25 mm in order to do the calculation of the G_{IC}.

Each specimen was pre-cracked. This means that, before doing the test, the crack has been let propagate for two or three millimetres. This fact has been done because the interest in all these tests was to study the behaviour of the material not in the onset of the delamination, but during the propagation of the crack.

4.4.3 Results

Once the test has been done on the three specimens, the following results have been obtained.

The first output directly obtained from the test machine is the force-opening curve. The three curves for each specimen are very close to each other and then only the most representative has been reported here.

Figure 4.10 shows the force-opening curve for the DCB test. It is possible to see the first elastic stage, the onset of the delamination, for a load of about 62 N, and the stage of the stable propagation of the crack.

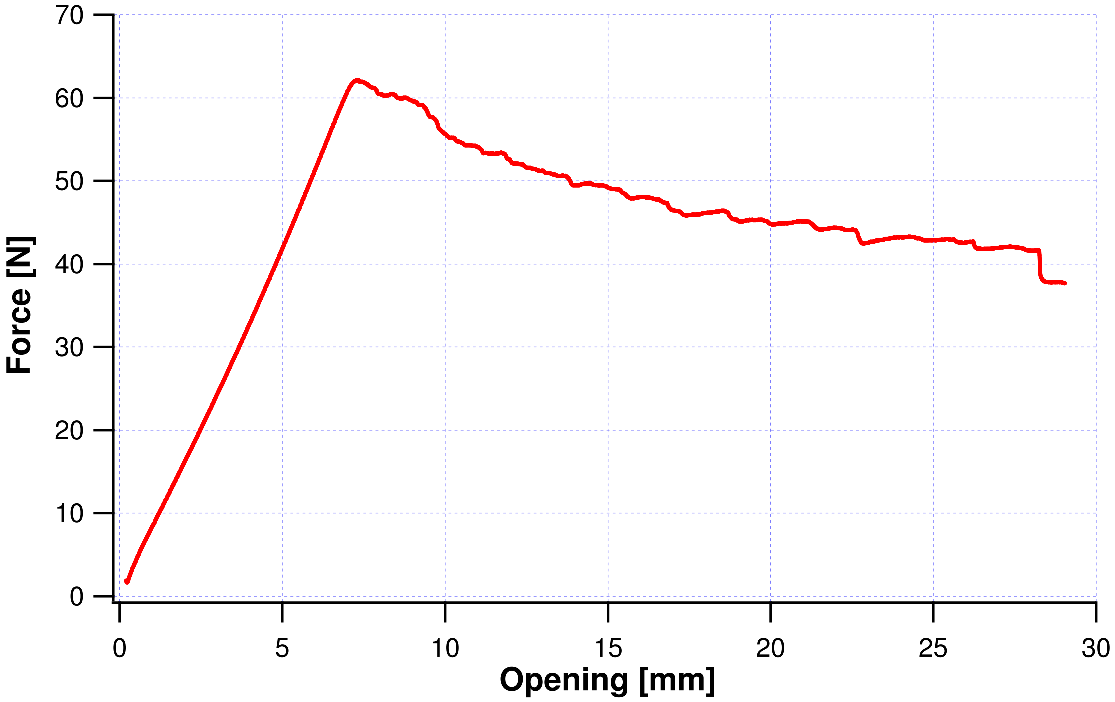

Figure 4.10 – Force vs. opening curve for the DCB test

Figure 4.11 shows the opening-crack length curve for the DCB test.

It has been obtained by correlating the lengths of the crack observed during the test, related to the time of the camcorder, and the displacement measured from the test machine, related to the time of the machine itself.

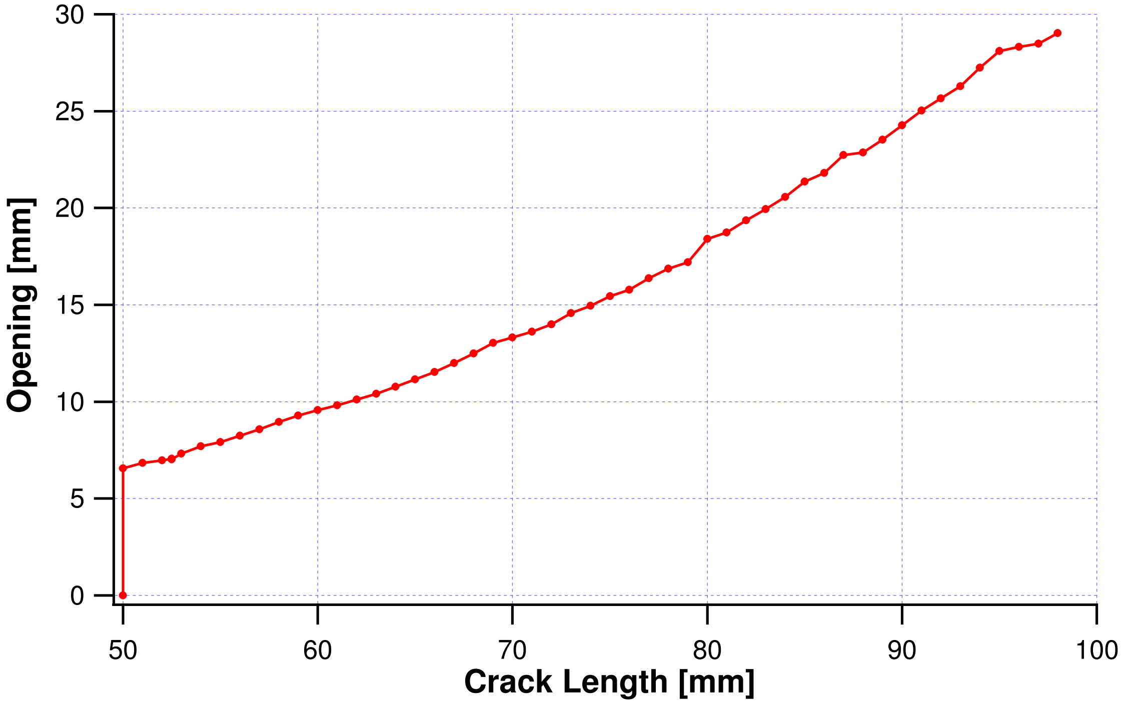

Figure 4.11 – Opening vs. crack length curve for the DCB test

From the previous output data it was possible to calculate the mode I interlaminar fracture toughness as described in the ASTM D5528-94a, at the point 12.1.2 "Compliance Calibration (CC) Method".

The length of the crack has been observed for each millimetre of propagation and, for the evaluation of the toughness, lengths between 50 mm and 75 mm were considered, corresponding to a length of propagation of 25 mm, as the standard says.

For each of the previous point the compliance has been calculated as following:

$$C = \frac{\delta}{P} \tag{4.8}$$

After having done this, a least squares plot of log (δ_i/P_i) versus log (a_i) has been generated and then a straight line through the data have been drawn, which results in the best least-squares fit, as it possible to see in figure 4.12.

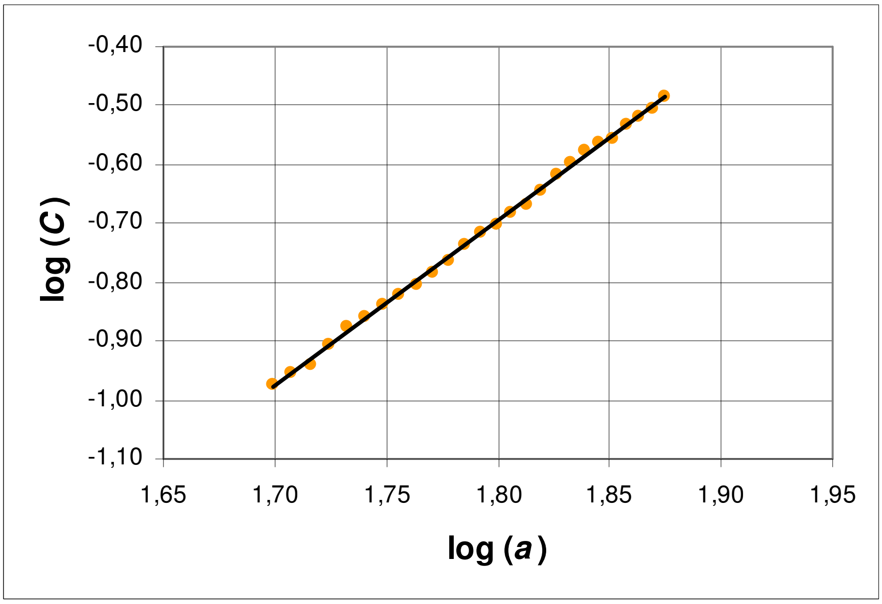

Figure 4.12 – Best least-squares fit for the compliance vs. crack length graph

After having evaluated the slope n of this line and after having calculated the value of G_{IC} for each of the points with the following relationship

$$G_{IC} = \frac{nP\delta}{2wa} \tag{4.9}$$

an average value of G_{IC} has been calculated and the final value found for the interlaminar toughness for the mode I is $G_{IC} = 643$ N/m.

4.5 Mode II test (4ENF)

4.5.1 Generality of the test

The 4ENF (Four-point End-Notched Flexure) test is a type of tests used to evaluate the mode II interlaminar fracture toughness in a composite laminate.

There is another type of test with the same aim, the ENF test, that is more common, but it suffers from unstable crack growth, that means that it is simple to evaluate the fracture toughness in the laminate in the beginning of the propagation, but it is usually not possible to study the behaviour of the specimen during the propagation of the crack.

The 4ENF specimen, with a different configuration, makes possible to obtain toughness values of the specimen also after the onset of the delamination.

The difference in the configuration between the 4ENF and the ENF test can be seen in the figure 4.13.

Basically the ENF test, in figure 4.13 (a), is a simple flexural test on three points, whereas the 4ENF, in figure 4.13 (b), is a flexural test on four points.

The 4ENF test have been not yet coded, but it have already used in the literature and it has been not difficult to find information about the most common features of the specimens and the modalities for the data reduction [ACB02].

The figure 4.13 (b) shows the pertinent geometry symbols for the 4ENF test geometry and specimen. The diameter of the loading and support cylinders is 10 mm, as for the three-point flexure test [ACB02].

The span between the lower supports, shown as *L*, should be 100 mm, whereas the span between the upper cylinders, shown as *l*, should be 60 mm.

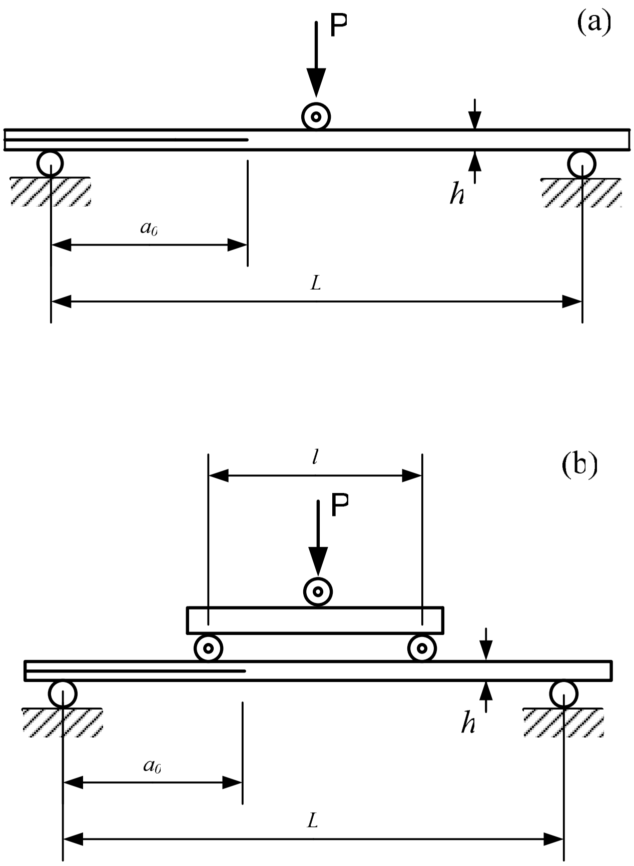

Figure 4.13 – Configuration of the ENF test (a) and of the 4ENF test (b)

The two cylinders of the loading system should be put on a beam that is able to rotate around a horizontal axis perpendicular to the longitudinal axis of the beam specimen.

This is necessary to be sure that the load is equally distributed between the two loading cylinders, because the 4ENF specimen is not symmetric.

The upper loading cylinder should be centered between the two upper loading cylinders and also between the two lower support cylinders.

The specimen, globally, should be long about 140 mm. In this way there is about an excess of 20 mm of specimen out of each lower support cylinder.

The length of the insert used to form the precrack should be 50 mm and the specimen should be put in the loading system in such way that the tip of the crack is inside the left upper loading cylinder for a length of 15 mm. It means that, in this case, the length of the initial crack (a_0) is 35 mm.

The evaluation of the fracture toughness (G_{IIC}) in the 4ENF test is based on the experimental compliance method.

The calculation of the compliance of the specimen directly from the measured load and displacement values ($C=\delta/P$) is executed from the linear stage of the load displacement curve obtained as record.

These compliance data have to be graphed versus the length of the crack and at this point it is necessary to generate a least squares plot of δ_i/P_i versus a_i and then drawing a straight line through the data which results in the best least-squares fit.

This line is described by an equation of the following type

$$C = C_0 + C_1 a \tag{4.10}$$

Combining the equations (4.10) and (4.1) it is possible to obtain the following expression

$$G = \frac{P^2 C_1}{2w} \tag{4.11}$$

where w is the width of the specimen.

Then, the value C_1 of the slope of the line resulting from the fitting is the value to be inserted in the (4.11) in order to obtain the value of the release of energy.

At fracture, $P = P_C$ and $G = G_{IIC}$. This last value of G is the mode II interlaminar fracture toughness of the laminate.

4.5.2 Test setup

In this section the setup of the 4ENF test and the characteristics of the specimens are described.

Three specimens were tested with this type of test. Remembering the nomenclature used for the specimens, as described in the paragraph 4.3, the names of the three specimens subjected to the 4ENF test are P5_4, P5_5 and P5_6.

The main dimensions of each specimen are shown in table 4.2.

SPECIMEN	WIDTH (average value between five measures)	THICKNESS (average value between five measures on a side of the specimen and five measures on the other side)
P5_4	19.92	3.23
P5_5	19.94	3.24
P5_6	19.84	3.20

Table 4.2 – Dimension of the specimens for the 4ENF test [mm]

The 4ENF test, as it has been already said, is a flexural test on four points, and required then a particular loading system. The one used in the tests, shown in the figure 4.14, is constituted by two lower support cylinders, above which the specimen is based on, by two upper loading cylinders, which transfer the load to the specimen, by another upper cylinder, that applies the load to all the system and by a plate that transfer the load from the upper cylinder to the two upper loading cylinders. All the cylinders are made of aluminum and they have a diameter of 10 mm.

With reference to the figure 4.13 (b), the dimensions of the fixture are the following. The span between the lower supports, shown as *L*, is 100 mm, whereas the span between the upper loading cylinders, shown as *l*, is 60 mm. The upper loading cylinder is centered between the two upper loading cylinders and also between the two lower support cylinders.

The length of the insert used to form the precrack is 50 mm and the specimen has been put in the loading system in such way that the tip of the crack is inside the left upper loading cylinder for a length of 10 mm. The length of the initial crack (a_0) is then 30 mm.

The dimension of the aluminum plate, instead, are 80 x 20 x 20 mm and it has three little notches in the contact points between the plate and the three cylinders.

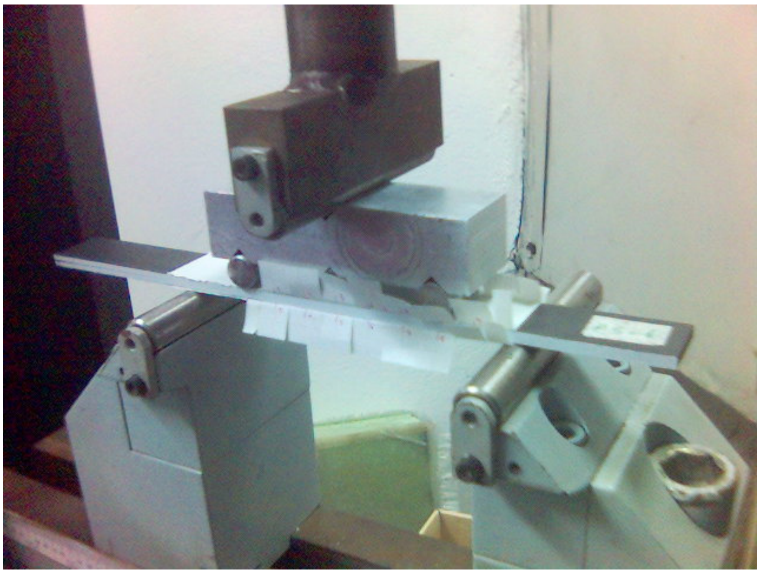

Figure 4.14 – Loading system for the 4ENF test

The stiffness of this system has been tested, in order to evaluate its capacity of transferring the load. The two upper loading cylinders, the plate and the upper cylinder have been put on a steel metal plate and this system has been loaded and its response has been evaluated. The force-displacement curve for the loading system is shown in figure 4.15.

Each test has been carried on under displacement control, with a constant speed of application of the displacement of 0.5 mm for each minute. In all the specimens the test has been stopped after a propagation of the crack of about 50 mm, having then let the crack propagate from a length of 30 mm to a length of about 80 mm, and after this each specimen has been unloaded and the unloading stage has been evaluated in order to check if it came back about to a zero load for a zero displacement.

All the results will be presented in the next paragraph.

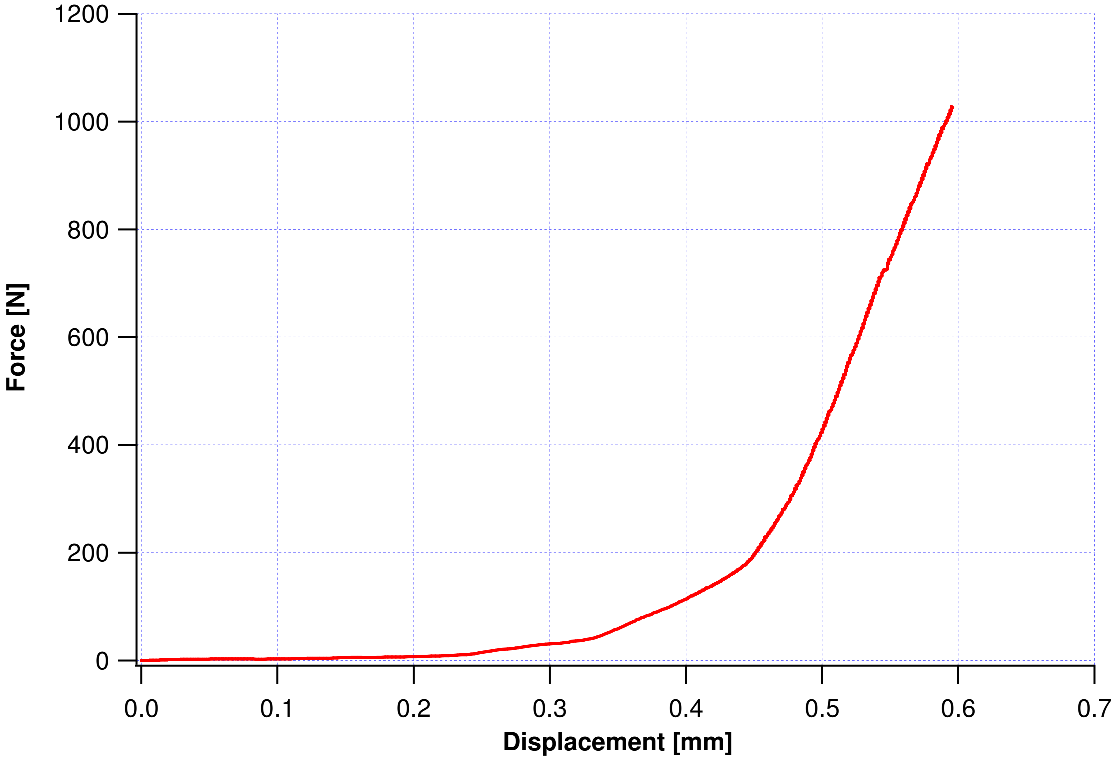

Figure 4.15 – Response of the loading system

4.5.3 Results

Once the 4ENF test has been done on the three specimens, the following results have been obtained.

The first output directly obtained from the test machine is the force-deflection curve. The three curves for each specimen were very close to each other and then only the most representative has been reported here.

In figure 4.16 the force-deflection curve for the 4ENF test is shown. After the elastic stage, the propagation happens with a different behaviour with respect to the DCB test. There is a horizontal irregular stage in which the crack grows and the force is practically constant. When the crack reaches the second loading upper cylinder it stops propagating and the force starts to increase again.

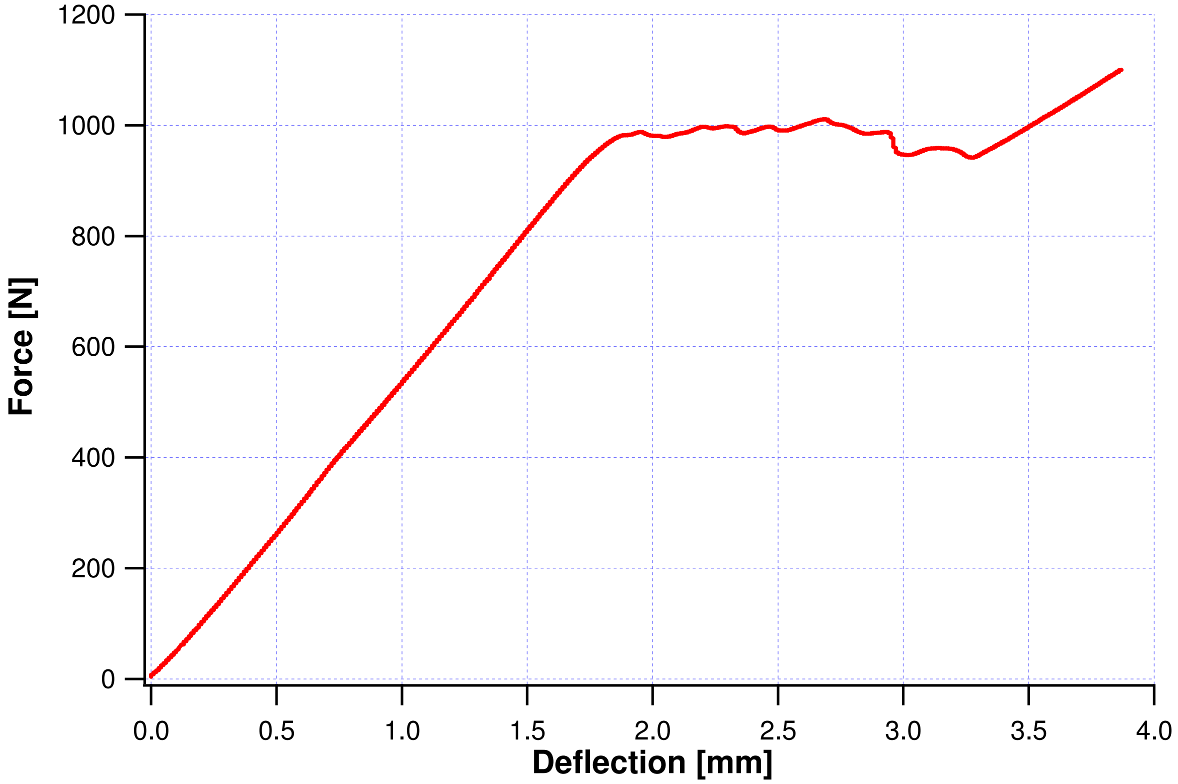

Figure 4.16 – Force vs. deflection curve for the 4ENF test

In figure 4.17 the propagation of the crack is shown. It is possible to see that the crack start to propagate about for the same displacement in which, in the force-deflection curve, the horizontal stage starts.

In this case the last point in which the crack was observed was for a propagation of 46 mm, that means a final length of crack of 76 mm, because of some difficult in follow the propagation in the last millimeters before the second loading cylinder.

This difficulty was due to the fact that the mode II propagation is a sliding mode, not clear to see as the mode I, in which the separation of the two surfaces is very clear.

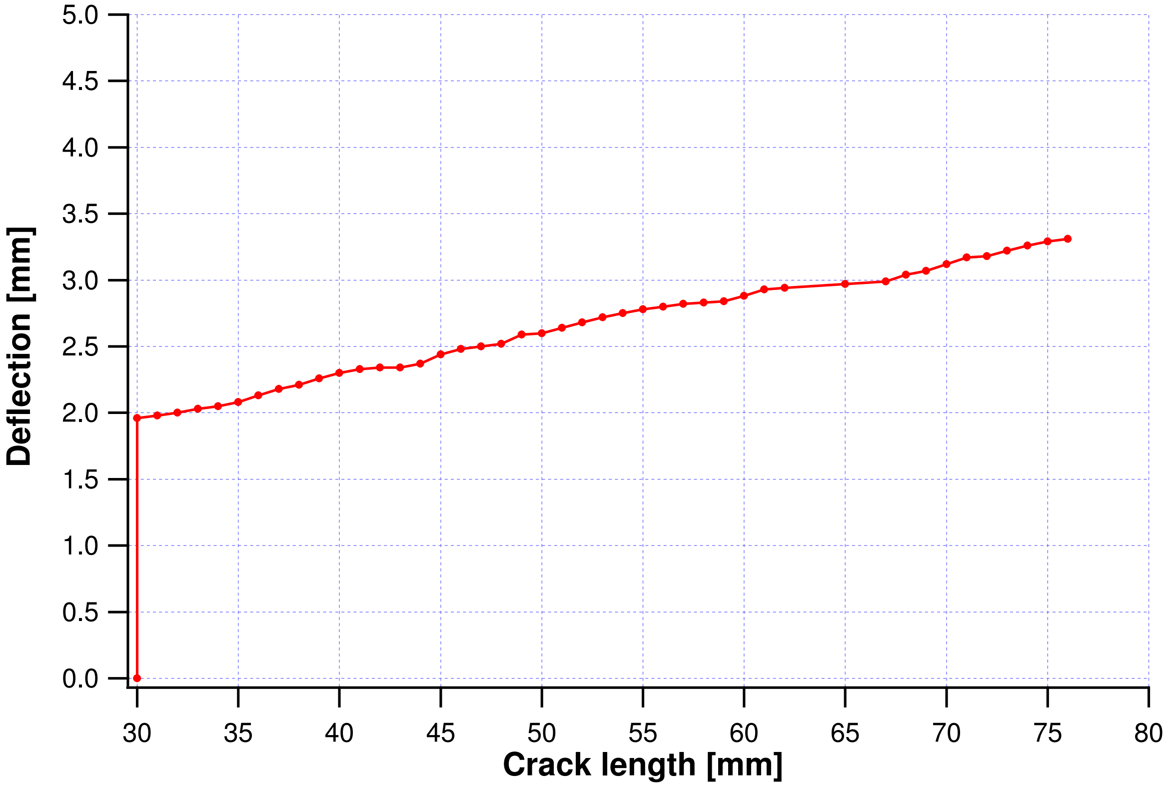

Figure 4.17 – Deflection vs. crack length curve for the 4ENF test

As for the DCB test, after have obtained the above outputs, the calculation of the mode II interlaminar fracture toughness become possible as described in the section 4.5.1.

The calculation have been done by implementing the described procedure in the Matlab code and the value obtained for the mode II toughness is G_{IIC} = 905 N/m.

4.6 Mixed mode I/II test (SLB)

4.6.1 Generality of the test

The Single-Leg Bending (SLB) is a mixed-mode I/II test which was proposed by Yoon and Hong [YH90] as a modified ENF specimen.

The main advantage of the SLB test, which is not yet coded, is that the total energy release rates can be obtained directly from test data by a compliance calibration procedure. Then, any mistake in the assignment of material properties, geometric properties, and the effects of finite width are avoided.

In figure 4.18 the configuration of this test is shown. It is a flexural test on three points with only the superior arm of the crack based on one of the lower support cylinder.

The upper loading cylinder is centred between the two lower ones and the initial length of the crack (a_0), with reference at the figure 4.18, has to be smaller than half of the span (L).

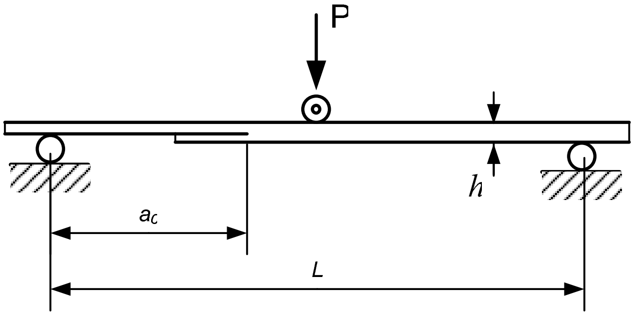

Figure 4.18 – Configuration of the SLB test

A typical span for this test is L = 100 mm, with an initial value of the crack a_0 = 35 mm.

As many authors have found, the mixed mode ratio of this test varies slightly in dependence of the actual length of the crack. Some of the values proposed are shown in table 4.3.

a [mm]	20	30	40	50	60	70	
	1.764	1.633	1.555	1.509	1.479	1.458	*
	1.665	1.555	1.500	1.467	1.445	1.429	**
	1.893	1.719	1.626	1.569	1.530	1.502	***

Table 4.3 – Values of the G_{IC}/G_{IIC} ratio for the SLB test evaluated from the following authors:

*** BRUNO and GRECO, 2001, ** BAO et al., 1992, *** CARLSSON 1986, OLSSON 1992,**

4.6.2 Test setup

In this section the setup of the SLB test and the characteristics of the specimens are described.

Four specimens were tested with this type of test. Remembering the nomenclature used for the specimens, as described in the paragraph 4.3, the names of the three specimens subjected to the SLB test are P6_4, P6_5, P6_7 and P6_8.

The main dimensions of each specimen are shown in table 4.4.

SPECIMEN	WIDTH (average value between five measures)	THICKNESS (average value between five measures on a side of the specimen and five measures on the other side)
P6_4	19.97	3.23
P6_5	19.96	3.24
P6_7	19.82	3.16
P6_8	19.98	3.12

Table 4.4 – Dimension of the specimens for the SLB test [mm]

With reference to the figure 4.18, the dimensions of the fixture are the following. The span between the lower supports, shown as L, is 100 mm and the upper loading cylinder is centred between the lower. The initial length of the crack (a_0) is 35 mm.

The test has been carried on under displacement control, with a speed of application of the displacement of 1 mm for each minute, and the test has been stopped for a propagation of the crack of about 40 mm, corresponding to a total length of the crack of about 60 mm.

4.6.3 Results

The outputs of this test, like the previous, are the force-deflection curve, shown in figure 4.19, and the deflection-crack length curve, shown in figure 4.20.

By comparing the two previous curves it is possible to see that there is an elastic stage, in which the crack does not propagate, followed by a first stage of propagation, which last until the crack reaches the central upper loading cylinder.

After this point the crack continue to propagate very slowly. It looks an average behaviour between the DCB and the 4ENF test.

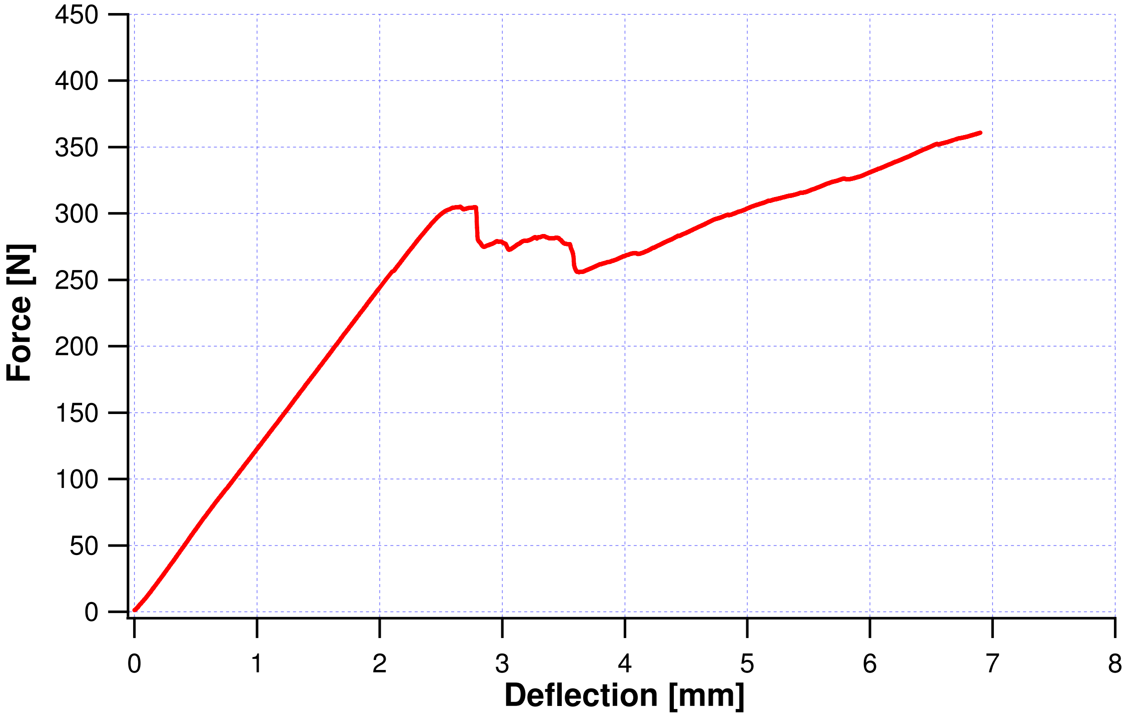

Figure 4.19 – Force vs. deflection curve for the SLB test

From the single-leg bending test any calculation of the value of the interlaminar fracture toughness for the mixed mode I/II has not been done.

Whereas the previous test have been done both in order to obtain the values of the interlaminar toughness for the relevant modes and to have a comparison with the finite element modelling with cohesive elements, the single-leg bending test has been instead carried on only to have a comparison in order to evaluate the potential of the cohesive zone model for the prediction of delamination propagation under mixed mode (I and II).

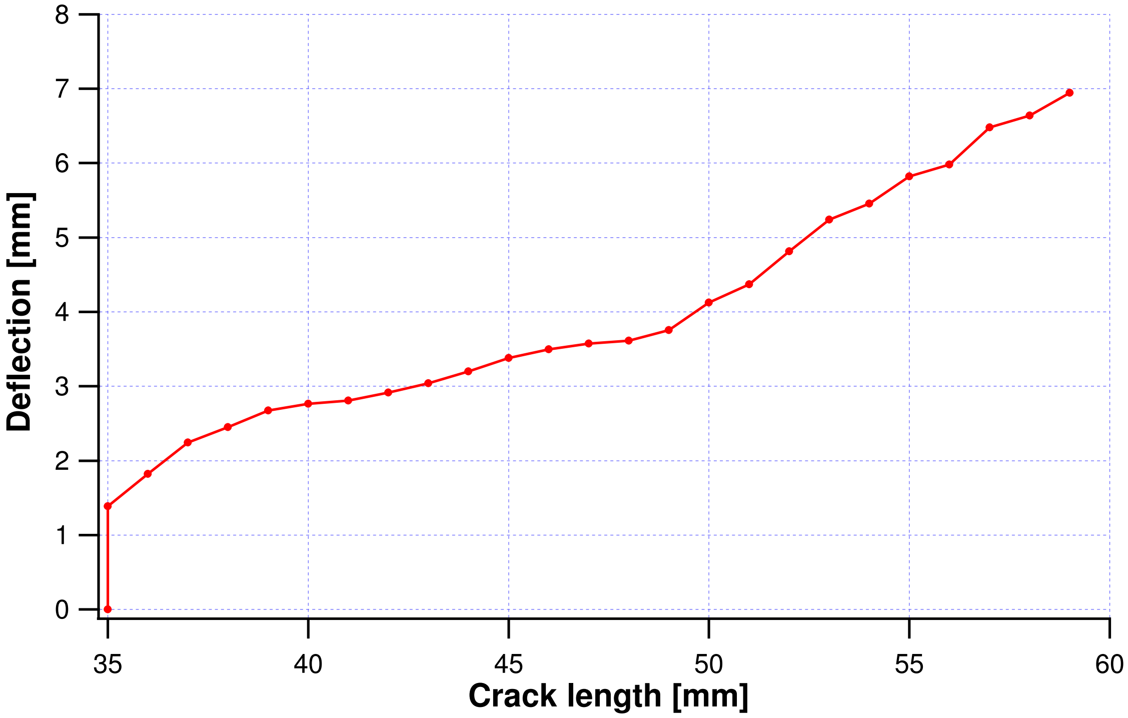

Figure 4.20 – Deflection vs. crack length curve for the SLB test

4.7 Comments

This chapter presented the tests of fracture mechanics carried out for the aim of this thesis. They are a mode I test, DCB, a mode II test, 4ENF, and a mixed mode test, SLB.

The specimens were manufactured from uniaxial pre-preg plies made of carbon fibres and a matrix of epoxy resin and the consolidation happened under hot press and vacuum bag.

All the manufacturing process of the specimens, from the layup of the specimen to the consolidation has shown characteristics of a good repeatability.

The system chosen to evaluate the length of the crack, with the white paint, the graph paper and the camcorder has shown a rather good precision in the evaluation of the length of the crack.

From each of the three tests two curves have been obtained:

- Force versus displacement curve.
- Displacement versus crack length curve.

Moreover, the tests for the mode I and mode II were used for the calculation of the interlaminar fracture toughness for the relevant mode of delamination.

The experimental tests showed accordance with the typical results of these tests. They can therefore be considered a good starting point for the comparison with the finite element modelling with cohesive elements discussed in the chapter 5.

Chapter 5

Finite element analysis and comparison with experimental tests

5.1 Introduction

This chapter presents a finite element modelling with cohesive elements of the tests of fracture mechanics already discussed in chapter 4 and a comparison between the results of the modelling and the ones obtained from the experimental tests.

The tests considered in this chapter for the modelling are the following:

- DCB test (mode I).
- 4ENF test (mode II).
- SLB test (mixed mode I/II).

The modelling has been done with the finite element code ABAQUS 6.5, using its explicit solver, described in the section 3.3.1.

For each model, the first step is a comparison between the force versus displacement curve obtained with the modelling and the same curve obtained by experimental. The comparison with experimental tests is presented also for the displacement versus crack length curve.

Finally, for the three models, the influence the interface cohesive stiffness has been evaluated and, for the mixed mode only, the differences between the linear and quadratic propagation criterion has been evaluated.

5.1.1 General characteristic of the models

This paragraph describes all the characteristics of the finite element models presented in this chapter.

In each model, the arms of the specimen and the cohesive layer are modelled each one with particular characteristics.

The arms of the specimen give the geometry of the model and they are modelled with solid two-dimensional elements with four nodes (CPE4R).

The behaviour of these elements is elastic orthotropic, without any failure criterion, and the elastic parameters for these elements are reported in table 5.1.

E_1 [MPa]	E_2 [MPa]	E_3 [MPa]	ν_{12}	ν_{13}	ν_{23}	G_{12} [MPa]	G_{13} [MPa]	G_{23} [MPa]
130000	6500	6500	0.26	0.26	0.50	2700	2700	2700

Table 5.1 – Mechanical characteristics given to the CPE4R solid elements

In the previous table, the quantities E_1, E_2, E_3, are the elastic modules in the direction of the fibres, in the direction of the width of the model and in the direction of the thickness, respectively; ν_{12}, ν_{13} and ν_{23} are instead the values of the Poisson's ratio. Finally, G_{12}, G_{13} and G_{23} are the shear modules. Some of the previous quantities are determined by experimental test. In particular E_1, E_2, ν_{12} and G_{12}, are evaluated by experimental. All the other elastic parameters are assumed from literature. The density given to these elements is $\rho = 1500$ kg/m^3.

For the modelling of the cohesive layer, four-node two-dimensional cohesive elements (COH2D4) with four nodes are used. These elements have the constitutive law that has already been described in section 3.3.2, and, with reference to that paragraph, the parameters given for describing the cohesive law are shown in table 5.2.

E [MPa]	G [MPa]	σ_{0I} [MPa]	σ_{0II} [MPa]	G_{IC} [N/m]	G_{IIC} [N/m]
2400	857	20	40	643	905

Table 5.2 – Mechanical characteristics given to the COH2D4 cohesive elements

In the previous table, E is the elastic modulus of the resin, G is the shear modulus of the resin, σ_{0I} and σ_{0II} are the elastic limit for the mode I and for the mode II respectively, and G_{IC} and G_{IIC} are the values of the critical release of energy for the mode I and for the mode II respectively. The density given to these elements is $\rho = 15000$ kg/m^3. This value is larger than the real value for the resin, and it was given in order to increase the limit of stability of the explicit method, which, as said in section 3.3.1, depends also on the density of the material.

A traction-separation behaviour, as defined in section 3.3.2, is assigned to the cohesive elements. As damage initiation criterion the quadratic nominal stress criterion is assumed, related to the values of σ_{0I} and σ_{0II}, whereas, for the evolution of the damage, the energetic criterion defined as ‘Power law form’ is used, which requires the values of G_{IC} and G_{IIC}.

In some models, as it will be explained in the relevant section, contact elements are required, in order to avoid compenetration between parts of the model itself.

All the analyses are performed as geometrically nonlinear analyses and under displacement control. The displacement is applied as boundary condition and a law of appliance of the displacement has to be defined. The variation of amplitude with time, in ABAQUS, can be specified in several ways.

In an explicit analysis the choice of this law has to be done with particular care. The amplitude curve has to be as regular and smooth as possible, in order to avoid dynamical effects and inaccuracy in the solutions. One of the curves that ABAQUS give to define the variation of amplitude is the smooth step amplitude definition with two data points, shown in figure 5.1. The only two data that have to be defined are the maximum amplitude and the time at what the amplitude has to be reached.

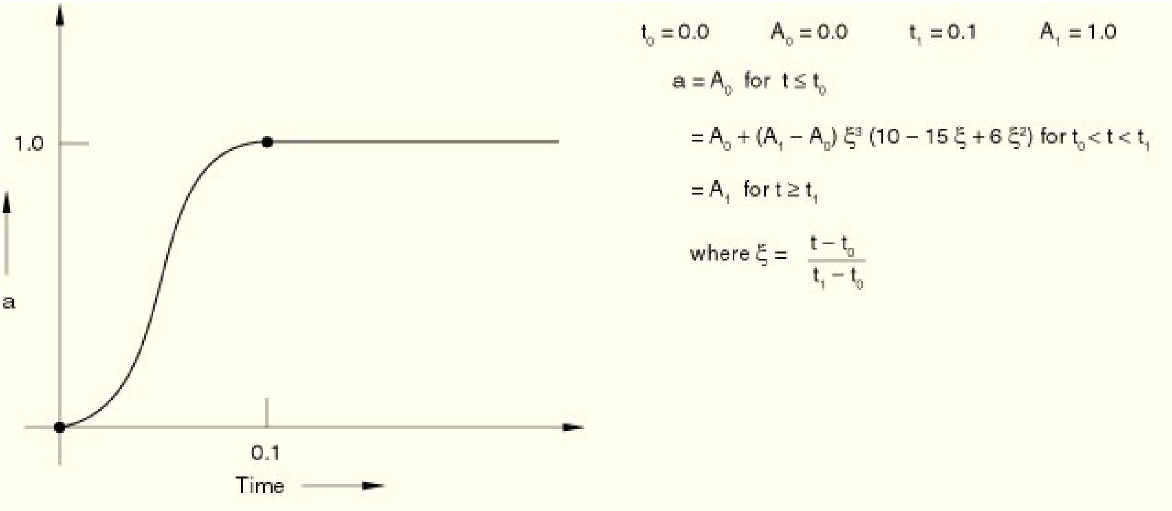

Figure 5.1 – Smooth step amplitude definition with two data points

5.1.2 Evaluation of the length of the crack

The length of the crack for each finite element model is evaluated through the analysis of the damage of the cohesive elements. The damage is described, as told in the section 3.3.2, by the parameter D. In each integration point of the element, a value equal to zero is assumed if the element is not damaged at all, in that integration point, and a value equal to one is assumed if the element is completely damaged and it gives no more contribution to react to the propagation of delamination.

There are some ways to evaluate the length of the crack based on the value of the damage parameter.

One way is to consider the tip of the crack in the position of the integration point of the element in which first, starting from the initial position of the tip of the crack, the value of the damage is smaller than $D = 1$. The total length of the crack is given, in this case, by the sum of the initial crack and the distance between the current tip of the crack and the initial tip. This means to considerate the crack propagated only when the element is completely damaged.

The second way is to consider the tip of the crack in the position of the integration point of the element in which first, starting from the initial position of the tip of the crack, the value of the damage is equal to $D = 0$. The total length of the crack is given, also in this case, by the sum of the initial crack and the distance between the current tip of the crack and the initial tip. This means to considerate the crack propagated when the element starts to be damaged. For each value of the load, or of the displacement, the difference between the value of the length of the crack for $D = 0$ and the value for $D = 1$ is the length of the cohesive zone. The length of the cracks shown in the section 5.2 for the FE modelling are all evaluated, for $D = 1$ and $D = 0$, assuming the previous considerations.

5.2 Comparison with experimental and parametric analysis

5.2.1 Mode I test (DCB)

The geometry of this mode I test has been already described in the chapter 4. Now the finite element modelling of this test is presented.

The figure 5.2 shows the configuration adopted for the modelling and the dimensions of the specimen. The total length (*L*) of the specimen is 140 mm, and the initial length of the crack (a_0) is 50 mm. The total thickness (*h*) is 3.24 mm.

The mesh adopted is made of two types of elements. For the arms solid two-dimensional elements (CPE4R) are used. Between the two arms, as shown in figure 5.2, there is a cohesive layer, with a thickness $t = 0.02$ mm. The elements used in the mesh of this layer are two-dimensional bilinear cohesive elements (COH2D4).

The cohesive elements are not present for all the length of the specimen, but only from the end of the length (a_0), where the tip of the initial crack is, until the end of the specimen.

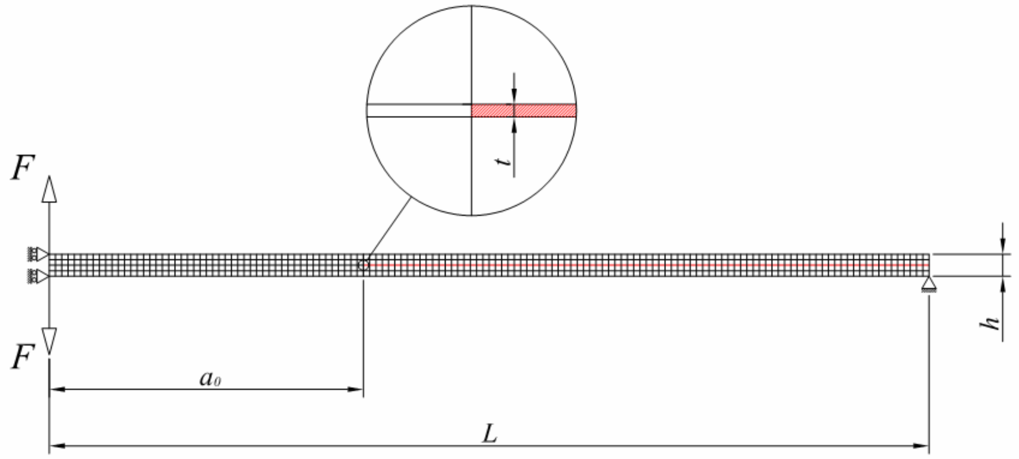

Figure 5.2 – Configuration, dimensions and mesh for the DCB model

The dimension of the mesh, both for the solid and the cohesive elements, is constant for all the model and equal to 0.25 mm. This dimension, evaluated after some analyses, has been chosen in order to have not less than three or four elements in the cohesive zone. In the direction of the thickness of the specimen, two solid elements were put in each arm and only one cohesive element in the interlaminar layer.

The simulation is under displacement control. The displacement is applied, as shown in figure 5.2, to the first node on the top of the upper arm and to the first node on the bottom of the lower arm. These last two nodes have also, as boundary condition, the displacement locked in the direction perpendicular to the applied displacement.

The last boundary condition is that the last node of the bottom of the lower arm has a displacement imposed equal to zero in the vertical direction.

All the other characteristics are the same described in the section 5.1.

In figure 5.3 it is possible to see the undeformed and the deformed shape of the specimen during the simulation.

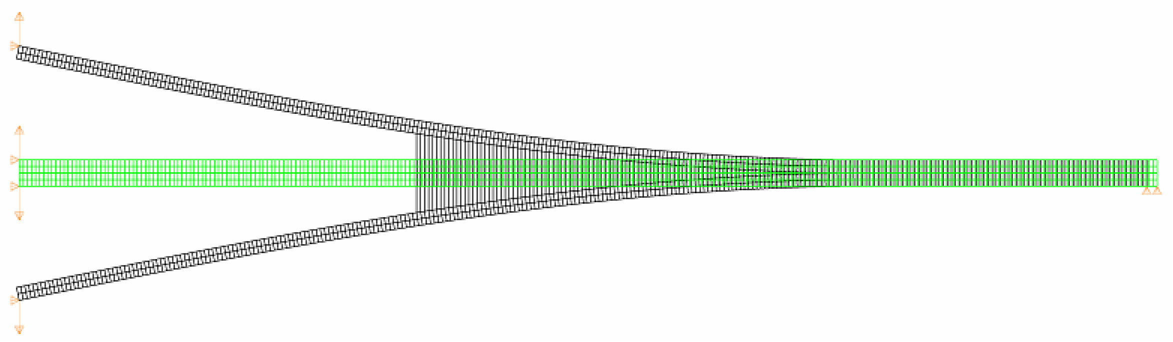

Figure 5.3 – Undeformed (green) and deformed (black) shape for the DCB test

The first result presented is the force-opening curve, which in figure 5.4 is compared with the same curve obtained in the experimental tests. There is a good correspondence between the elastic branches of the two curves and also the prediction of the onset of the propagation looks adequate.

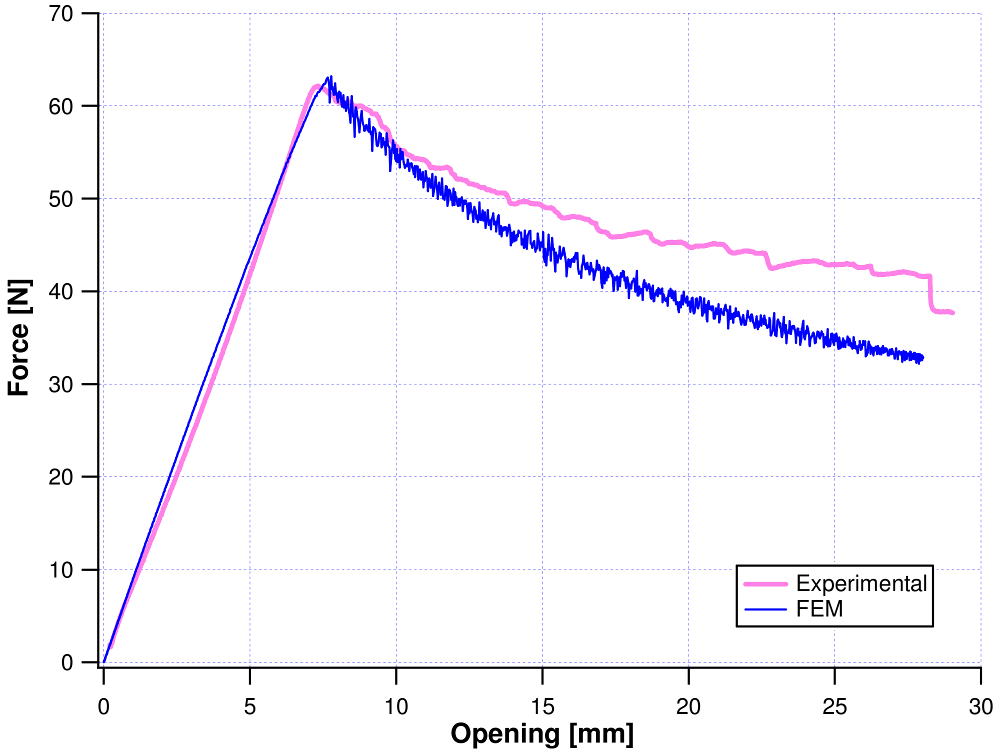

Figure 5.4 – Force vs. opening curve for the DCB test: comparison between experimental and FEM

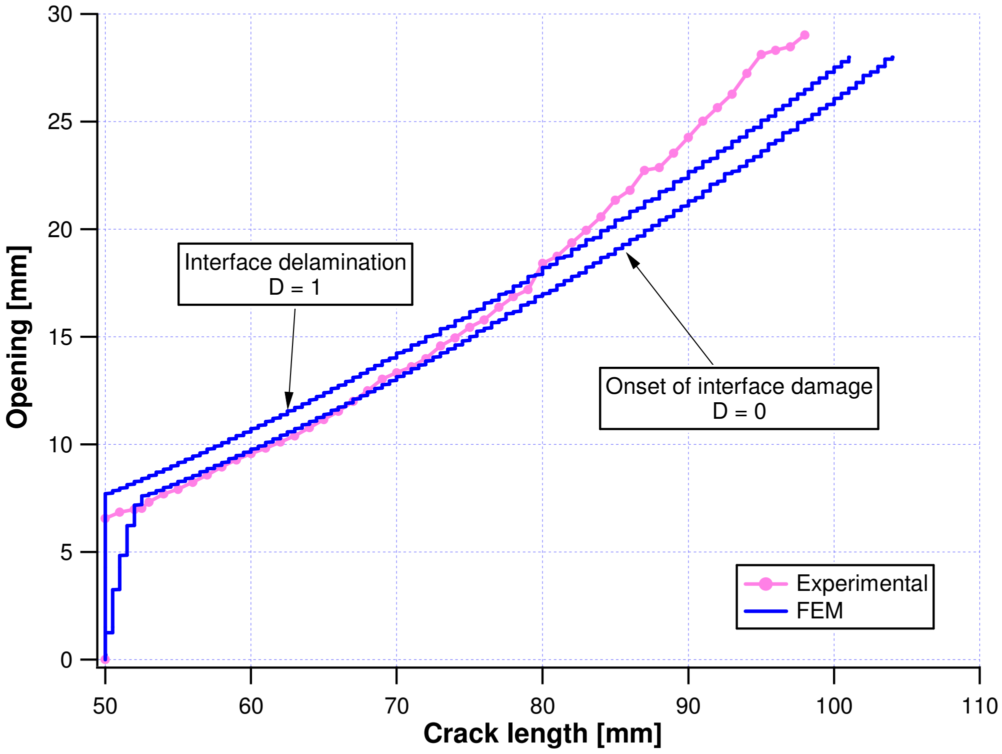

Figure 5.5 – Opening vs. crack curve for the DCB test: comparison between experimental and FEM

There is instead a difference in the propagation branch, with the stiffness of the FE model that decrease more quickly. There is no a sure explanation about this, but there is the possibility that it depends on the phenomenon of bridging, already observed and described in the experimental tests. The bridging operates in order to react to the propagation of the crack, and then it can be represented as an increment of the critical energy release (G_{IC}) for the material. Reminding that the bridging becomes more important as the length of the crack increases, it means that the value of G_{IC} is not constant during the delamination. In the FE modelling, instead, the value of the assigned G_{IC} remains constant for all the simulation. Therefore some analyses with different value of G_{IC} have been done.

The figure 5.6 shows the comparison between the same force-opening curves of the figure 5.4, in which the simulated curve is related to a value of G_{IC} equal to 643 N/m, both compared with a curve with a bigger value of G_{IC}, equal to 770 N/m. It is possible to see that the curve with the lower G_{IC} match the onset of the propagation of the experimental test, whereas the curve with the higher G_{IC} matches the propagation branch for bigger displacements. Probably with a variable value of G_{IC} during the simulation it could be possible to match the entire experimental curve.

The figure 5.5 shows the length of the crack for some values of the relative displacement. The experimental curve has been already discussed in chapter 4. The two other curves shown, instead, related to the finite element model, are the lengths of the crack evaluated, for $D = 0$ and for $D = 1$, as described in the section 5.1.2.

It is possible to consider good the prediction of the length of the crack if the experimental length of the crack is contained between the length for $D = 0$ and for $D = 1$. In this case, probably, the experimental curve should be closer to the one for $D = 1$, because during the test the crack has been assumed propagated when it was possible to see it with the camcorder, that means a complete damage.

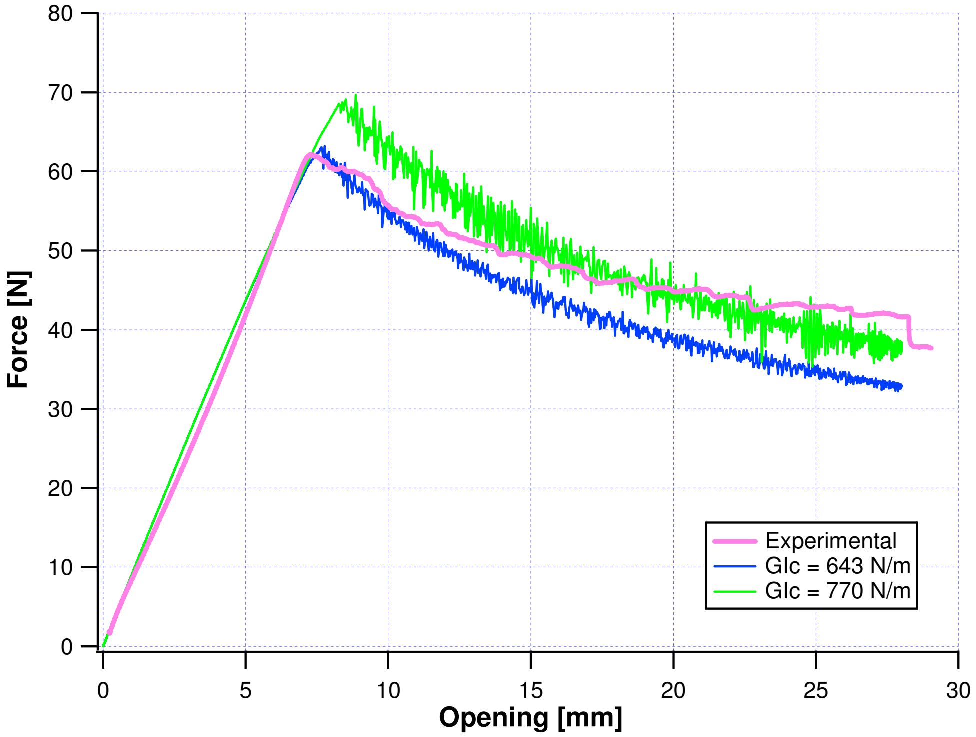

Figure 5.6 – Force vs. opening curve for the DCB test: different values of G_{IC}

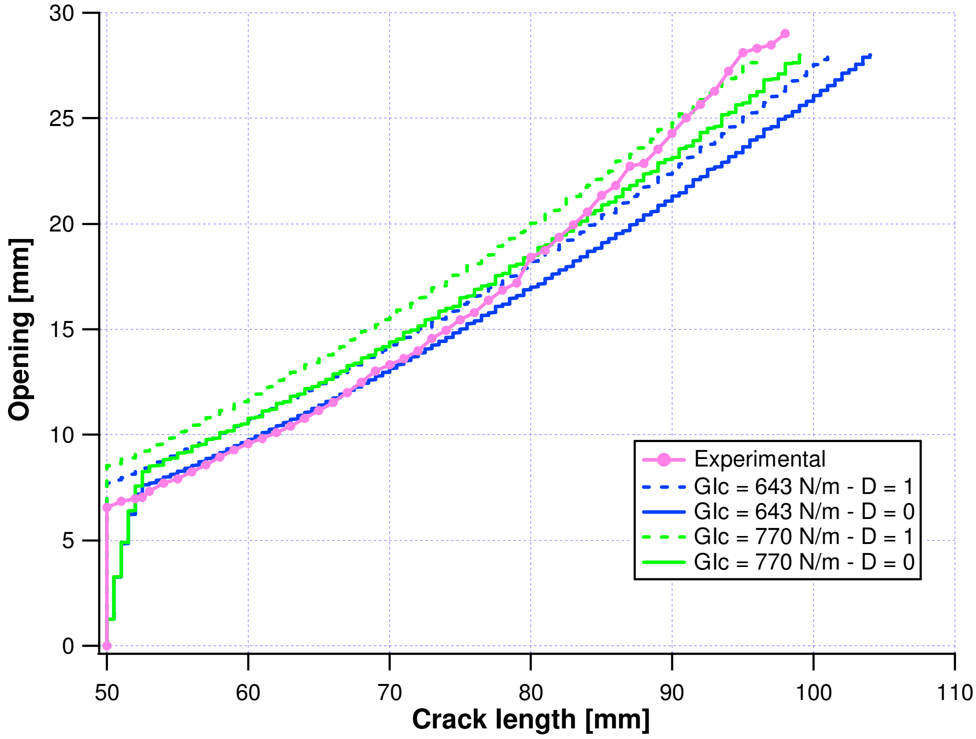

Figure 5.7 – Opening vs. crack length curve for the DCB test: different values of G_{IC}

It is possible to see, in figure 5.5, a good correspondence between experimental cracks and simulated cracks for the first 30 mm of propagation. For bigger displacements the simulated crack length becomes bigger than the experimental one.

This fact agrees with the behaviour of the curve force-opening shown in figure 5.4. Reminding that the opening in figure 5.4 is corresponding to the opening shown in figure 5.5, as the simulated force-opening curve moves away from the experimental one, the simulated opening-crack curve does the same.

Reminding that the ASTM D5528 – 94a prescribes that, for the calculation of G_{IC}, a propagation of 25 mm has to be considered, in order to avoid the influence of the bridging, it is interesting to observe that the finite element model, for such length of propagation of the crack, has a good correspondence with the experimental results.

The cohesive zone, as defined in the paragraph 5.1.2, for the cohesive model in figures 5.4 and 5.5, has a length of 3 mm. The dimension of the mesh is 0.25 mm, therefore there are twelve elements in the cohesive zone, that are a good number with respect to the minimum number of three or four elements necessary for a good behaviour of the cohesive zone model.

The figure 5.7, related to the figure 5.6, shows the behaviour of the length of the crack for the experimental test and for the finite element model with the original value of G_{IC}, compared with the model with G_{IC} = 770 N/m. As it was expected, the model with the bigger G_{IC} has, for the same opening, smaller values of the length of the crack.

After the comparison with the experimental tests, the influence of the interface stiffness on the cohesive model is evaluated.

The interface stiffness is the elastic modulus of the resin per unit thickness and is therefore given by dividing the elastic modulus of the resin by the thickness of the cohesive layer. Assuming that the value of the elastic longitudinal modulus of the resin is

$E = 2400$ MPa and the interface thickness is $t = 0.02$ mm, the interface stiffness K_N for the mode I is given by the following expression:

$$K_N = \frac{E}{t} = 120 \text{ GPa/mm} \qquad (5.1)$$

The interface stiffness K_N is the slope of the elastic branch of the cohesive law, as shown in figure 5.8(a).

The sensitivity of the cohesive model is then investigated by varying K_N. Three different values were used for the analysis. The first is the original value shown by equation 5.1. It is a value corresponding to a very steep slope of the constitutive law.

The two other values were therefore chosen considering the ratio between the area before the elastic limit and the area after the elastic limit.

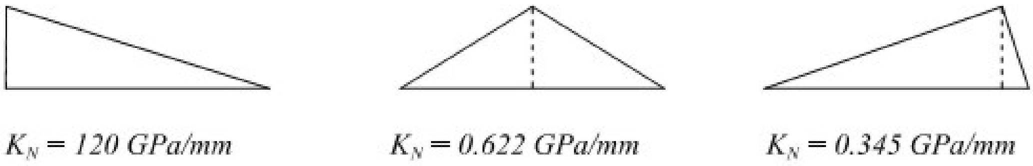

(a) **(b)** **(c)**

Figure 5.8 – Interface stiffness values for the mode I

The second value of K_N, as figure 5.8(b) shows, is related to a ratio between the two above areas of 1/1. It means that the constitutive law is an isosceles triangle. Reminding that the total area of the triangle is $G_{IC} = 643$ N/m and the elastic limit for the mode I is $\sigma_0 = 20$ MPa, it is simple to obtain the slope of the elastic branch as $K_N = 0.622$ GPa/mm.

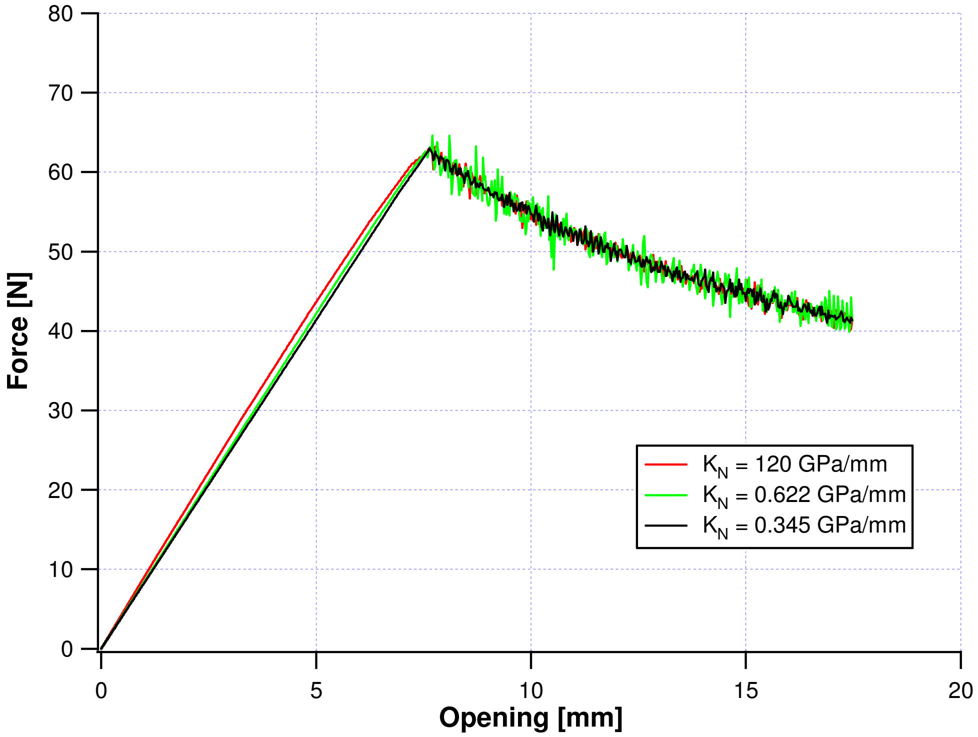

Figure 5.9 – Force vs. opening curve for the DCB test: influence of the interface stiffness

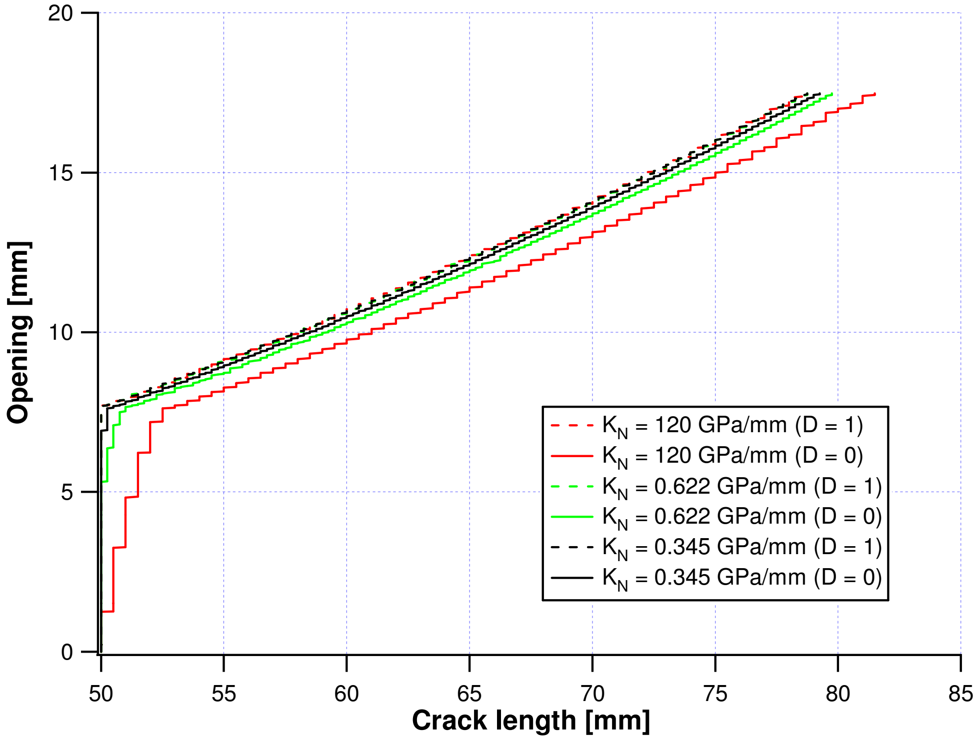

Figure 5.10 – Opening vs. crack length curve for the DCB test: influence of the interface stiffness

The third value of K_N, as figure 5.8(c) shows, is obtained considering a ratio between the area before the elastic limit and the area after the elastic limit equal to 9/1.

In this case the slope of the elastic stage is very low. With few calculations it is possible to evaluate the interface stiffness that is $K_N = 0.345$ GPa/mm.

The first comparison is between the force-opening curves of the models with the three values of the interface stiffness, shown in figure 5.9. It is possible to see that there is a small variation both in the initial slope of the curve and in the propagation.

The oscillations that became bigger by increasing the interface stiffness are due to the cohesive zone that became smaller, and then contain a smaller number of elements. It is possible to observe this in figure 5.10, where the opening–crack curves are shown for the three models. The length of the crack evaluated for $D = 1$ is not too different for all the models, whereas the length of the crack evaluated for $D = 0$ became closer to the correspondent curve for $D = 1$ by reducing the interface stiffness. Since the difference between the length of the crack evaluated for $D = 1$ and the length of the crack evaluated for $D = 0$ represent the length of the cohesive zone, it is clear that the cohesive zone became smaller by decreasing K_N.

The length of the cohesive zone for each model is shown in table 5.3.

Interface stiffness K_N [GPa/mm]	Length of the cohesive zone [mm]
120	3
0.622	1
0.345	0.5

Table 5.3 – Length of the cohesive zone for models with different interface stiffness K_N

5.2.2 Mode II test (4ENF)

This section presents the finite element modelling of the 4ENF test, mode II test, already described in the chapter 4.

With reference to the figure 5.11, which shows the configuration and the mesh adopted for the modelling, the span between the lower supports, shown as *L*, is 100 mm, whereas the span between the upper loading cylinders, shown as *l*, is 60 mm.

As for the experimental specimen, the tip of the crack is inside the left upper loading cylinder for a length of 10 mm. The length of the initial crack (a_0) is then 30 mm. The total thickness (*h*) is 3.24 mm.

The modelling of the 4ENF specimen is more complex than the DCB test.

For the arms, as in the DCB model, solid two-dimensional elements (CPE4R) were used. Between the two arms, as shown in figure 5.11, a cohesive layer, with a thickness of 0.02 mm, was put. The elements used in the mesh of this layer were two-dimensional bilinear cohesive elements (COH2D4). The cohesive elements are not present for all the length of the specimen, but only from the end of the length (a_0), where the tip of the initial crack is, until the end of the specimen.

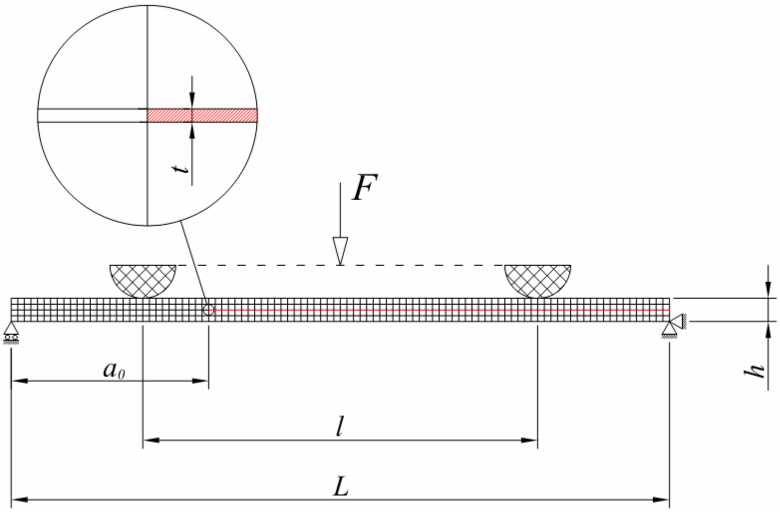

Figure 5.11 – Configuration of the 4ENF model

Between the two arms, in the region of the model in which there are not cohesive elements, contact elements are necessary to avoid any compenetration between the two edges of the crack.

In the model of the 4ENF test it is not possible to apply the displacement directly on the nodes because of the loading system made of two cylinders and because the specimen is not symmetric in the bending of the model. It means that the points of the specimen in which the two loading cylinders transfer the load during the test can change with the bending of the specimen.

The loading system is therefore formed by two cylinders of 10 mm of diameter modelled with the same solid two-dimensional elements (CPE4R) of the arms, but with the mechanical characteristics shown in table 5.4.

Elastic longitudinal modulus [GPa]	Poisson parameter	Density [Kg/m^3]
210	0.33	1500

Table 5.4 – Elastic constants of the loading cylinders

The boundary conditions applied to the model are that the node that represent the right support has an imposed displacement equal to zero in both the direction horizontal and vertical, whereas the node that represent the left support has an imposed displacement equal to zero only in the vertical direction.

All the other characteristics are the same described in the section 5.1.

In figure 5.12 it is possible to see the undeformed and the deformed shape of the specimen during the simulation.

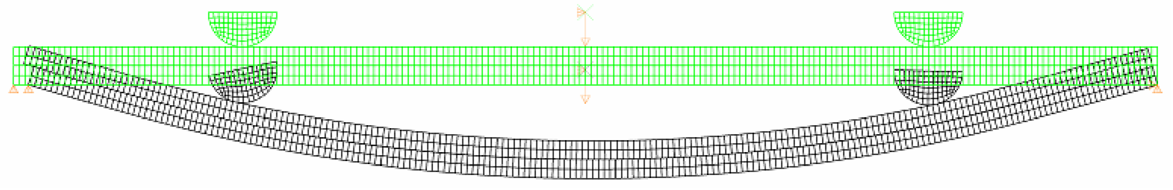

Figure 5.12 – Undeformed (green) and deformed (black) shape for the 4ENF test

The first result presented is the force-deflection curve, which in figure 5.13 is compared with the same curve obtained in the experimental tests. There is a very good correspondence between the elastic branches of the two curves and also in the prediction of the onset of the propagation and in the entire propagation branch the two curves are very close.

The figure 5.14 shows the length of the crack for some value of the deflection. The experimental curve has been already discussed in chapter 4. The two other curves, related to the finite element model, are the length of the crack evaluated, for $D=0$ and for $D=1$, as described in the section 5.1.2. The experimental curve is very close to the one for $D=1$, even if slightly outside the cohesive zone for most of the simulation, but its behaviour can be considered good. It has to be remembered that the visual evaluation of the crack in an experimental mode II test is more difficult than in a mode I test, because there is not an opening of the crack, but only a sliding, more difficult to measure. For this reason, an error bigger than in the DCB test can be considered also a good result. In reference [ACB02] it is recommended, in order to evaluate G_{IIC} from this test, to follow the delamination until its front reaches within 10 mm of the right loading cylinder. In this range, that means a total length of the crack of 70 mm, the behaviour of the cohesive model looks adequate.

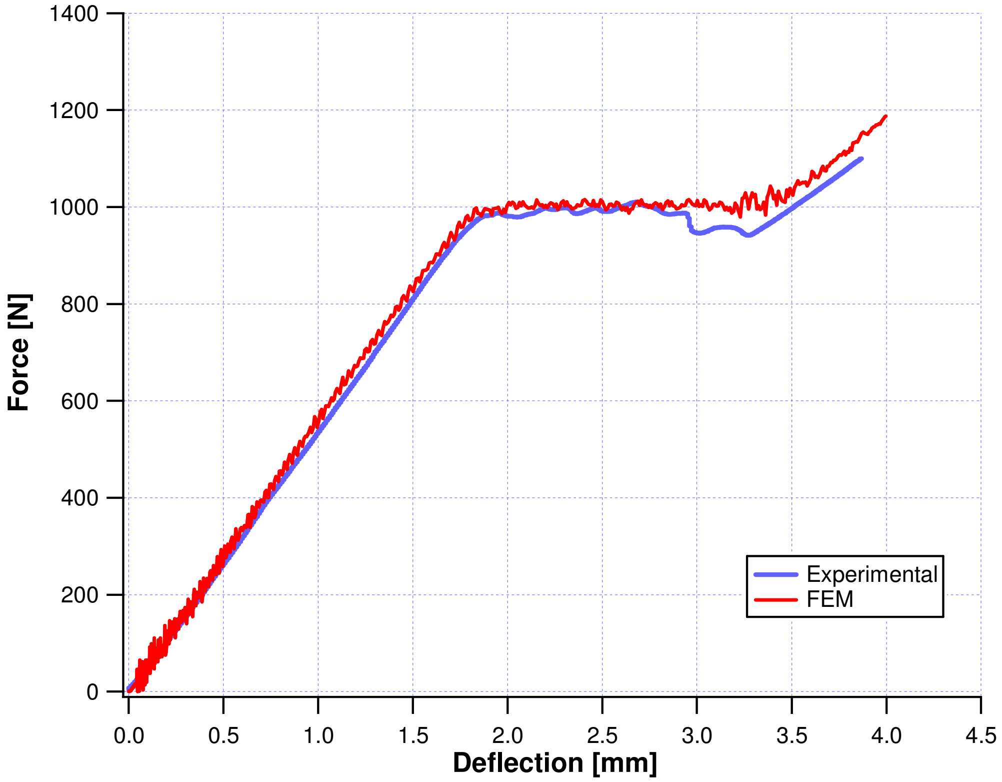

Figure 5.13 – Force vs. deflection curve for the 4ENF test: experimental and FEM

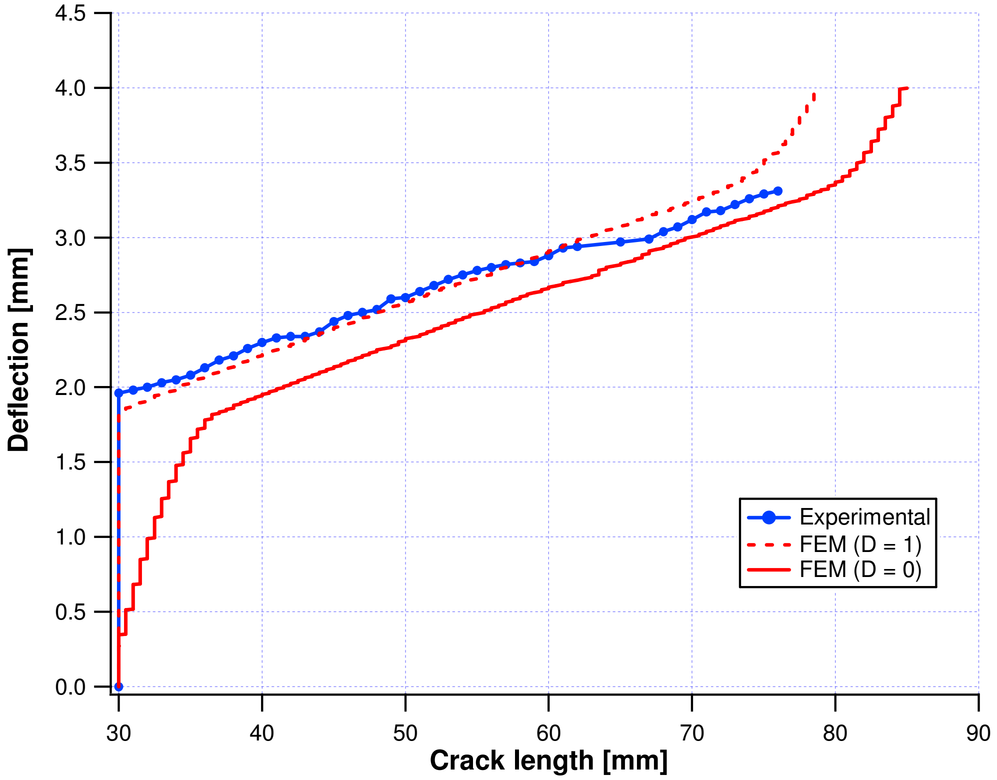

Figure 5.14 – Deflection vs. crack length curve for the 4ENF test: experimental and FEM

After the comparison with the experimental tests, the influence of the interface stiffness on the cohesive model is evaluated.

For the mode II, assuming that the value of the elastic shears modulus of the resin is $G = 857$ MPa and the interface thickness is $t = 0.02$ mm, the interface stiffness K_S is given by the following expression:

$$K_S = \frac{G}{t} = 42.9 \text{ GPa/mm} \tag{5.2}$$

The equation 5.2 shows the interface stiffness K_S related to the original value of the elastic modulus G assigned to the model. This situation is represented in figure 5.15(a).

The sensitivity of the cohesive model is then investigated also for the 4ENF test by varying K_S considering three different values. The first, as before, is the original value.

The two other values were chosen considering the ratio between the area before the elastic limit and the area after the elastic limit.

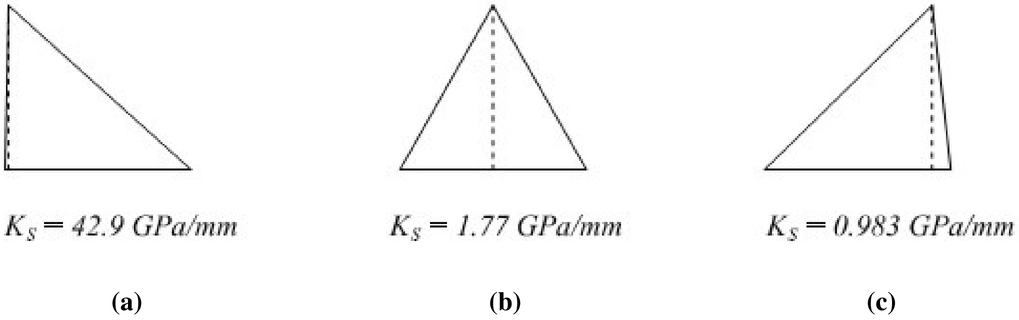

Figure 5.15 – Interface stiffness values for the mode II

The second value of K_S, as figure 5.15(b) shows, is related to a ratio between the two above areas of 1/1. It means that the constitutive law is an isosceles triangle.

Reminding that the total area of the triangle is $G_{IIC} = 905$ N/m and the elastic limit for the mode II is $\sigma_0 = 40$ MPa, it is simple to obtain the slope of the elastic branch as K_S = 1.77 GPa/mm.

The third value of K_S, as figure 5.15(c) shows, is obtained considering a ratio between the area before the elastic limit and the area after the elastic limit equal to 9/1. In this case the constitutive law is a triangle mirror to the one with the initial slope. With few calculations it is possible to evaluate the interface stiffness K_S = 0.983 GPa/mm.

The first comparison is between the force-deflection curves of the models with the three values of the interface stiffness, shown in figure 5.16. It is possible to see that there is a small variation both in the initial slope of the curve and in the propagation.

Also in this case the oscillations became bigger by increasing the interface stiffness. The reason is again the reduction in the dimension of the cohesive zone, which then contains a smaller number of elements. It is possible to observe this in figure 5.17, where the deflection–crack curves are shown for the three models. The length of the crack evaluated for $D = 1$ is not too different for all the models, whereas the length of the crack evaluated for $D = 0$ became closer to the correspondent curve for $D = 1$ by reducing the interface stiffness. Since the difference between the length of the crack evaluated for $D = 1$ and the length of the crack evaluated for $D = 0$ represent the length of the cohesive zone, it is clear that the cohesive zone became smaller by decreasing K_S. The length of the cohesive zone for each model is shown in table 5.5.

Interface stiffness K_S [GPa/mm]	Length of the cohesive zone [mm]
42.9	7
1.77	3
0.983	1

Table 5.5 – Length of the cohesive zone for models with different interface stiffness K_S

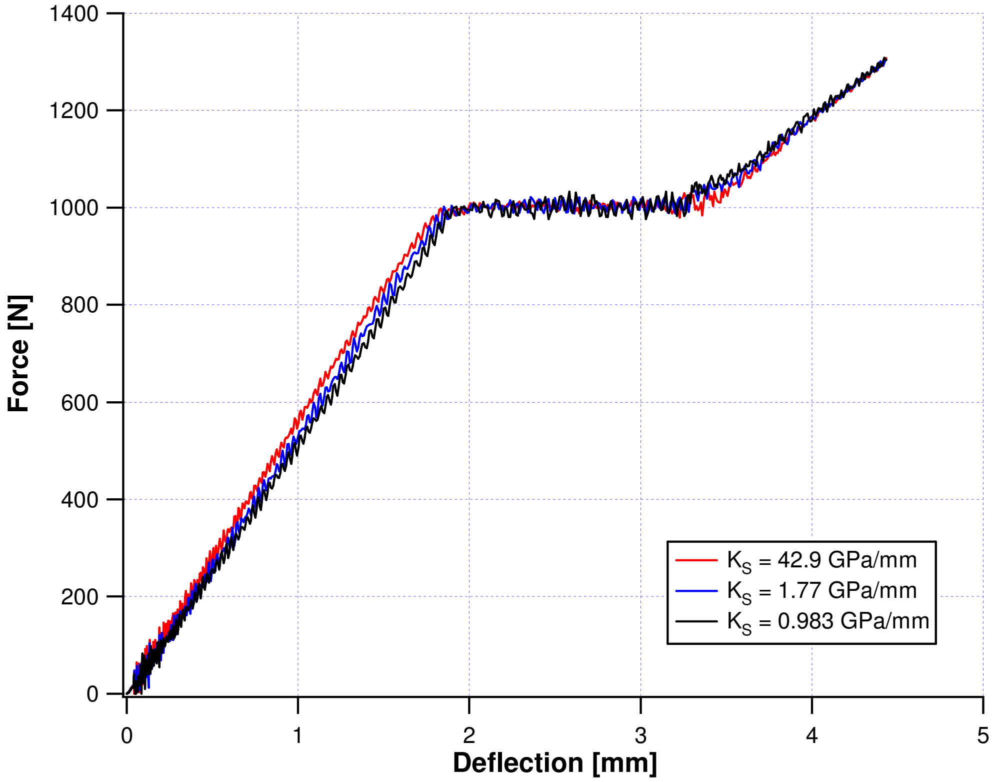

Figure 5.16 – Force vs. deflection curve for the 4ENF test: influence of the interface stiffness

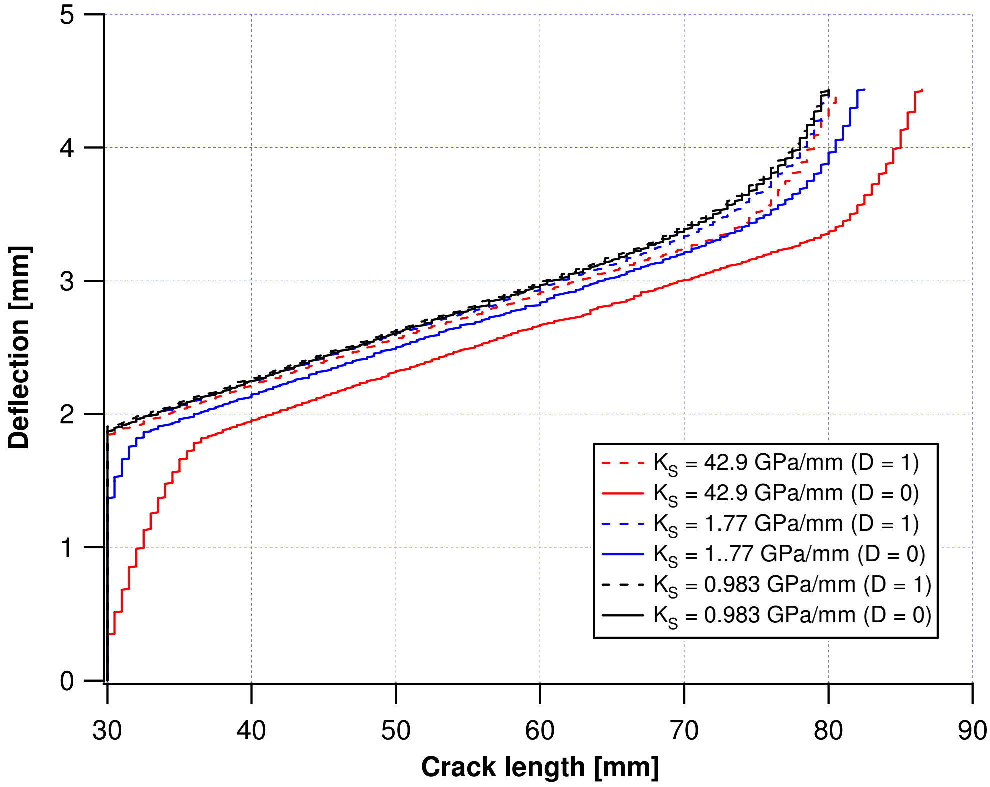

Figure 5.17 – Deflection vs. crack length curve for the 4ENF test: influence of the interface stiffness

5.2.3 Mixed mode I/II test (SLB)

This section presents the finite element modelling of the SLB test, mixed mode I/II test, already described in the chapter 4.

With reference to the figure 5.18, which shows the configuration and the mesh adopted for the modelling, the span between the lower supports, shown as L, is 100 mm. The upper loading cylinder is centred between the two lower ones and the initial length of the crack (a_0), measured from the left support is 35 mm. The total thickness (h) is 3.24 mm.

Regarding to the mesh of the SLB model, for the arms, as in the other models, solid two-dimensional elements (CPE4R) were used. Between the two arms, as shown in figure 5.18, a cohesive layer, with a thickness of 0.02 mm, was put. The elements used in the mesh of this layer are two-dimensional bilinear cohesive elements (COH2D4). The cohesive elements are not present for all the length of the specimen, but only from the end of the length a_0, where the tip of the initial crack is, until the end of the specimen.

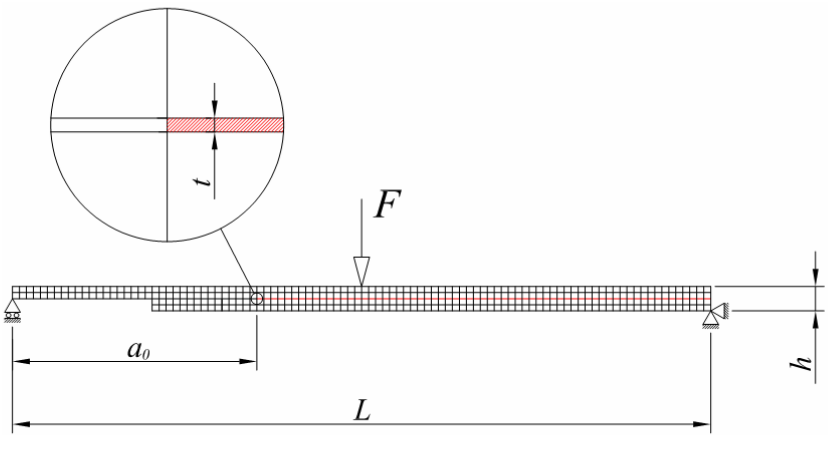

Figure 5.18 – Configuration of the SLB model

In the SLB model contact elements are not necessary, because there is not the possibility of compenetration between the edges of the crack.

The displacement is applied in the mid node of the upper surface of the model, whereas the other boundary conditions simulate the supports: the node that represent the right support has an imposed displacement equal to zero in both the direction horizontal and vertical, whereas the node that represent the left support has an imposed displacement equal to zero only in the vertical direction. All the other characteristics are the same described in the section 5.1. In figure 5.19 it is possible to see the undeformed and the deformed shape of the specimen during the simulation.

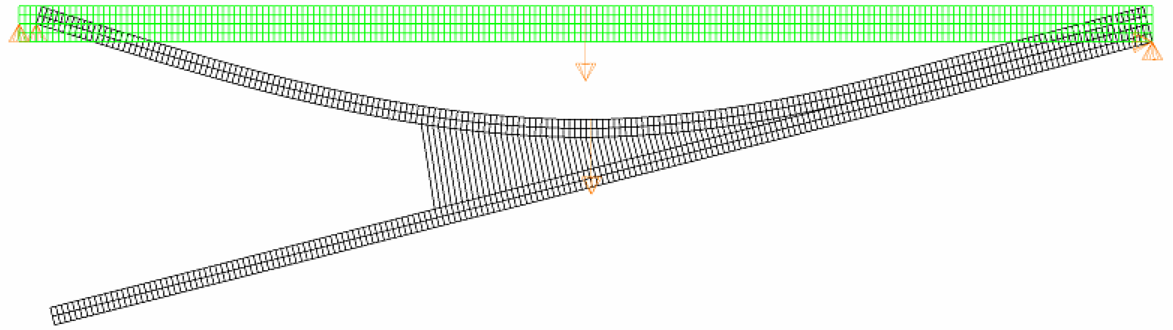

Figure 5.19 – Undeformed (green) and deformed (black) shape for the SLB test

The first result presented is the force-deflection curve, which in figure 5.20 is compared with the same curve obtained in the experimental tests. There is a good correspondence between the elastic branches of the two curves. In the propagation branch there is a difference between the experimental curve and the cohesive model smaller than in the DCB test, but bigger than the 4ENF test. This difference could be due to the bridging in the experimental specimen, which in the mixed mode is less relevant than in the mode I.

The figure 5.21 shows the length of the crack for some value of the relative displacement. The experimental curve has been already discussed in chapter 4. The two other curves shown, instead, related to the finite element model, are the length of the crack evaluated for $D=0$ and for $D=1$ as described in the section 5.1.2. The experimental curve, this time, is almost centred between the curves for $D=1$ and $D=0$.

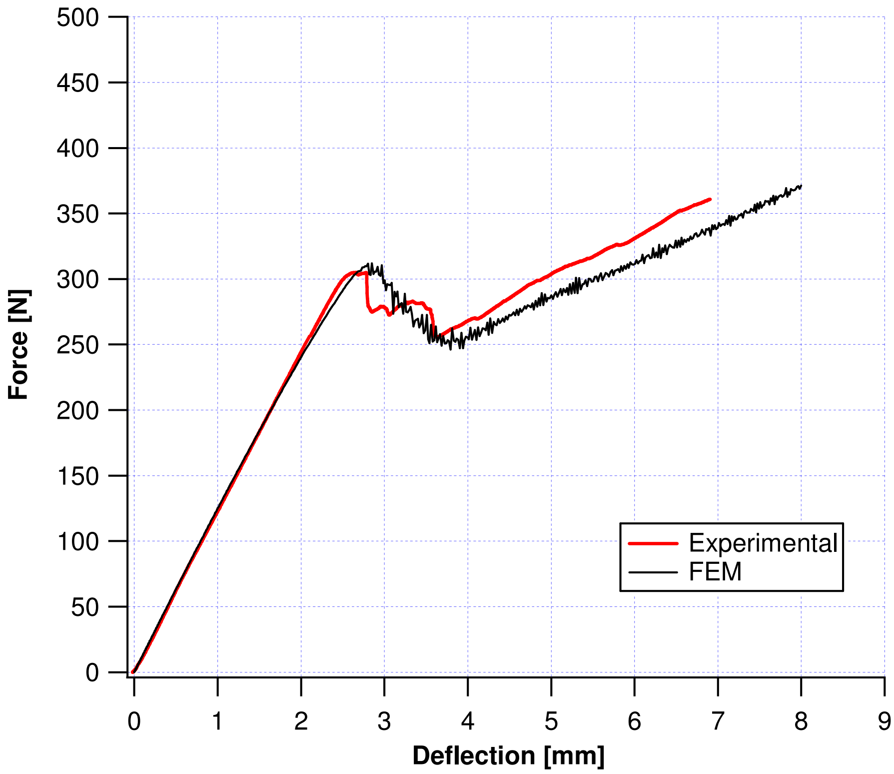

Figure 5.20 – Force vs. deflection curve for the SLB test: experimental and FEM

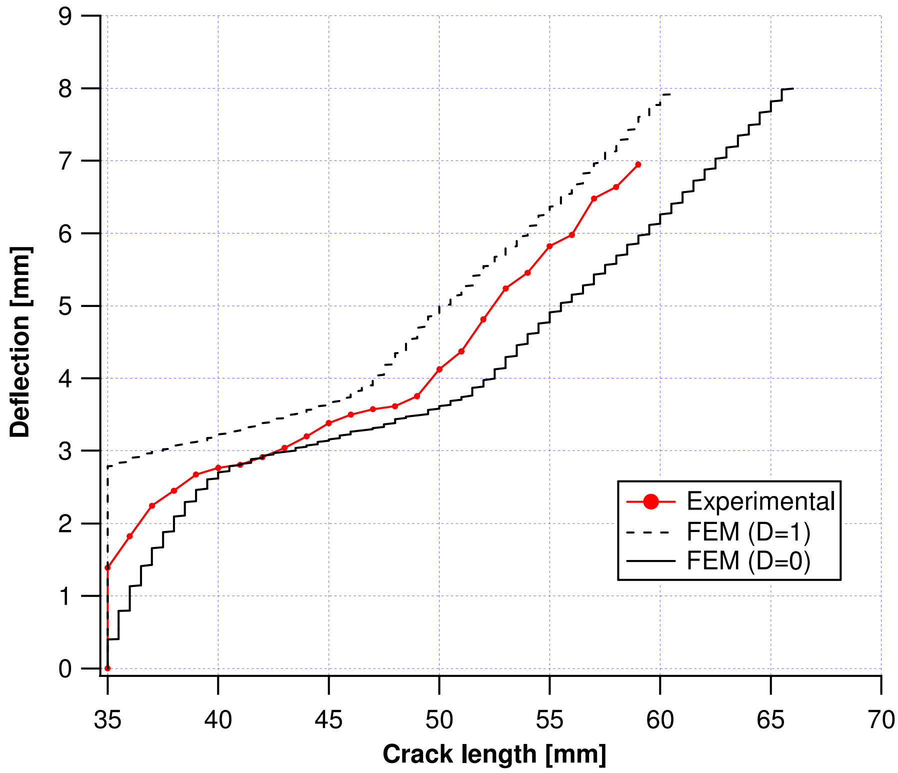

Figure 5.21 – Deflection vs. crack length curve for the SLB test: experimental and FEM

For the SLB test two analyses are presented. The first is a study of the sensitivity of the model to the grade of the propagation law used for describing the progression of the delamination, expressed by the equation 3.41. Practically the analysis consists in changing the exponent of the equation 3.41, letting it assume the values one and two, in order to understand if it is more reliable in predicting the propagation a linear or quadratic criterion.

The second analysis is the same already done for the previous models. It is a parametric study to evaluate the behaviour of the model when the interface stiffness changes.

The results of the analysis of the response of the model with the linear or quadratic progression of the damage are shown in the figures 5.22 and 5.23. The model with the linear progression is the same presented in figures 5.20 and 5.21.

In the figure 5.22, which shows the force-deflection curve for both the model, and in figure 5.23, which shows the deflection-crack curves, it is possible to observe a large difference between the two methods. Therefore the linear progression of the damage, already used in the DCB and 4ENF models, has been kept, because not only it makes the model more close to the experimental test, but it is also simpler.

The second analysis presented is the parametric one with respect to the interface stiffness. In the SLB test, which is a mixed mode test, both the values of G_{IC} and G_{IIC} have influence on the progression of the damage in dependence of the law described by the equation 3.41. Therefore variations of both K_N and K_S can have a considerable effect.

The problem, once decided to vary the interface stiffness, is how to vary the value for the mode I and II reciprocally.

Two possibilities are explored that are now described. The first consist in varying K_N and K_S by keeping for both the same ratio between the area before and the area after the elastic limit, with the same three values just described for the two previous tests.

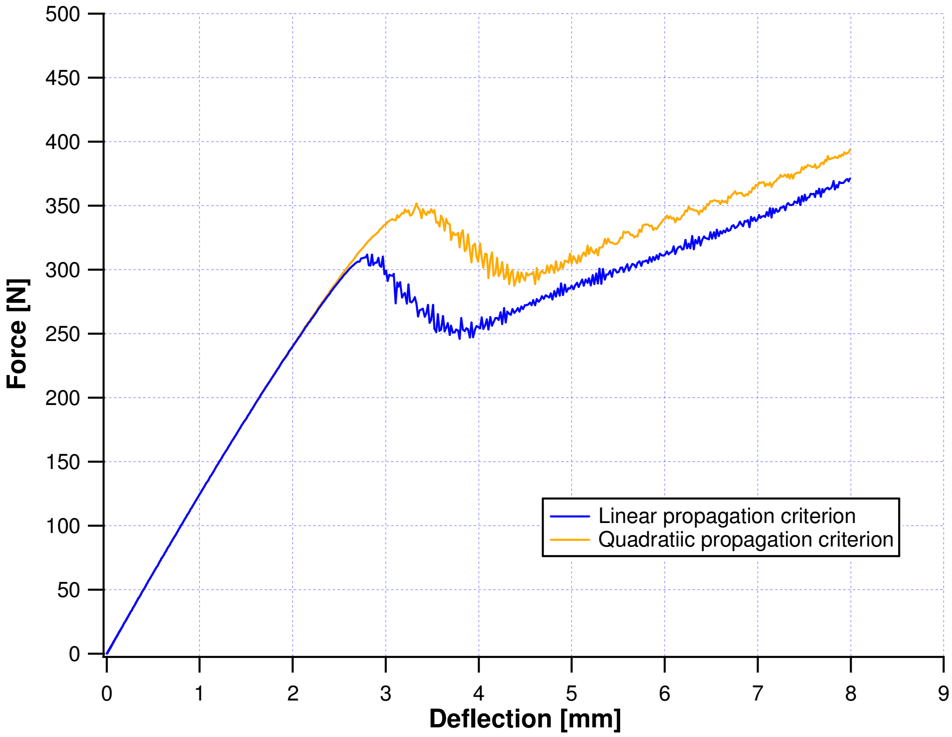

Figure 5.22 – Force vs. deflection curve for the SLB test: influence of the criterion for the damage progression

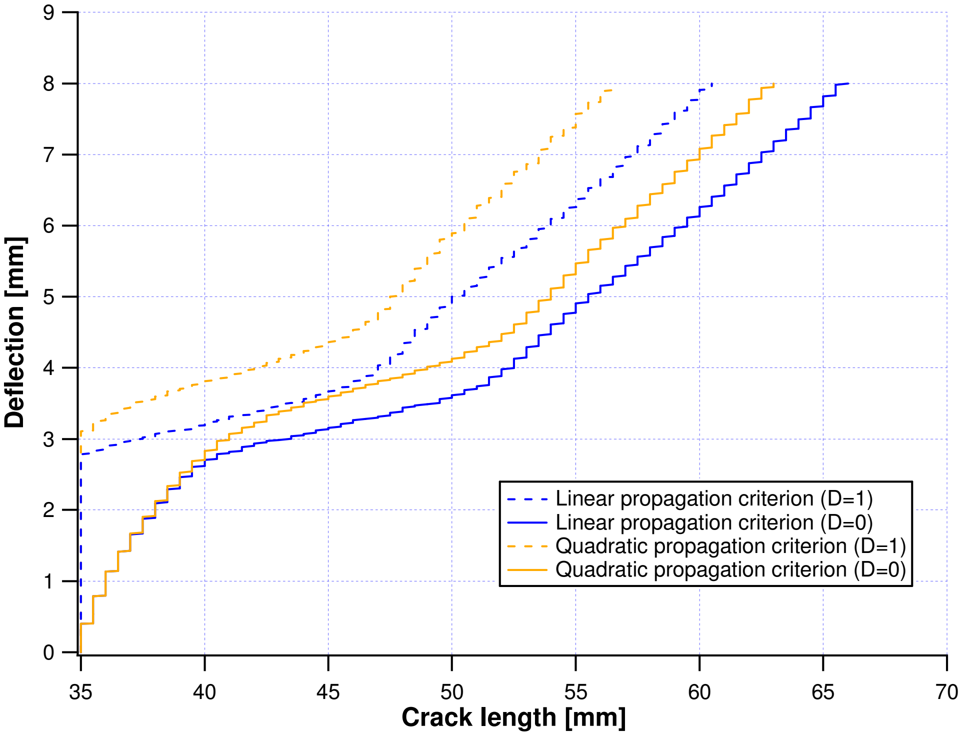

Figure 5.23 – Deflection vs. crack length curve for the SLB test: influence of the criterion for the damage progression

Three models were analysed with the values of K_N and K_S shown in table 5.6.

Model	Interface stiffness K_N [GPa/mm]	Interface stiffness K_S [GPa/mm]
1	120	42.9
2	0.622	1.77
3	0.345	0.983

Table 5.6 – Value of the interface stiffness for the mixed mode

In figure 5.24 and 5.25 respectively the curve force-deflection and the curve deflection-crack, evaluated for $D = 1$ and for $D = 0$, are shown for the three models.

It is possible to see in both the graphs a big difference between the model with the original values and the two others. The two models with the smaller slope, even if the ratio between the two areas of the triangle of the cohesive law is quite different, have a small difference in the interface stiffness, because the base of the triangle, which is the critical displacement δ_c, is long respect to the height of the triangle, which is the elastic limit σ_0.

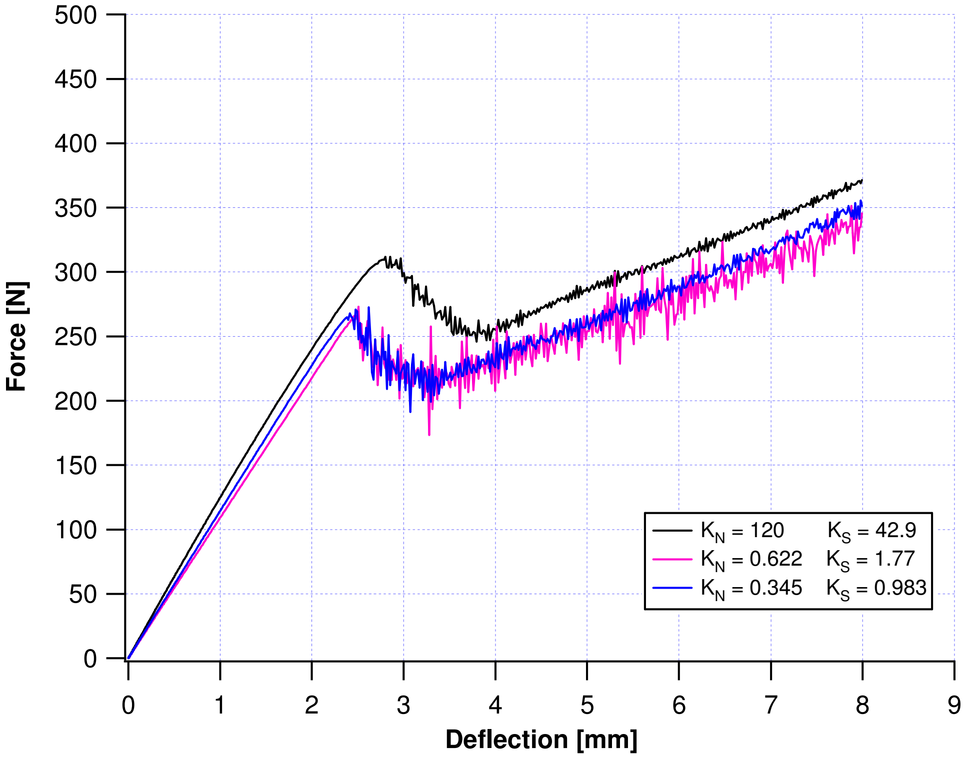

Figure 5.24 – Force vs. deflection curve for the SLB test: influence of the interface stiffness

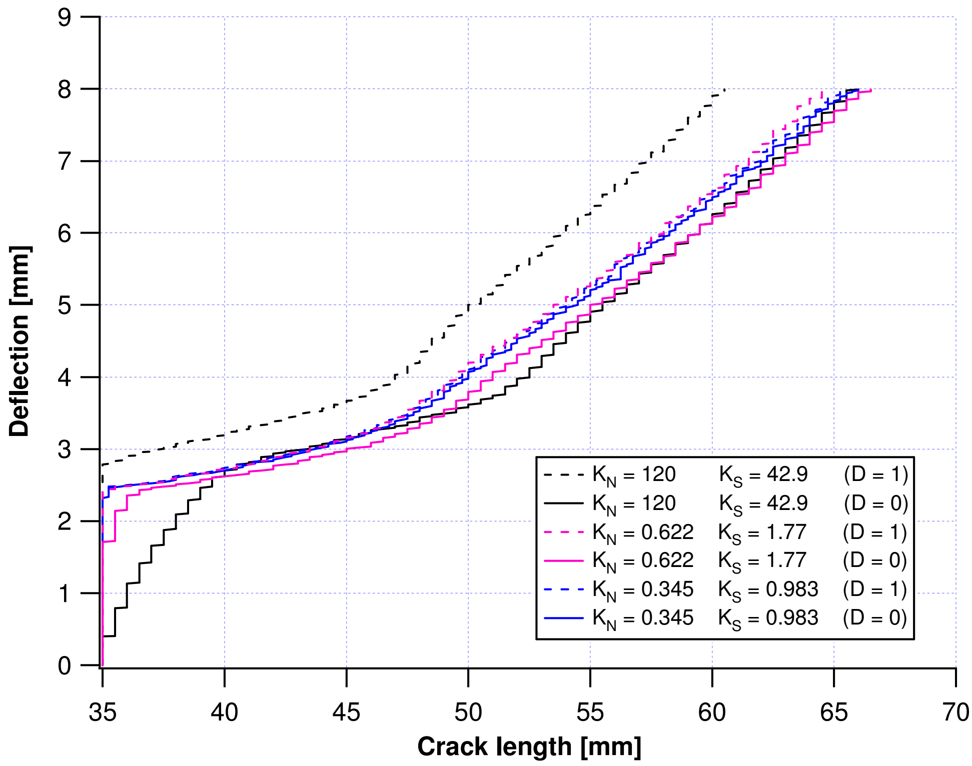

Figure 5.25 – Deflection vs. crack length curve for the SLB test: influence of the interface stiffness

The second way to vary the interface stiffness of the two models is to divide both the original K_N and K_S for the same whole number. Figure 5.26 shows the models that are discussed. The original values were divided by a factor equal respectively to 2, 8, 20 and 40. This attempt is made in order to keep the proportionality between the values of the interface stiffness for the mode I and for the mode II.

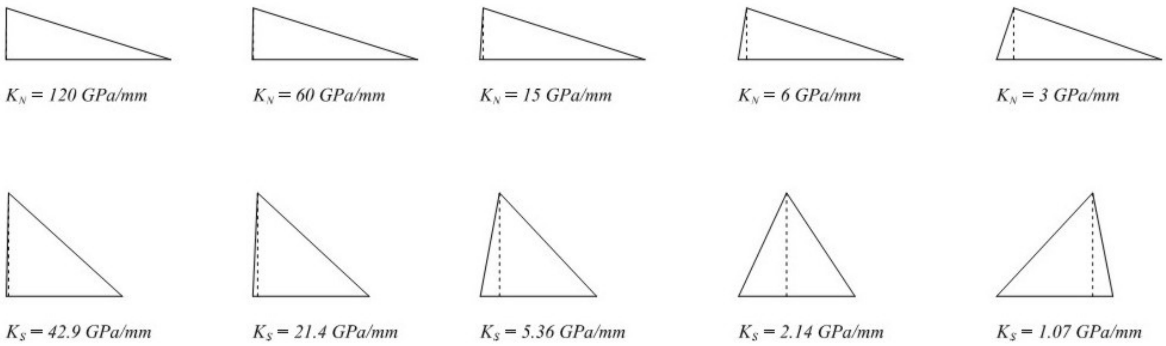

Figure 5.26 – Interface stiffness obtained by dividing the original K_N and K_S for a whole number

The figure 5.27 shows the force-deflection curve for the models studied in this parametric analysis. It is possible to see how the difference between the curves varies more slowly than the previous analysis, even if the variation of the interface stiffness is large, especially for the mode II.

The interface stiffness of the mode I, instead, is so steep in its original value that even when divided by a factor equal to forty the slope does not became shallow.

The response of the model indicates then a bigger sensitivity to the variation of the stiffness K_N of the mode I than of the stiffness K_S of the mode II.

The figures 5.28 and 5.29 show the length of the crack, for each model, evaluated for $D = 0$ and $D = 1$, respectively.

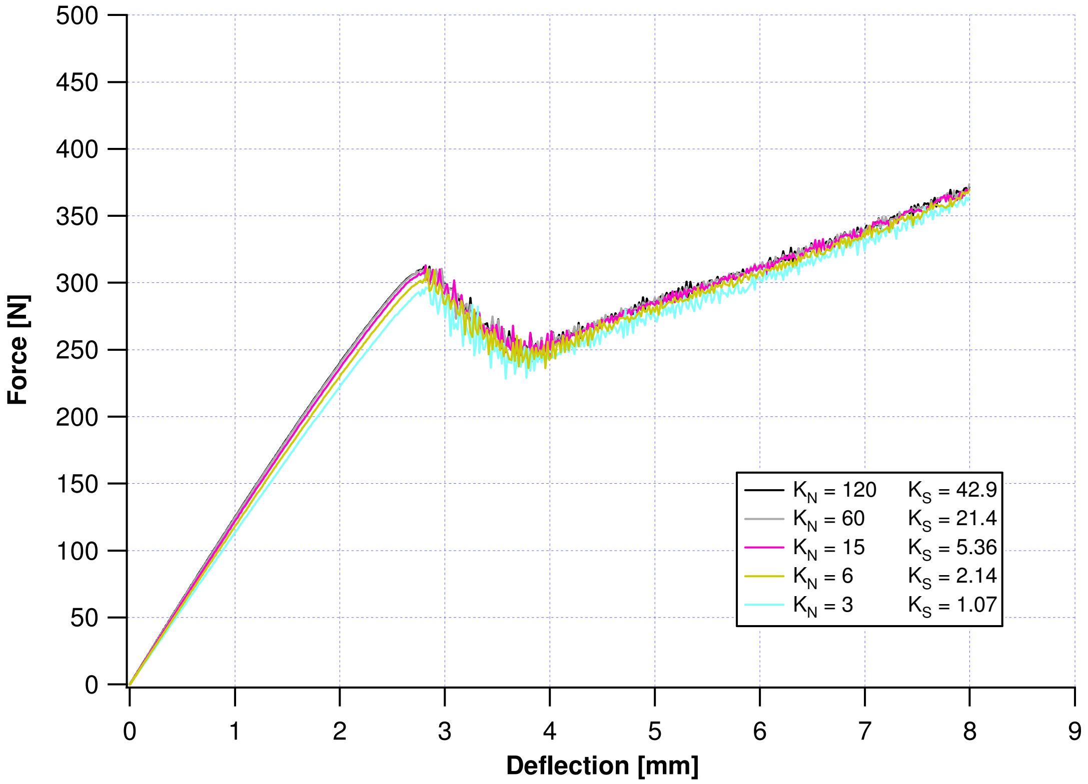

Figure 5.27 – Force vs. deflection curve for the SLB test: influence of the interface stiffness

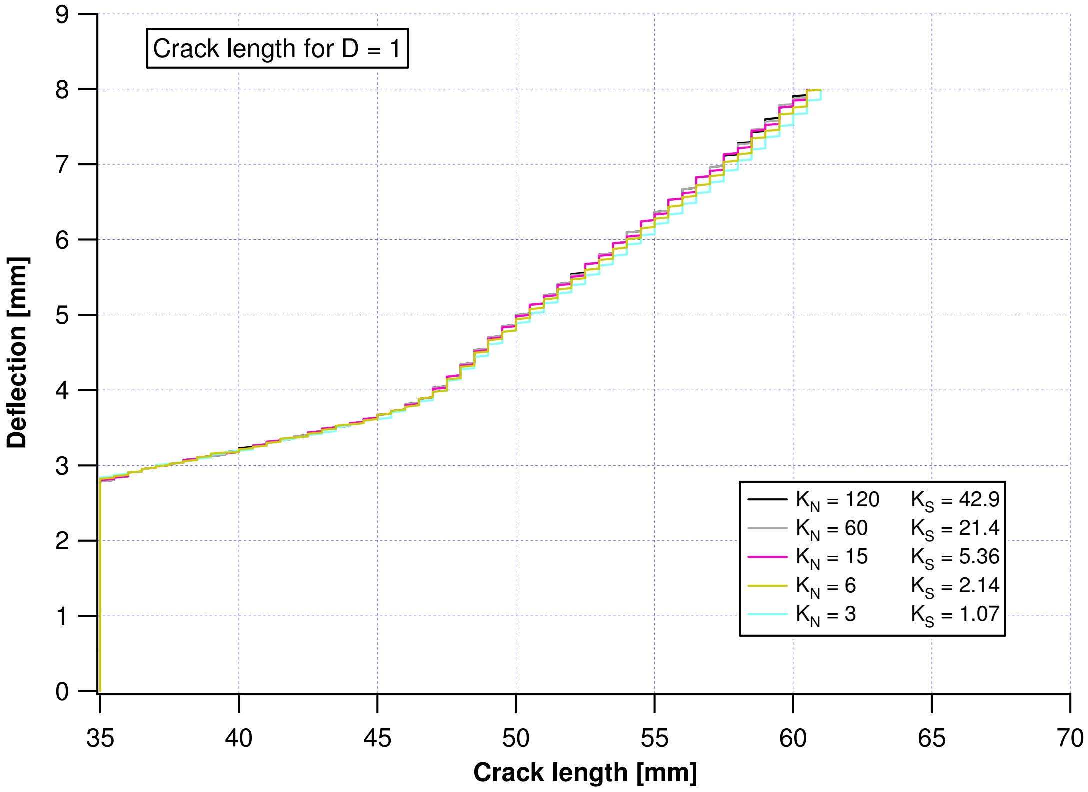

Figure 5.28 – Deflection vs. crack (D=1) curve for the SLB test: influence of the interface stiffness

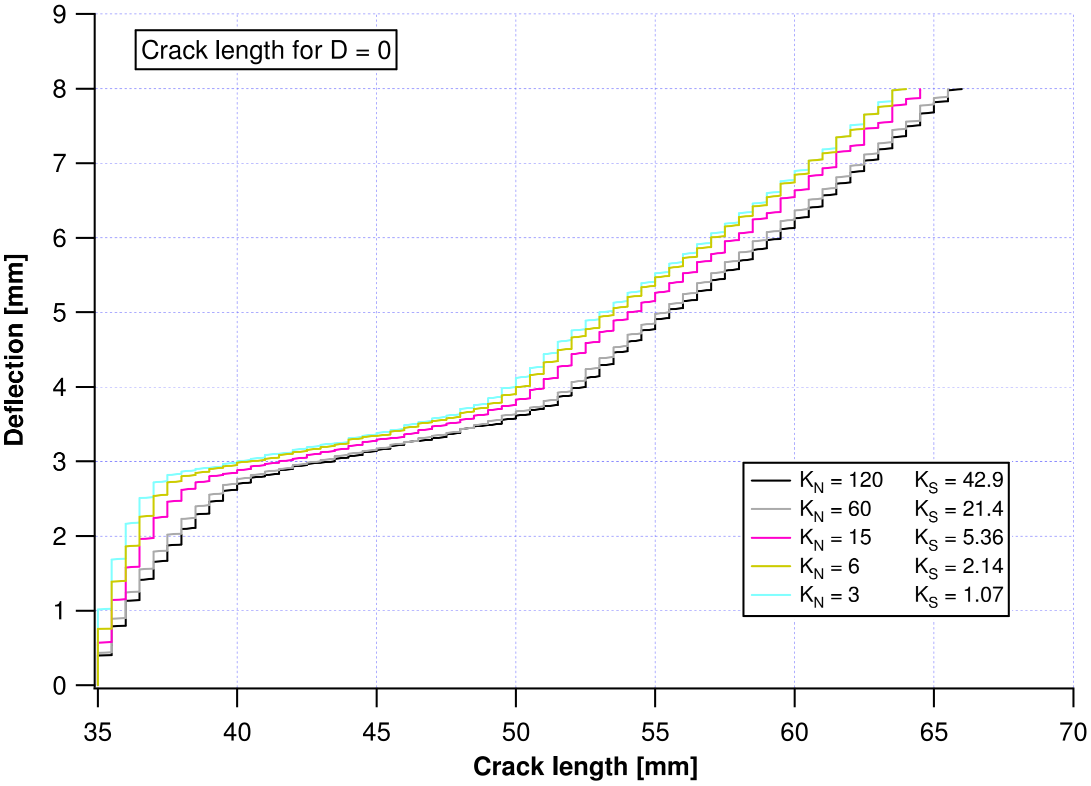

Figure 5.29 – Deflection vs. crack (D=0) curve for the SLB test: influence of the interface stiffness

5.3 Comments

This chapter presented a finite element modelling of the experimental tests described in the chapter 4, the test for the evaluation of the interlaminar toughness in pure mode I, which is the DCB test, in pure mode II, 4ENF test, and a test for the mixed mode, the SLB test.

The modelling allowed studying the potential of the cohesive interface elements for the prediction of delamination propagation under quasi-static loading.

For each model, firstly a comparison with the experimental tests has been done, with regard to the force versus displacement curve and the displacement versus crack length curve.

All the tests showed that a rather good accordance may be obtained between experimental data and numerical simulations with a proper choice of the main model parameters (critical fracture energies G_{IC} and G_{IIC}, interface stiffness and mesh density, in particular).

Subsequently, for each model, the sensitivity to the cohesive stiffness interface has been evaluated with a parametric analysis with respect to the stiffness. This analysis showed for the pure mode I and pure mode II a small influence of the initial stiffness of the cohesive interface on the behaviour of the laminates. The mixed mode, instead, is slightly influenced only if the interface stiffness, in the two modes, is reduced proportionally.

For the mixed mode, also the influence of the propagation criterion has been evaluated. The model has been tested with a linear and quadratic law. The linear law showed a good accordance with the experimental tests, and then it was chosen also for its simplicity.

Chapter 6

Delamination under fatigue loading

6.1 Introduction

In this chapter a simplified analytical model for the study of the delamination under fatigue loading is presented.

This model has been already developed [LGR07, L08] and in this thesis an implementation of this model in the programming language Matlab is presented.

This chapter presents another aspect of the study of delamination with respect to the previous chapters. In fact, the chapter four describes the experimental side of the study of delamination, the chapter five contains a comparison between the experimental tests and the finite elements modelling with cohesive elements, in order to evaluate the potential of these elements in the prediction of the delamination, whereas this chapter is a dissertation about a simplified method to predict the delamination both for static and fatigue loading.

The reason for studying new solutions for the prediction of the delamination under fatigue loading is that the increasing use of polymer matrix composites in many engineering fields is driving a demand for improved design methods.

The aim is to reduce the amount of expensive and time-consuming physical testing required during the development of a composite product and so a significant effort is being made to develop design tools which predict the complex failure modes which can occur in these materials.

Finite Element Analysis (FEA) is one of the most commonly used methods for the structural design of complex structures, but often the study of any strategy for this method requires lots of FE model runs.

In the present chapter a simple model is presented for a fast, systematic and rational evaluation of the performance of interface elements for fatigue induced delamination and propagation. The simple mathematical model does not involve any finite element mesh of the delaminating layers and therefore isolates the interface elements from the interaction with other parts of the mesh; this enables attention to be focused on three key aspects of modelling fatigue-driven delamination:

- Interface constitutive laws.
- Damage definitions.
- Fatigue degradation strategies.

The simple mathematical model is extremely efficient from a computational point of view so a large number of runs can be performed in a relatively short time and parametric studies involving hundreds of thousands of different sets of parameter values are possible.

6.2 Simplified model for delamination and quasi-static behaviour

6.2.1 Description of the model

This section describes the mathematical model, which consist in a cylinder of radius *R* that rolls on a surface composed by two zero-thickness layers.

In the initial state the two layers, which are called 'upper' and 'lower', as shown in figure 6.1, are coincident.

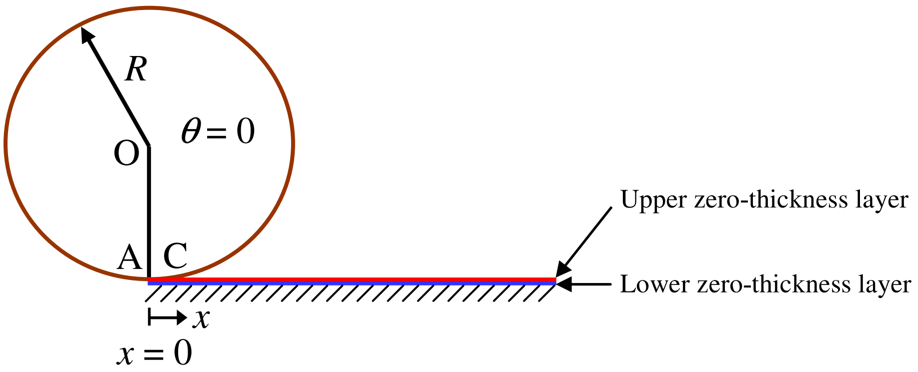

Figure 6.1 – Cylinder in the initial position

Under static loading, the cylinder rotates in a clockwise direction. The lower layer is fixed, whereas the upper layer adheres to the surface of the cylinder at the contact point, C, and remains adhered as the cylinder rotates and the contact point advances, as shown in figure 6.2.

The two layers are connected by a system of vertical springs, that are distant each other of the same quantity *Δl*. All the springs in a position in which the two layers are yet coincident, starting from the spring in correspondence to the contact point, are not stressed, whereas as soon as the two layers start to separate the springs became stressed.

A reference system *x* has been chosen, starting from the left hand edge of the zero-thickness layers, such that *x*=0 when the contact point is in the initial position. The position *x*=0 is also the position of the first spring.

The rotation of the cylinder can be described with the angle *θ*, that it is also equal to zero in the initial position. The line OA on the cylinder cross section (as shown in figure 6.1) is vertical in this initial configuration and as the cylinder rolls along the horizontal surface the angle swept through by OA is the rotation, *θ*, of the cylinder (as shown in figure 6.2).

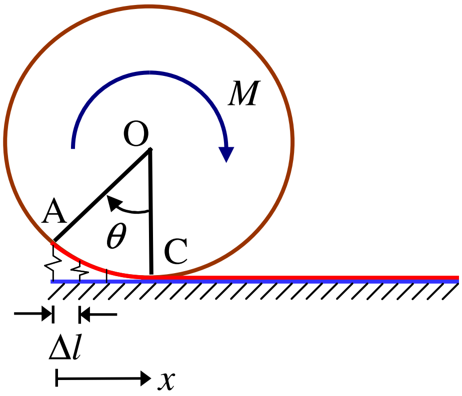

Figure 6.2 – Cylinder after a rotation *θ*

When the clockwise moment is applied the cylinder rotates in the same direction and the upper layer, which adheres to the cylinder, will separate from the lower layer.

The springs will react to this separation and will be activated, elongating and offering resistance to the change of rotation.

In this model the springs have the same role of the interface elements in the Finite Element method. Each spring has a constitutive law, the same for all the springs, which will be discussed later. This constitutive law enables the force in the spring to eventually reduce to zero (representing total interlaminar failure) as the layer separation increases.

It is important to say that the value of R has to be very large with respect to the maximum elongation of a spring in order to be able to consider the position of the spring vertical during its elongation.

6.2.2 Kinematics

This model has only one degree of freedom, which is the rotation θ of the cylinder. As it has been already said, when the contact point is in the initial condition, the value of the angle is $\theta = 0$ and the coordinate of the contact point is $x_{con}=0$.

After a change in rotation of the cylinder so that $\theta > 0$ the coordinate of the contact point is given by

$$x_{con}=\theta R \tag{6.1}$$

The coordinate of the contact point represent also the length of the crack. Once this length is known, it is possible to determinate the number (n) of the springs from the origin of the coordinate system to the contact point by calculating the integer part (denoted by the square brackets [ ]) of the result of the following expression:

$$n = [x_{con}/\Delta l]+1 \tag{6.2}$$

It is possible to identify the individual springs then the position of each spring with respect to the origin, after have defined the sub-index i to vary from 1 to n, by

$$x_i=(i-1)\Delta l \tag{6.3}$$

The angle (ω_i) measured at the centre of the cylinder which locates the top of the i-th spring with respect to the vertical through the current contact point is obtained, as it is possible to see in figure 6.3, from:

$$\omega_i = \sin^{-1}\left(\frac{x_{con} - x_i}{R}\right) \qquad x_i \le x_c \tag{6.4}$$

The springs have a zero initial height, and then the elongation will be defined as the vertical displacement (δ_i) of the top of the spring using the following equation:

$$\delta_i = R(1-\cos\omega_i) \tag{6.5}$$

The distance of the spring to the current contact point is given by

$$d_i = x_{con} - x_i \tag{6.6}$$

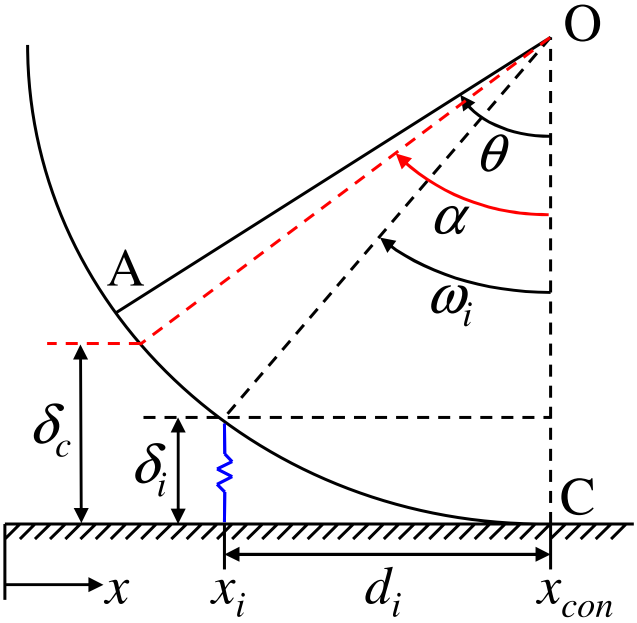

Figure 6.3 – Geometry of the model

As it has been already said, depending on the constitutive law, the response of each spring can degrade as the displacement is increased until the spring force reduces to zero. If the opening displacement at which failure occurs is called critical displacement (δ_c), it is possible to determinate the angle, called critical angle (α), by the following expression:

$$\alpha = \cos^{-1}\left(\frac{R - \delta_c}{R}\right) \tag{6.7}$$

6.2.3 Equilibrium and critical applied moment

When a rotation is applied to the cylinder, some springs become active. It is possible to obtain, for each spring, the interface stress (σ_i), which is a function of the displacement ($\sigma_i = f(\delta_i)$), by using an interface constitutive law.

By multiplying the interface stress σ_i associated with each spring by the area which the spring 'represents' it is possible to find the spring force (F_i). It has been supposed that the cylinder has a unit width, and then the interface area associated with a typical spring is $1 \cdot \Delta l$ whereas the area of the first spring is taken as $1 \cdot \Delta l/2$. The value of the force for one spring is given by

$$F_i = \sigma_i \cdot \Delta l \cdot 1 \tag{6.8}$$

The moment (M_i), respect to the contact point, generated by the spring is obtained by multiplying the force by the distance to the current contact point

$$M_i = F_i \cdot d_i \tag{6.9}$$

and it is possible to obtain the total moment (M_t) generated by the springs by summing all the moments M_i of all the active springs

$$M_t = \sum_{i=1}^{n} M_i \tag{6.10}$$

This is the magnitude of the moment which has to be applied to the cylinder in order to maintain the cylinder in equilibrium for a given applied rotation.

The quasi-static monotonically applied moment required to delaminate the two zero-thickness layers can be determined in terms of the toughness (G_c) of the interface between the two layers [G21]. An expression for the critical moment (M_c) can be determined by considering an energy balance as the point of contact moves through an infinitesimal distance dx. The change in rotation of the cylinder corresponding to such a movement is dx/R and so equating the external work to the energy consumed in separating the layers gives

$$M_c \frac{dx}{R} = 1 \cdot dx G_c \tag{6.11}$$

which can be rewritten as

$$M_c = G_c R \tag{6.12}$$

6.2.4 Interface constitutive laws

As it was mentioned previously, a constitutive law is required to describe the behaviour of σ as a function of δ in interface elements. The constitutive law should be defined in such a way that for every value of δ there is a unique value of σ.

In this research three different interface constitutive laws have been analyzed:

- Bilinear law.
- Third order polynomial law.
- Mixed law.

Only the constitutive behaviour for mode I monotonic increasing relative opening displacement will be described in the next sub-sections.

Even if the three laws are different there are some common aspects. In particular, for all the three laws three parameters have to be defined in order to define the law.

The first parameter is the critical displacement value (δ_c) that is the maximum displacement before which the stress in the spring became equal to zero and the spring gives no more contribution to the resistance to the separation between the two layers of the surface.

Another parameter is the maximum stress value (σ_0) which is the maximum stress that a spring can reach.

The third parameter is the critical energy release rate (G_c). The critical energy release rate is a criterion used in linear elastic fracture mechanics for the propagation of the delamination in the interface. It is indirectly used by equating the areas under the stress-displacement curves to the critical energy release rates.

The value of the release of energy (G) for a generic displacement can be evaluated as area under the stress-displacement curve for that displacement. The critical energy release rate (G_c) is the value of G corresponding to the critical displacement.

Bilinear interface constitutive law

The bilinear interface law is shown in figure 6.4. For this law it is necessary to define another parameter more than the three defined in the previous paragraph. The parameter is δ_0, which is the displacement corresponding to the value of stress of σ_0.

This law can be considered formed from three parts: linear elastic stage, stiffness degradation and failure. In the first part a linear-elastic behaviour is assumed until the relative opening displacement reaches the elastic limit δ_0 and the stress assumes its maximum value, σ_0. The linear-elastic part of the law is described by the following expression:

$$\sigma = K\,\delta \qquad 0 \leq \delta \leq \delta_0 \tag{6.13}$$

where K is the stiffness and it has the following expression

$$K = \sigma_0 / \delta_0 \tag{6.14}$$

The second part of the interface constitutive law defines the behaviour between the elastic limit and the critical displacement δ_c. Once the elastic limit is exceeded the interface element starts to be degraded. This degradation is described by the following relationship:

$$\sigma = \sigma_0 \left(\frac{\delta_c - \delta}{\delta_c - \delta_0} \right) \qquad \delta_0 < \delta < \delta_c \tag{6.15}$$

The last part of the law is for equal or bigger displacements than the critical displacement δ_c. When this value is reached the stress became equal to zero and there is no more possibility of reaction of the interface.

$$\sigma = 0 \qquad \delta \geq \delta_c \tag{6.16}$$

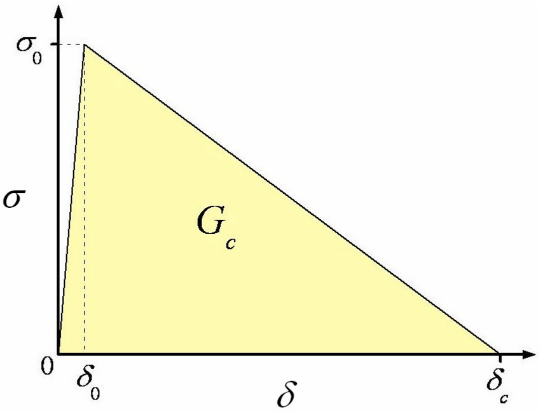

Figure 6.4 – Mode I bilinear constitutive law

The value of *G*, energy release rate for a generic relative displacement, has the same value of the area under the curve for that displacement. The expression is the following:

$$G = \frac{1}{2} \cdot \delta \cdot \sigma \qquad 0 \leq \delta \leq \delta_0 \tag{6.17}$$

$$G = \frac{1}{2} \cdot [\delta_0 \cdot \sigma_0 + (\delta - \delta_0) \cdot (\sigma + \sigma_0)] \qquad \delta_0 < \delta < \delta_c \tag{6.18}$$

$$G = \frac{1}{2} \cdot \delta_c \cdot \sigma_0 \qquad \delta \geq \delta_c \tag{6.19}$$

The critical energy release rate G_c is equal to the total area under the $\delta - \sigma$ curve, that is represented by the equation 6.19, so, in this case,

$$G_c = \frac{\delta_c \sigma_0}{2} \tag{6.20}$$

The bilinear constitutive law is therefore completely defined once have been assigned the value of δ_0 and two out three values of G_c, δ_c and σ_0.

Third-order polynomial interface constitutive law

The third-order polynomial interface constitutive law, shown in figure 6.5, eliminates the discontinuities that exist in the bilinear law. This law has been proposed by Needleman [N87] and it has been adapted by Pinho et al. [PIR06] to interface elements.

This law has a slope equal to zero at the maximum stress value σ_0 and at the critical displacement value δ_c. The maximum stress σ_0 is not more in correspondence of the elastic limit δ_0, which does not exist more, but it is at a displacement $\delta=(\delta_c/3)$.

It is possible to see this from the equation of the curve of the law that, in accord to the name of the law, is a third-order polynomial function with the following expression:

$$\sigma = \frac{27}{4}\sigma_0\left(1-\frac{\delta}{\delta_c}\right)^2\frac{\delta}{\delta_c} \qquad 0 \le \delta \le \delta_c \tag{6.21}$$

Like the bilinear law, as soon as the critical displacement δ_c is reached, the stress in the interface element became zero. The condition is the following

$$\sigma = 0 \qquad \delta > \delta_c \tag{6.22}$$

The stiffness K, in the polynomial law, has the following expression:

$$K = \frac{27}{4}\frac{\sigma_0}{\delta_c} \tag{6.23}$$

The value of the energy release (G) for a generic displacement is given by the area under the curve until that displacement, with the following expression:

$$G = \frac{27}{4} \cdot \sigma_0 \cdot \left(\frac{\delta^2}{2 \cdot \delta_c} + \frac{\delta^4}{4 \cdot \delta_c^3} - \frac{2}{3} \cdot \frac{\delta^3}{\delta_c^2} \right) \qquad 0 \le \delta \le \delta_c \qquad (6.24)$$

$$G = \frac{27}{48} \cdot \delta_c \cdot \sigma_0 \qquad \delta > \delta_c \qquad (6.25)$$

The value of the critical energy release, G_c, is the same value of the total area under the curve, and then the expression is equal to the equation 6.25:

$$G_c = \frac{27}{48} \delta_c \sigma_0 \qquad (6.26)$$

This law is completely defined if two out of three parameters G_c, δ_c, σ_0 are defined, because only two of those are independent.

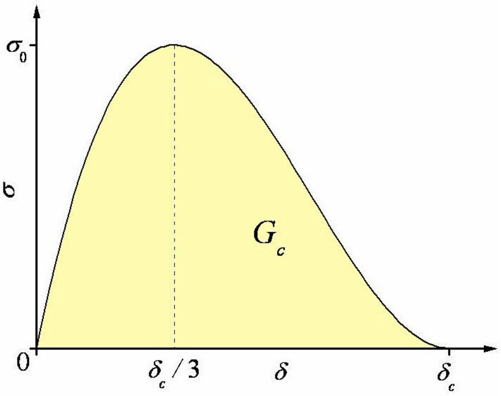

Figure 6.5 - Mode I third-order polynomial constitutive law

Linear-polynomial mixed interface constitutive law

The mixed law, proposed by Pinho et al. [PIR06], is a linear-polynomial law and can be defined as a combination of the two previous laws. As it is possible to see in figure

6.6, this law can be considered in three parts, like the bilinear law: linear elastic, stiffness degradation and failure. In the first part a linear-elastic behaviour is assumed until the relative opening displacement reaches the elastic limit δ_0 and the stress assumes its maximum value, σ_0. The linear-elastic part of the law is described by the following expression:

$$\sigma = K\,\delta \qquad 0 \leq \delta \leq \delta_0 \tag{6.27}$$

where K is the stiffness and is given by

$$K = \sigma_0 / \delta_0 \tag{6.28}$$

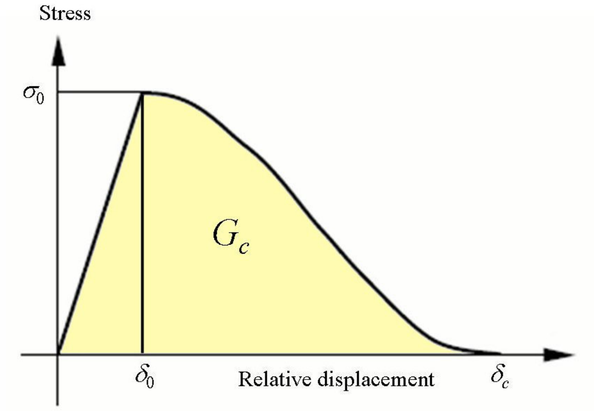

Figure 6.6 – Mixed linear-polynomial interface constitutive law

The second part of the interface constitutive law defines the behaviour between the elastic limit δ_0 and the critical displacement δ_c.

Once the elastic limit is exceeded the interface element starts to be degraded. This degradation is described by the following polynomial law:

$$\sigma = \left[1 + \left(\frac{\delta - \delta_0}{\delta_c - \delta_0}\right)^2 \left(2\frac{\delta - \delta_0}{\delta_c - \delta_0} - 3\right)\right] K\delta_0 \qquad \delta_0 \leq \delta \leq \delta_c \tag{6.29}$$

The third and last part of the interface constitutive law is for relative displacement values that are equal or larger than the critical displacement value. When this critical value is reached or exceeded the element fails so that no stress can be carried by the interface:

$$\sigma = 0 \qquad \delta \geq \delta_c \tag{6.30}$$

The expression of the energy release G for a generic displacement is the following:

$$G = \frac{1}{2} \cdot \delta \cdot \sigma \qquad 0 \leq \delta \leq \delta_0 \tag{6.31}$$

$$G = \frac{1}{2} \cdot \delta_0 \cdot \sigma_0 + \frac{\sigma_0}{2 \cdot (\delta_c - \delta_0)^3} \cdot \left[\delta^4 - 2 \cdot (\delta_0 + \delta_c) \cdot \delta^3 + 6 \cdot (\delta_0 \cdot \delta_c) \cdot \delta^2 + \right.$$

$$\left. + 2 \cdot (\delta_c^3 - 3 \cdot \delta_0 \cdot \delta_c^2) \cdot \delta + \delta_0^4 - 4 \cdot \delta_0^3 \cdot \delta_c - 2 \cdot \delta_0 \cdot \delta_c^3 + 6 \cdot \delta_0^2 \cdot \delta_c^2 \right] \qquad \delta_0 < \delta < \delta_c \tag{6.32}$$

$$G = \frac{1}{2} \cdot \delta_c \cdot \sigma_0 \qquad \delta \geq \delta_c \tag{6.33}$$

Also in the mixed law the value of G_c, energy release rate, is the value of the total area under the curve. The expression is the following:

$$G_c = \frac{\delta_c \sigma_0}{2} \tag{6.34}$$

6.2.5 Damage formulations

Each of the interface constitutive laws presented in the previous paragraph can be expressed in terms of a damage parameter *D*. The reason for which is convenient to do this is that the fatigue formulation operates through the definition of the damage parameter.

In accord to Lemaitre and Chaboche [LC94], a surface or a volume is considered damaged if there are respectively discontinuities in the form of micro-cracks or discontinuities in the form of cavities in a considered volume element. If there are not any cracks and cavities at the microscopic scale the material is considered not damaged. The final damage state is reached when the considered volume element is completely fractured.

The theory of damage describes the evolution of the constitutive behaviour of the material between the undamaged state and macroscopic crack initiation.

Since it is not possible to measure directly the damage its evaluation is related to the definition of a variables chosen to represent it. A simple way to describe the damage is to introduce a scalar variable *D* which is a non decreasing quantity. The damage parameter is usually defined in such way that for the undamaged state it is equal to zero and for the failure state it is equal to unity, as shown in the following expression:

$$\left| \begin{array}{cc} D = 0 & \textit{undamaged} \\ 0 < D < 1 & \textit{damaged} \\ D = 1 & \textit{failed} \end{array} \right. \qquad (6.35)$$

The constitutive interface laws described in the previous paragraph do not include explicitly the damage parameter *D* just described, but it is possible to write them in terms of this parameter. The damage parameter, as it will be described in section 6.3.3., is considered divided in two components: the static damage D_s and the fatigue damage D_f.

In this section only the static component of the damage D_s is described. For the static damage, three different formulations have been analyzed:

- Stiffness degradation.
- Energy consumed.
- Work done.

For the static damage all the three damage formulations are applied to the bilinear, the third-order polynomial and to the linear-polynomial mixed law, whereas in the fatigue damage formulation the stiffness degradation will be applied to both the bilinear and the third-order polynomial constitutive laws, while the other two damage formulations are applied only to the bilinear constitutive law. The mixed law will not be used for the fatigue.

Only the constitutive behaviour for mode I monotonic increasing relative opening displacement will be described in the next sub-sections.

Stiffness degradation based damage for the bilinear interface law

In this approach the static damage parameter, D_s, can be considered a measure of the degradation of the initial stiffness, and the bilinear law can be expressed as follow:

$$\sigma = (1-D_s)\, K\delta \tag{6.36}$$

The expression of the damage parameter D_s can be obtained by equating the equation 6.36 to the expression of each part of the bilinear law, respectively the equation 6.13, which is the linear elastic stage, the equation 6.15, which is the degradation part and the equation 6.16, which represents the failure.

As it is possible to see in the equation 6.37, the value of the damage parameter is zero in the elastic part of the law, when there is no damage, it decrease with linear law in the degradation part and it became equal to unity after that the stress has become null.

$$D_s = \begin{cases} 0 & 0 \le \delta \le \delta_0 \\ \left(\dfrac{\delta - \delta_0}{\delta}\right)\left(\dfrac{\delta_c}{\delta_c - \delta_0}\right) & \delta_0 < \delta < \delta_c \\ 1 & \delta \ge \delta_c \end{cases} \tag{6.37}$$

Stiffness degradation based damage for the third-order polynomial interface law

The formulation of the damage parameter for the polynomial law using the stiffness degradation follows the same principle of the bilinear law. Comparing the equation 6.36, which is also in this case the general form of the law, respectively with the equation 6.21, that is the equation of the curve, and with the equation 6.22, that represents the failure after the maximum displacement δ_c, the expression of the damage parameter is the following:

$$D_s = \begin{cases} 2\dfrac{\delta}{\delta_c} - \left(\dfrac{\delta}{\delta_c}\right)^2 & 0 \le \delta < \delta_c \\ 1 & \delta \ge \delta_c \end{cases} \tag{6.38}$$

It is interesting to observe that in the polynomial law, differently from the bilinear law and also from the mixed law, which will be shown in the next subparagraph, the damage starts to exist as soon as the displacement is bigger than zero.

Stiffness degradation based damage for the linear-polynomial mixed interface law

As for the two previous laws, it is possible to write the bilinear law in terms of the damage variable by equating the equation 6.36, which is also in this case the general form of the law, to the expression of each part of the mixed law, respectively the equation 6.27, which is the linear elastic stage, the equation 6.29, which is the polynomial degradation part and the equation 6.30, which represents the failure. The expression of the damage parameter is the following:

$$D_s = \begin{cases} 0 & 0 \le \delta \le \delta_0 \\ 1 - \dfrac{\delta_0}{\delta} \cdot \left[1 + \left(\dfrac{\delta - \delta_0}{\delta_c - \delta_0} \right)^2 \cdot \left(2 \cdot \dfrac{\delta - \delta_0}{\delta_c - \delta_0} - 3 \right) \right] & \delta_0 < \delta < \delta_c \\ 1 & \delta \ge \delta_c \end{cases} \qquad (6.39)$$

Energy consumed based damage for the bilinear interface law

If an interface, modelled by the bilinear law, is stressed until a point A, where $\delta > \delta_0$, as shown in figure 6.7, and then unloaded, it is assumed that an elastic unloading happens with a reduced stiffness, which represents the secant slope from point A to the origin.

If the same relative displacement δ is now reached again, the spring will be loaded along the same straight line, with the reduced slope, until it reaches again the point *A*.

This means that some energy has been consumed and this energy per unit area is represented by the triangle delimited by the original loading path and the unloading line *A0*.

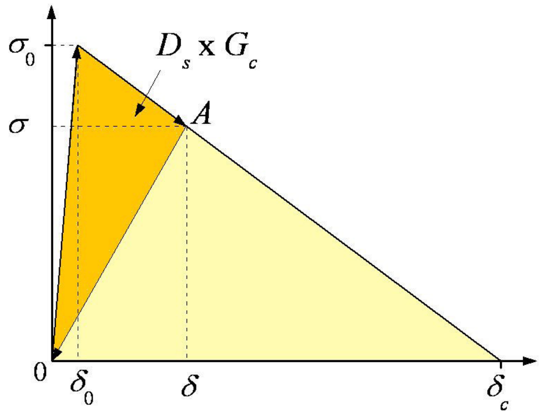

Figure 6.7 – Damage formulation based on the energy consumed

If damage is defined as a ratio between the area of the above triangle and the area under the entire constitutive law, equal to G_c, the expression of the static damage (D_s) is the following:

$$D_s = \begin{cases} 0 & 0 \le \delta \le \delta_0 \\ \left(\dfrac{\delta - \delta_0}{\delta_c - \delta_0} \right) & \delta_0 < \delta < \delta_c \\ 1 & \delta \ge \delta_c \end{cases} \tag{6.40}$$

Using this definition of D_s, equations 6.13, 6.15 and 6.16 can be rewritten as

$$\sigma = \begin{cases} K\delta & 0 \le \delta \le \delta_0 \\ (1 - D_s)\sigma_0 & \delta_0 < \delta < \delta_c \\ 0 & \delta \ge \delta_c \end{cases} \tag{6.41}$$

It is possible to see from equation 6.40 that the growth of the energy-consumed damage is a linear function of the relative displacement applied to the spring.

Energy consumed based damage for the third-order polynomial interface law

It is possible to write the polynomial law in terms of damage variable by using the energy consumed based definition of the damage and applying the same considerations of the bilinear law with the energy consumed damage definitions.

The damage parameter can be defined as ratio between the two following areas:

- The area included under the curve of the law and above the line that links the origin with a generic point on the curve corresponding to a generic displacement.
- The total area under the curve, that is G_c.

The expression of the static damage is the following:

$$D_s = \begin{cases} \left[3 \cdot \left(\frac{\delta}{\delta_c} \right)^4 - 8 \cdot \left(\frac{\delta}{\delta_c} \right)^3 + 6 \cdot \left(\frac{\delta}{\delta_c} \right)^2 \right] & 0 \le \delta < \delta_c \\ 1 & \delta \ge \delta_c \end{cases} \tag{6.42}$$

The expression 6.21 and 6.22, in terms of damage, can be written in the following way:

$$\sigma = \begin{cases} (1 - D_s) \cdot K \cdot \delta + \left[\left(\frac{\delta}{\delta_c} \right)^2 - 2 \cdot \left(\frac{\delta}{\delta_c} \right) + D_s \right] \cdot K \cdot \delta & 0 \le \delta < \delta_c \\ 0 & \delta \ge \delta_c \end{cases} \tag{6.43}$$

Energy consumed based damage for the linear-polynomial mixed interface law

It is possible to write the mixed law in terms of damage variable by using the energy consumed based definition of the damage and applying the same considerations of the bilinear law with the energy consumed damage definitions.

The damage parameter can be defined as ratio between the two following areas:

- The area included under the curve of the law and above the line that links the origin with a generic point on the curve corresponding to a generic displacement.
- The total area under the curve, that is G_c.

The expression of the static damage, D_s, is the following:

$$D_s = \begin{cases} 0 & 0 \leq \delta \leq \delta_0 \\ \dfrac{1}{\delta_c \cdot (\delta_c - \delta_0)^3} \cdot \left[-\delta^4 + (\delta_0 + \delta_c) \cdot \delta^3 + (\delta_c^3 - 3 \cdot \delta_0 \cdot \delta_c^2) \cdot \delta + \right. & \\ \qquad \left. + 3 \cdot \delta_0^2 \cdot \delta_c^2 - \delta_0 \cdot \delta_c^3 - \delta_0^3 \cdot \delta_c \right] & \delta_0 < \delta < \delta_c \\ 1 & \delta \geq \delta_c \end{cases} \tag{6.44}$$

Work done based damage for the bilinear interface law

The work done per unit area necessary to separate an interface by δ is the area under the δ-σ curve up to that displacement. The work done is shown in figure 6.8 in a darker color and clearly further work must be done to completely fail the interface.

The remaining work to be done per unit area (G_r) to fail the interface is given by

$$G_r = \frac{\sigma(\delta_c - \delta)}{2} \qquad \delta_0 < \delta < \delta_c \tag{6.45}$$

The damage parameter based on the work done per unit area can be defined as

$$D_s = \begin{cases} 0 & 0 \leq \delta \leq \delta_0 \\ \left(\dfrac{G_c - G_e - G_r}{G_c - G_e} \right) & \delta_0 < \delta < \delta_c \\ 1 & \delta \geq \delta_c \end{cases} \tag{6.46}$$

where G_e is the area under the elastic stage of the σ–δ graph (right-angled triangle of base 0-δ_0 and height σ_0 in figure 6.8).

If σ is replaced from equation 6.15 in equation 6.29 and the expression of G_c from equation 6.20 is used, the equation 6.46 can be rewritten as

$$D_s = \begin{cases} 0 & 0 \le \delta \le \delta_0 \\ 1 - \left(\dfrac{\delta_c - \delta}{\delta_c - \delta_0} \right)^2 & \delta_0 < \delta < \delta_c \\ 1 & \delta \ge \delta_c \end{cases} \tag{6.47}$$

and the value of the stress for any spring using this damage definition can be found with the following expression:

$$\sigma = \begin{cases} K\delta & 0 \le \delta \le \delta_0 \\ (1 - D_s)\sigma_0 \left(\dfrac{\delta_c - \delta_0}{\delta_c - \delta} \right) & \delta_0 < \delta < \delta_c \\ 0 & \delta \ge \delta_c \end{cases} \tag{6.48}$$

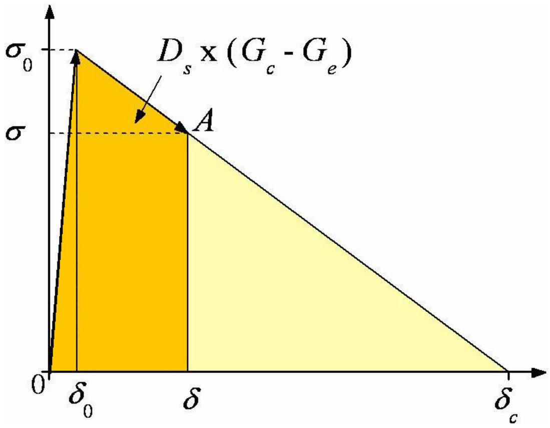

Figure 6.8 - Damage formulation based on the work done

Work done based damage for the third-order polynomial interface law

The third-order polynomial law can be written in terms of damage, with the work done formulation, by considering the work done per unit area necessary to separate an interface by δ as the area under the δ-σ curve up to that displacement.

The damage parameter can therefore be defined as ratio between the two following areas:

- The area under the curve of the constitutive law until a generic displacement δ.
- The total area under the curve, that is G_c.

The expression of the static damage with this formulation is the following:

$$D_s = \begin{cases} \left(\dfrac{4 \cdot \delta_c - 3 \cdot \delta}{\delta_c} \right) \cdot \left(\dfrac{\delta}{\delta_c} \right)^3 & 0 \le \delta < \delta_c \\ 1 & \delta \ge \delta_c \end{cases} \tag{6.49}$$

The equations 6.21 and 6.22, in terms of damage, can be written in the following way:

$$\sigma = \begin{cases} (1 - D_s) \cdot K \cdot \delta \cdot \left(1 - \dfrac{\delta}{\delta_c} \right)^2 \cdot \dfrac{1}{\left[2 - 2 \cdot \dfrac{\delta}{\delta_c} - 5 \cdot \left(\dfrac{\delta}{\delta_c} \right)^2 + 8 \cdot \left(\dfrac{\delta}{\delta_c} \right)^3 - 3 \cdot \left(\dfrac{\delta}{\delta_c} \right)^4 \right]} & 0 \le \delta < \delta_c \\ 0 & \delta \ge \delta_c \end{cases} \tag{6.50}$$

Work done based damage for the linear-polynomial mixed interface law

The linear-polynomial mixed law can be written in terms of damage, with the work done formulation, by considering the work done per unit area necessary to separate an interface by δ as the area under the δ-σ curve up to that displacement.

The damage parameter can therefore be defined as ratio between the two following areas:

- The area under the curve of the constitutive law until a generic displacement δ, without the area under the elastic branch, corresponding to a displacement δ_0.
- The total area under the curve, that is G_c, without the area under the elastic branch, corresponding to a displacement δ_0.

The expression of the static damage with this formulation is the following:

$$D_s = \begin{cases} 0 & 0 \le \delta \le \delta_0 \\ \dfrac{1}{(\delta_c - \delta_0)^4} \cdot \left[\delta^4 - 2 \cdot (\delta_0 + \delta_c) \cdot \delta^3 + 6 \cdot (\delta_0 \cdot \delta_c) \cdot \delta^2 + 2 \cdot (\delta_c^3 - 3 \cdot \delta_0 \cdot \delta_c^2) \cdot \delta + \right. & \\ \qquad \left. + \delta_0^4 - 4 \cdot \delta_0^3 \cdot \delta_c - 2 \cdot \delta_0 \cdot \delta_c^3 + 6 \cdot \delta_0^2 \cdot \delta_c^2 \right] & \delta_0 < \delta < \delta_c \\ 1 & \delta \ge \delta_c \end{cases}$$

(6.51)

6.2.6 Implementation

In this section the implementation of the simplified model described in the previous sections is presented. Before introducing the formulation of the fatigue damage in the model, it has been necessary to analyze the response of the model under static loading only, in order to evaluate its reliability.

The programming language chosen for this implementation is Matlab, which has been chosen for its simplicity and in order to have a comparison and a different point of view from a previous implementation [LGR07], already made in FORTRAN.

The response of the static model has been evaluated both under displacement (rotation) control and under force (moment) control. The moment control, that means that a moment has been applied to the cylinder, is the modality that has been carried on also for the fatigue loading, whereas the rotation control modality has been applied only to the static loaded model.

The rotation control modality permit to analyze the behaviour of the model for rotations bigger than the critical angle, as it has been defined by equation 6.7, and the value of the reacting moment can be calculated directly from the imposed rotation without the necessity of any iterative process.

In figure 6.9 the flowchart related to the implementation of the static loaded model under moment control is shown.

The implementation of the model under rotation control is basically the same. The only difference is that in the rotation control model the bisection method is not needed, because from a particular value of the angle it is possible to evaluate directly the relevant value of the moment.

In the first column from the left of the flowchart, the first block is the one in which the geometric characteristics of the model and the other input data, as they will be described later in this section, have to be inserted.

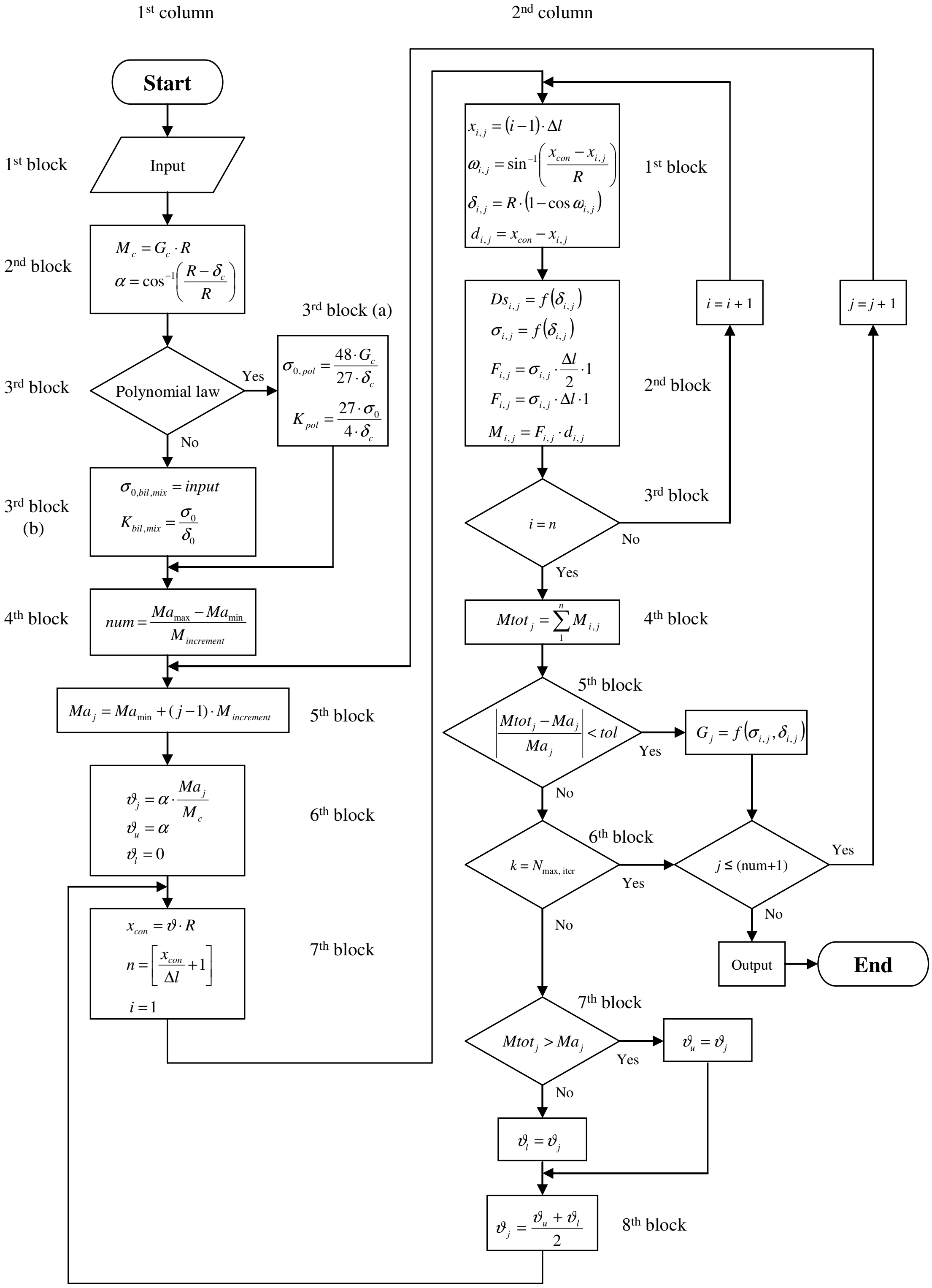

Figure 6.9 – Flowchart of the static damage model implementation under moment control

In the second block the value of the critical moment (M_c) and the value of the relevant critical angle (α) for the model are calculated.

In the third block there is a check to ensure that the values of σ_0 and K are the right values for the chosen constitutive law. The reason for this it will be better explained in section 6.2.7.

After the choice of the constitutive law, in the flowchart there is the fourth block, in which the total number (*num*) of the increments of the moment is calculated. In fact it is possible to assign a minimum (Ma_{min}) and a maximum (Ma_{max}) value of the applied moment and to reach the maximum value of the moment trough a certain number of increments with the value of $M_{increment}$. In this work the value of Ma_{min} will be always put equal to zero, and the maximum value of the applied moment will be simply called M_a.

In the fifth block the value of the moment (Ma_j) for the actual increment j is calculated.

With the sixth block starts the procedure to evaluate the resultant moment ($Mtot_j$) due to the j-th increment of the moment. In this sixth block the initial parameters required for the bisection method are imposed.

In the seventh block, the position of the contact point (x_{con}) of the cylinder, that is the tip of the crack, and the number of springs before that point is computed.

In the second column, in the first block, the kinematical characteristics of the i-th spring are computed, whereas in the second block the stress, the force, and the relevant moment in the i-th spring are calculated.

In the third block there is another check, which is a comparison between the index i of the number of the springs and the total number n of springs before the contact point. If the value of the index i is smaller than the number of springs, the index is increased of one and the program goes back to the beginning of the second column.

If the moment in all the active springs has been computed, in the fourth block the sum of all the contribution to the moment due to the *i*-th spring is calculated.

If this sum satisfies the condition in the fifth block, then it is possible to calculate the value of the energy release (G_j) for the *j*-th increment, to go to the next *j*-th increment of the moment and then to repeat the procedure from the fifth block of the first column. When the last increment is reached, the program gives the outputs and stops.

If instead the condition in the fifth block is not satisfied, in the sixth block there is a check that ensure that if the previous condition it is not verified by the maximum chosen number of iterations, the program go to the next increment or stops (if the actual increment is the last).

Until the maximum number of iteration is reached, if the computed moment $Mtot_j$ is bigger than the actual applied moment Ma_j, as checked the seventh block, the upper bisection limit (θ_u) is put equal to the actual angle (θ_j), otherwise the lower bisection limit (θ_l) is put equal to the actual angle.

In the eighth block of the column, the new value for the actual angle is assigned, and the program goes back to the seventh block of the first column to start a new iteration.

6.2.7 Analysis of the model and validation

An analysis was made in order to evaluate the response of the model and its correspondence with the implementation of this model already done [LGR07].

Both the implementation of the model under rotation control and the model under moment control were evaluated.

Regarding to the model under rotation control, for each of the constitutive law and the damage formulation described in the sections 6.2.4 and 6.2.5, was evaluated the behaviour of the following output parameters.

Firstly, the behaviour of the ratio between the applied moment and the critical moment (M_a/M_c) versus the ratio between the applied angle and the critical angle (θ/α) was evaluated. The applied moment, in the case of rotation control, is computed as the sum of the moment in each spring due to the applied rotation.

Secondly, for only one spring, precisely the first, but it would be the same for each spring that has done completely damaged, the following things were evaluated:

- The ratio between the actual stress and the critical stress (σ/σ_0) versus the ratio between the actual displacement and the critical displacement (δ/δ_c).
- The ratio between the actual energy release rate and the critical value of the energy release rate (G/G_c) versus the ratio between the actual displacement and the critical displacement (δ/δ_c).
- The behaviour of the damage parameter (D_s) versus the ratio between the actual displacement and the critical displacement (δ/δ_c).

All the above quantities were computed for an applied rotation angle variable from zero to two times the value of the critical angle (α), as defined by equation 6.7. In fact, the advantage of the rotation control model, other than a bigger simplicity in evaluating the resultant moment, is the possibility to evaluate the behaviour of the model for values of the moment bigger than the critical value.

At least, a parametric analysis was made to evaluate the behaviour of the model with respect do the distance between the springs (Δl).

Regarding the moment control model, for each of the above constitutive law and for each damage criterion, were evaluated the same quantities studied for the rotation control model. It was applied a moment M_a equal to the 99.6 % of the critical value M_c.

In fact, under moment control, when the value of the applied moment is close to the value of the critical moment, the model needs more iteration to reach the convergence and in correspondence of the critical value of the moment the model is not able to converge.

For this model the parametric analysis respect to Δl has not been carried on.

Before showing the obtained results, it is necessary to explain which value was used as data input. The following data are the same for the both the models under rotation and under moment control.

The geometric characteristic of the model are the following:

- Radius of the cylinder (R): 100 mm
- Distance between springs (Δl): 0.01 mm
- Model width (w): 1 mm

The parameters of the constitutive laws are now discussed.

The critical value of the energy release rate (G_c) is assumed the same for all the constitutive laws, with the value of 0.260 N/mm.

The elastic limit δ_0 value has been assumed equal to 1 x 10^{-6} mm.

The maximum value of the stress (σ_0) has been assumed the same for the bilinear and for the mixed law: 30 MPa.

The critical value of the relative displacement (δ_c), remembering the equations 6.20 and 6.33, has been evaluated as following for the bilinear law and for the mixed law:

$$\delta_c = \frac{2 \cdot G_c}{\sigma_0} \tag{6.52}$$

In this case σ_0 is the value related to the bilinear and mixed law.

However the value of δ_c evaluated by the equation 6.52 has been assumed valid also for the third-order polynomial law.

The reason for this is that, as it has been explained in the paragraph 6.2.4, each constitutive law is characterized by some parameters. For the bilinear and mixed law, these parameters are the elastic limit (σ_0), the relative displacement related to the elastic limit (δ_0), the critical value of the relative displacement (δ_c) and, at least, the critical value of the release energy rate (G_c) evaluated as the area under the constitutive curve.

For the polynomial law the parameter are only σ_0, δ_c, and the critical value of the release energy rate (G_c) this last evaluated always as the area under the constitutive curve.

The above parameters are not all independent, but they are related each other by the constitutive law.

The problem, in using different constitutive laws, is that there is not the same correspondence between the parameters. For example, for a particular value of G_c and δ_c in the bilinear law there is a value of σ_0, but in the polynomial law, for the same value of G_c and δ_c, there will be a different value of σ_0.

In order to ensure that the model has the most similar characteristic in using the three different laws, the choice to assign the same value at the parameters that are most important for the model was made.

It is now necessary to remember that the critical moment of the model (M_c) is related to the release energy rate (G_c) by equation 6.12 and that the critical angle (α), instead, is related to the critical value of the relative displacement (δ_c) by equation 6.7.

In order to let the model have the same values of M_c and α, to all the three constitutive laws the same values of G_c and δ_c have been assigned. Therefore σ_0 has the same value for the bilinear and mixed law, but a quite smaller value for the polynomial law.

This choice it will be carried for all this work.

The maximum value of the stress for the polynomial law (σ_0), evaluated remembering the equation 6.26, is the following:

$$\sigma_0 = \frac{4}{27} \cdot \frac{G_c}{\delta_c} \tag{6.53}$$

Only for the model under moment control two parameters have to be added. They are the maximum number of iterations for the bisection method, which has been assumed equal to 100, and the convergence tolerance (*tol*), assumed equal to 1e-8.

If the program does not reach the convergence by 100 iterations, it stops.

In the moment control model, in which, because of its characteristics, the critical moment (M_c), evaluated by equation 6.12, is 26 N·mm, a maximum moment of 25.9 N·mm was applied, with increments of 0.1 N·mm.

In the next subparagraph the results obtained for each model and for each law will be shown.

Analysis of the model under rotation control

The first analysis done on the cylinder model under rotation control, as said in the previous subparagraph, has been carried on about the behaviour of the ratio between the resultant moment and the critical moment (M_a/M_c) versus the ratio between the applied angle and the critical angle (θ/α). As shown in figure 6.10, this analysis was made for all the three constitutive laws. The graphs in figures 6.10, 6.11 and 6.12 are independent on the damage formulation, because whatever is the expression of the damage parameter, the expression of the constitutive law globally does not change.

The applied rotation is two times the critical angle, and it is possible to see that after the value of $\theta/\alpha = 1$ the value of M_a/M_c remains constant, because, for applied rotations bigger than the critical angle, some springs start to be broken, do not giving any more contribution, and the number of the reacting springs remains constant.

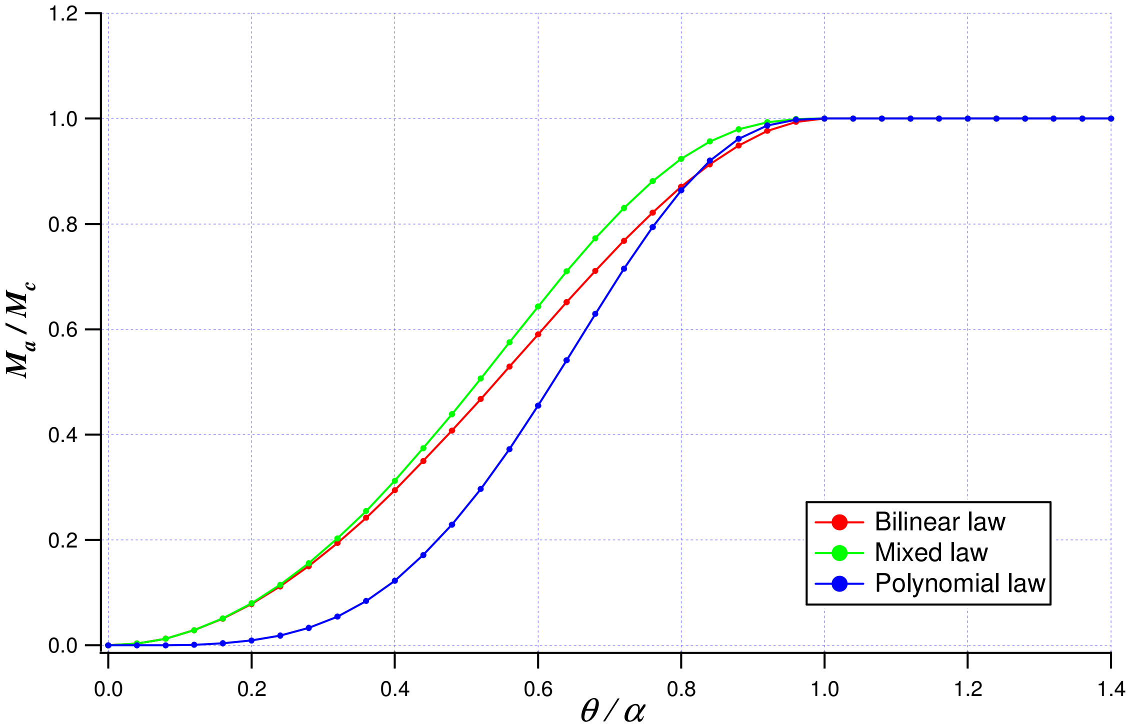

Figure 6.10 – Behaviour of M_a vs. θ for the three constitutive laws

It is possible to see that the bilinear and the mixed law have a very similar behaviour for little relative displacements, because of their equal elastic branches, whereas the polynomial law, in which the damage starts from the beginning of the curve, gives smaller moments for the same rotations.

In figure 6.11 it is possible to see the behaviour of the stress versus the relative displacement of a spring. This curve is related to the first spring of the model (with $x = 0$), but this is the behaviour of a typical spring of the model. Each of the curves in the graph has the same shape of the relevant constitutive law.

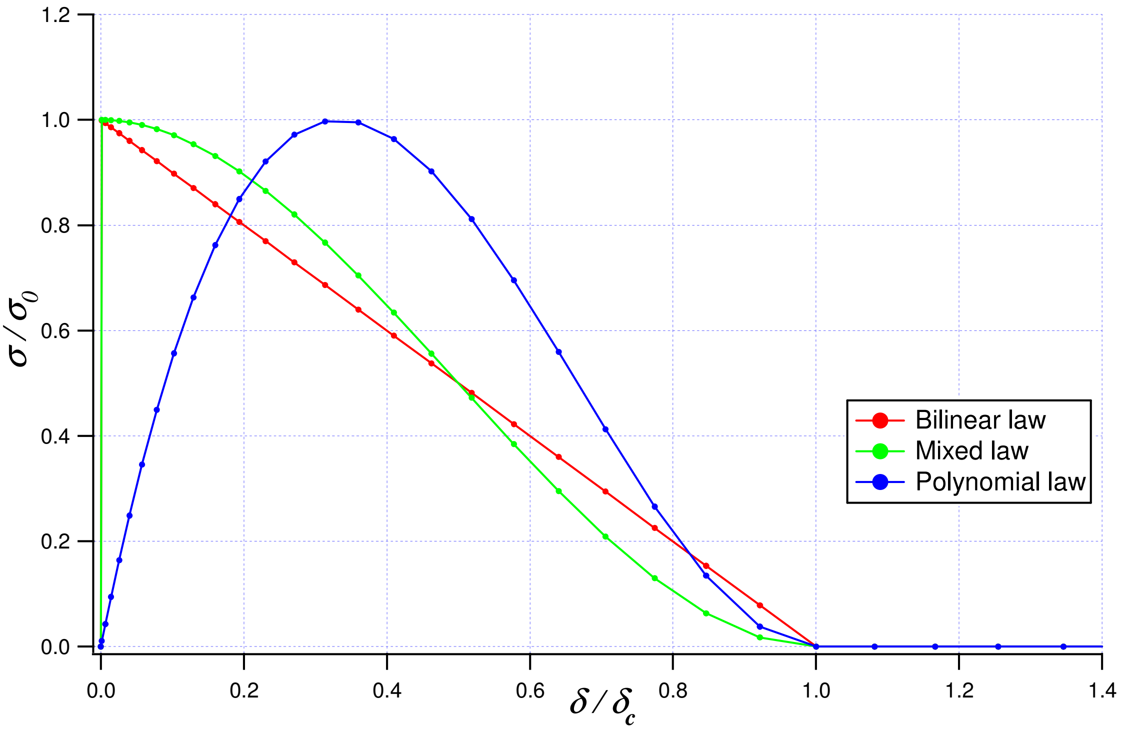

Figure 6.11 – Behaviour of σ vs. δ for a typical spring with the three constitutive laws

The figure 6.12 shows the behaviour of the energy release (G) rate versus the relative displacement in a typical spring (the first, also in this case). Remembering that the release energy rate for a particular displacement is the area under the curve by that displacement, it is simple to understand that the value of G increases more quickly with the displacement in the linear and mixed law, rather than in the polynomial, because the area under the curve of the two first laws increases more quickly than the polynomial.

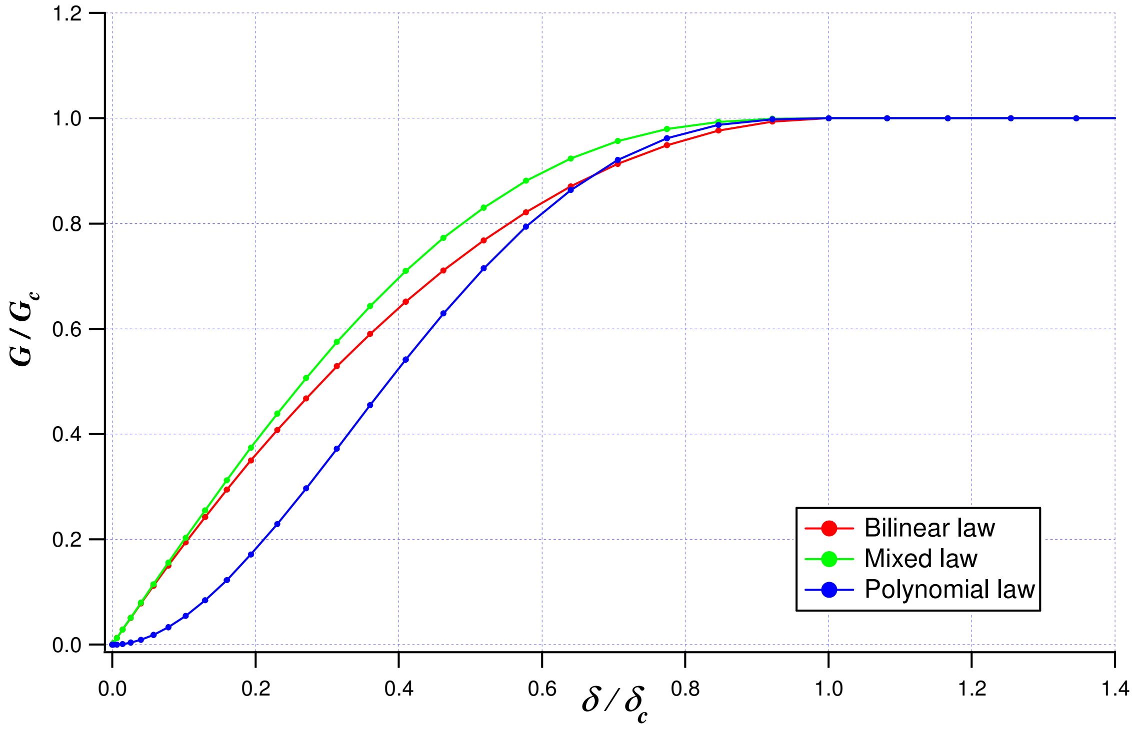

Figure 6.12 – Behaviour of *G* vs. *δ* for a typical spring with the three constitutive laws

The other important thing that has been studied in the model is the variation of the static damage parameter versus the relative displacement. Figure 6.13 shows the growth of damage with an increasing value of the relative displacement using the three damage formulation for the bilinear interface constitutive laws. It can be appreciated that, for the stiffness degradation based damage, with only a small increment in δ over δ_0 the value of the static damage increases extremely fast. This is a consequence of the way in which the static damage has been defined and of the adopted parameter values. With the two other formulations the damage parameter increases more slowly with the relative displacement.

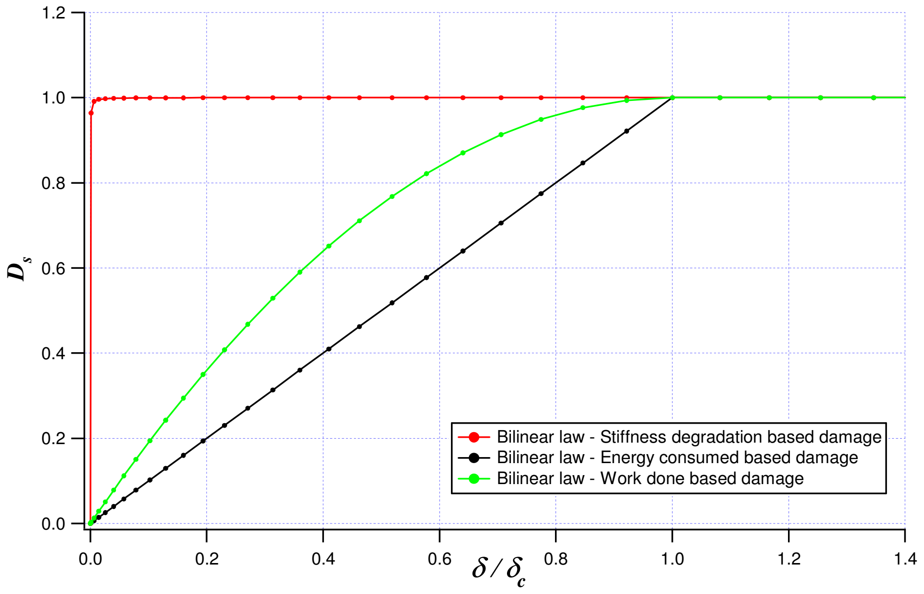

Figure 6.13 – Behaviour of D_s vs. δ for a typical spring (bilinear law with three damage formulations)

Applying the three formulations of the static damage to the linear-polynomial mixed law, with the stiffness degradation based damage the behaviour of the damage parameter is basically the same of the bilinear law, as figure 6.14 shows. With the two other formulations, instead, the value of the damage parameter increase a little more quickly than in the bilinear law.

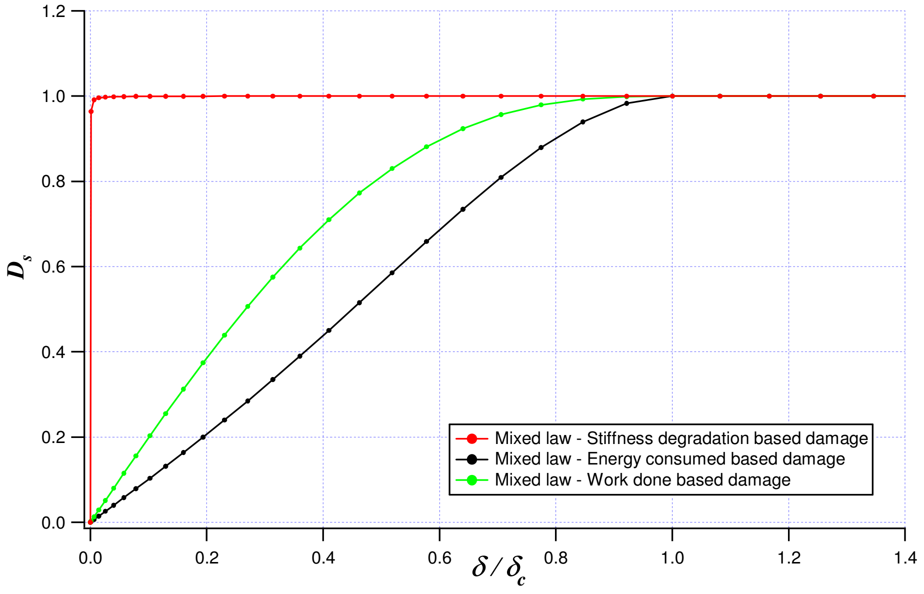

Figure 6.14– Behaviour of D_s vs. δ for a typical spring (mixed law with three damage formulations)

The polynomial law changes a lot the behaviour of the damage parameter, as figure 6.15 shows. With all the three damage formulations the damage parameter increases more slowly then the other constitutive laws.

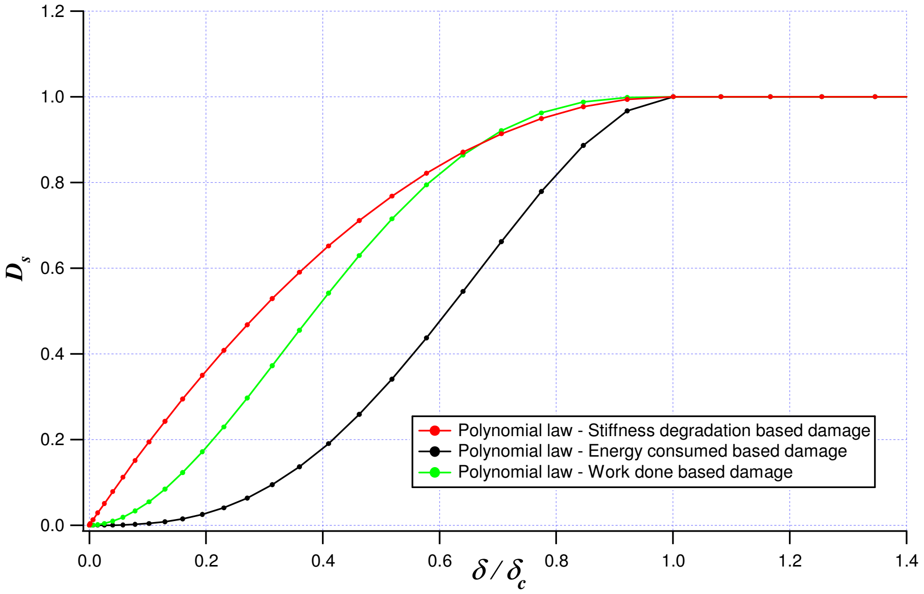

Figure 6.15– Behaviour of D_s vs δ for a typical spring (polynomial law with three damage formulations)

In order to evaluate the behaviour of the model with respect to the influence of the distance between the springs (Δl), a parametrical analysis was conducted.

For the analysis was chosen the model under rotation control, with the bilinear law and the stiffness degradation based damage.

All the data input are the same for all the analysis and only Δl varies from a value of 0.01 mm, which is the value used for all the previous analysis, and 0.9 mm, that it is a quite big value for the geometry of this problem.

In the figure 6.16 the behaviour of the model with respect to Δl is shown.

It is possible to observe that, when Δl become bigger, some oscillations appears in the graph of the ratio between the resultant moment and the critical moment (M_d/M_c) versus the ratio between the applied angle and the critical angle (θ/α).

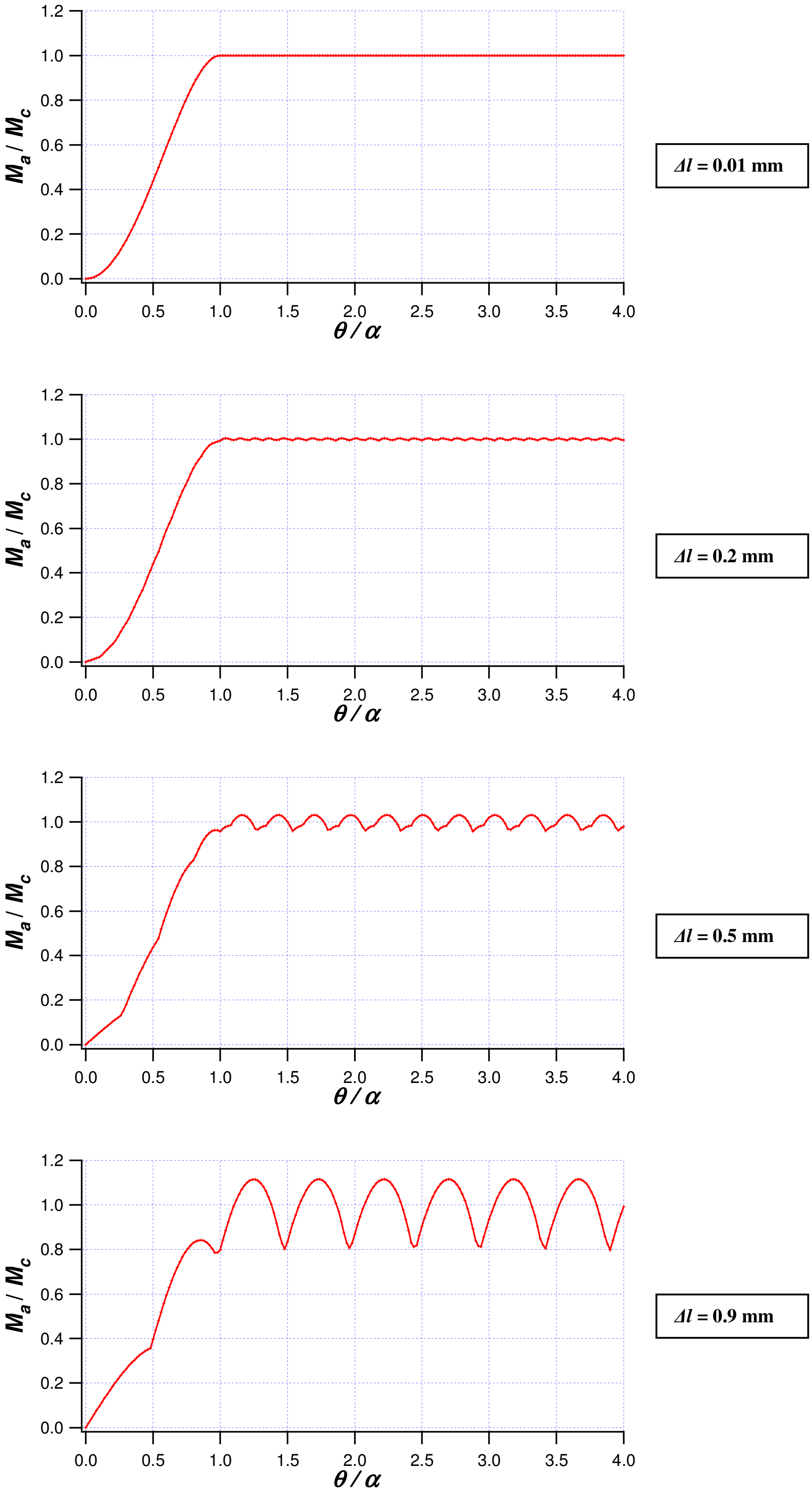

Figure 6.16 – Parametric analysis for *Δl* (bilinear law, stiffness degradation and rotation control)

These oscillations are due to the fact that, when the distance between the springs grows up, the number of the spring decreases. If there are few active springs close to the contact zone, when a spring is active the next spring is in a too different situation of stress to give a contribution to the total moment without an abrupt variations of the total result moments.

The phenomenon is more evident when Δl is bigger. For $\Delta l = 0.9$ mm, for example, there is only one active spring before the value of $\theta/\alpha = 0.5$. At this point the contribution of the second spring is done, with an abrupt variation of the curve.

This analysis has let know that the value of Δl adopted for the model is a good value.

Analysis of the model under moment control

Under moment control the same analysis of the model under rotation control has been done, with the only difference that it is not possible to reach a moment equal to or bigger than the critical moment.

In this subparagraph only few graphs are presented, that are comparable with the ones already obtained for the same model [L08].

In figure 6.17 the behaviour of the applied moment versus the angle is shown for all the three constitutive laws. Also in this case the graph is independent on the formulation of the damage, as said in the previous subparagraph.

The graph is alike to the one obtained under rotation control, and the curve related to the bilinear law looks very close to the one presented in figure 6.18, that is the curve obtained in reference [L08] for the same bilinear law with all the same input data.

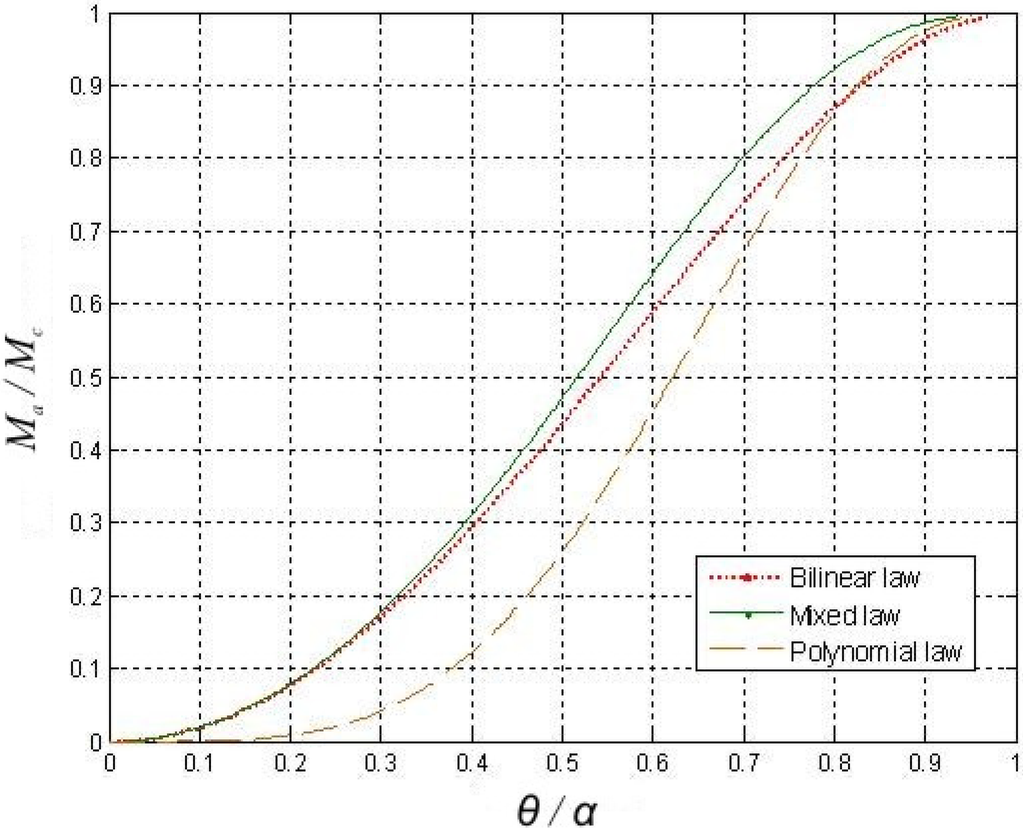

Figure 6.17 – Comparison of the behaviour of M_a vs. θ for three constitutive laws (moment control)

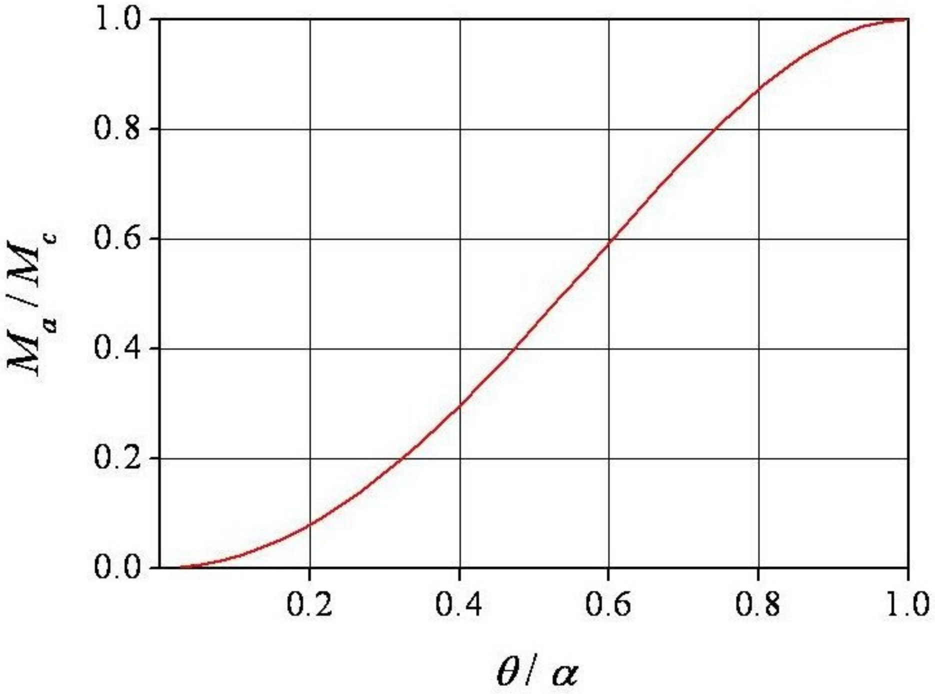

Figure 6.18 – Behaviour of M_a vs. θ shown in reference [L08]

The last graph proposed, shown in figure 6.19, represents the behaviour of the energy release versus the relative displacement.

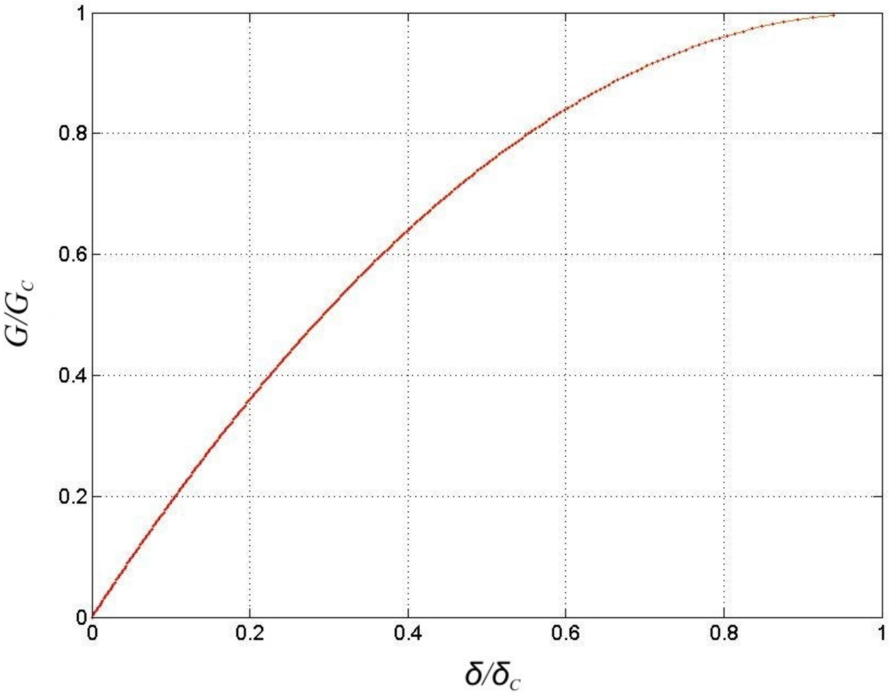

Figure 6.19 – Behaviour of *G* vs. *δ* for the bilinear law

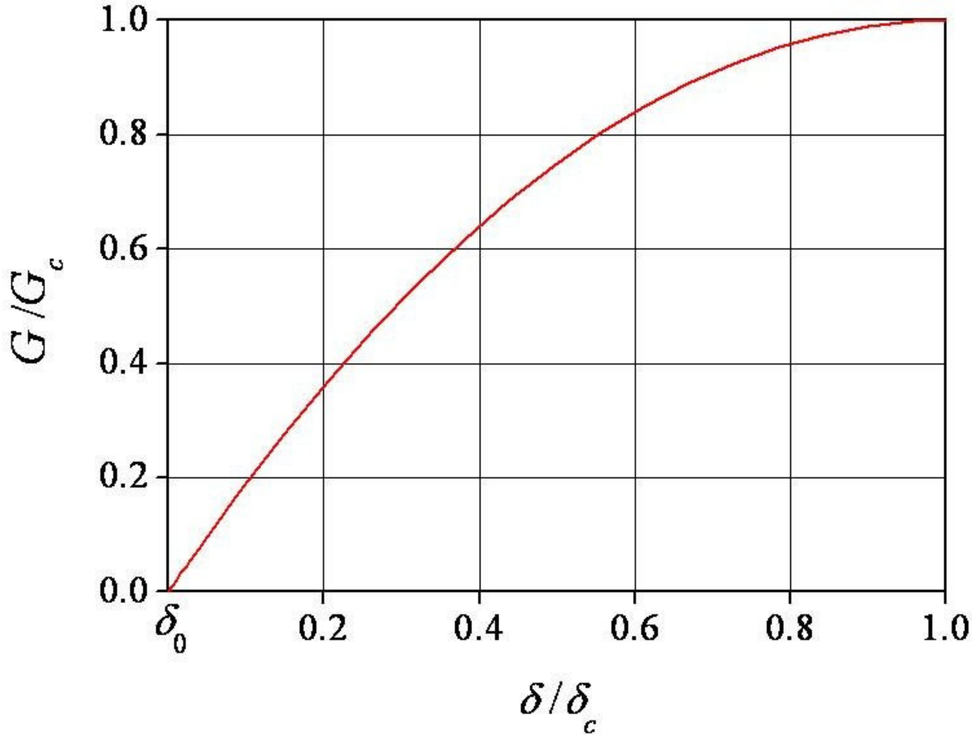

Figure 6.20 – Behaviour of G vs. δ for the bilinear law shown in reference [L08].

The curve is similar to the one shown in figure 6.12 for the bilinear law, but obtained under moment control, and it is now compared with the one obtained in reference [L08], shown in figure 6.20, for the same model with all the same input data. It is possible to see that the curves look very close to each other.

In conclusion, it is possible to see that the response of the model is highly dependent on the constitutive law adopted.

The bilinear and the mixed law show an equal behaviour for little values of the applied moment. In this situation, in fact, all the springs are yet in the linear-elastic stage of the curve.

When the damage begins, the bilinear law gives, for the same rotation, a higher reacting moment. This behaviour was expected, because the mixed law contains a bigger area (more energy to win in order to let the crack propagate).

The polynomial law has instead a very different behaviour from the others, due to the fact that there is not an elastic stage, but the damage starts from the beginning of the constitutive curve.

Anyway, regarding to the implementation of the static, the model has done results coherent each other and a good correspondence, as possible, with the previous implementation [L08].

In the next sections the implementation of the strategy for the study of the fatigue will be described.

6.3 Simplified model for delamination under fatigue loading

The simple cylinder model described in the previous paragraphs was developed to enable rapid assessment of fatigue degradation strategies for interface elements. In the following paragraphs the degradation strategy which has been implemented using the cylinder model is described. It is possible to find more details of this strategy in references [RGTBV05, PBDG00], in which the stiffness degradation definition is adopted for the damage *D* using a simple bilinear interface element in a finite element model.

In this work the fatigue degradation strategy is extended to include the following interface element constitutive laws, described in the paragraphs 6.2.4 and 6.2.5:

- Bilinear constitutive laws, with all the three definition of damage *D*.
- Third-order polynomial constitutive laws with the stiffness degradation definition of damage *D* only.

6.3.1 Basic assumptions for the numerical simulation

Some assumptions were made in order to simplify the calculation process [PBDG00]. The first one is related to the cyclic load which is assumed to be sinusoidal and oscillating between zero and a maximum value. It would be very computationally expensive to simulate the relative displacement history for each pair of nodes along the interface, and so for constant amplitude loading the load numerically applied to the structure (the cylinder model, in this thesis) is taken as constant and equal to the maximum value of the actual cyclic load, as shown in figure 6.21.

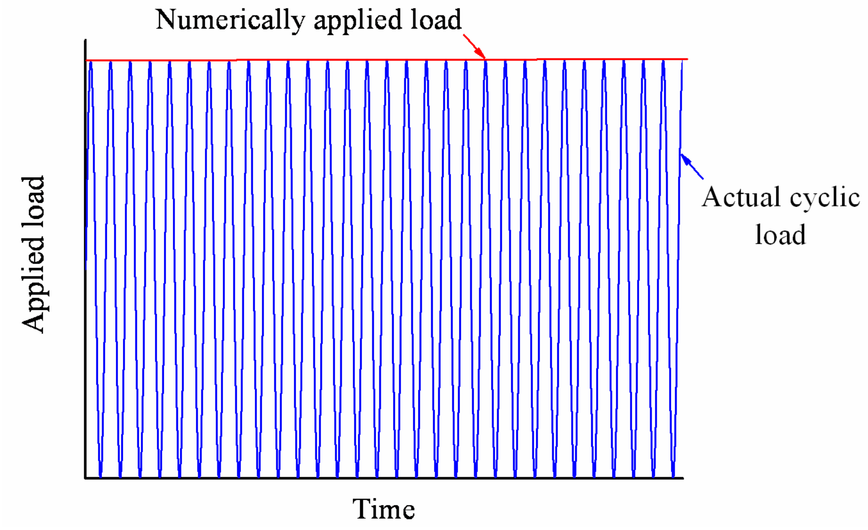

Figure 6.21 - Envelope of the assumed cyclic load for a large number of cycles

Consequently, the relative displacement calculated at the interface will be the envelope of its true cyclic variation with time, as seen in figure 6.22.

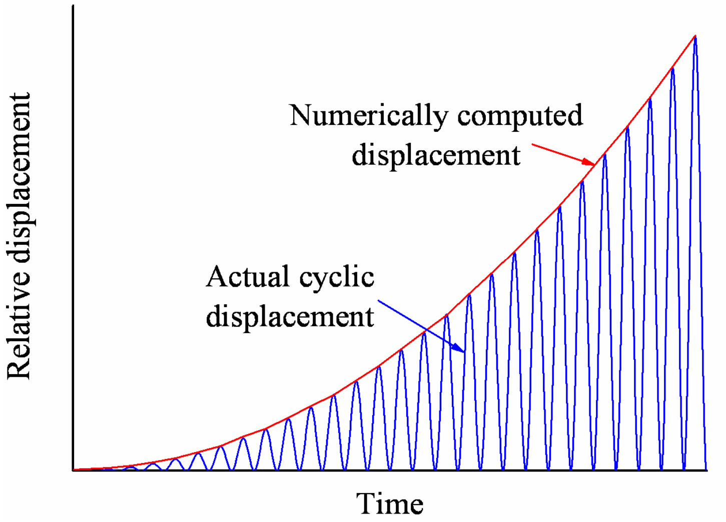

Figure 6.22- Actual cyclic displacement and its envelope curve

6.3.2 Rate of change of the damage variable

The introduction of the study of fatigue in the cylinder model requires combining the relative displacement/stress relationship described in the previous sections with a fatigue model.

It is possible to do this by splitting the rate of total damage ($\dot{D}$) into the sum of the static ($\dot{D}_s$) and fatigue ($\dot{D}_f$) components, as following:

$$\dot{D} = \dot{D}_s + \dot{D}_f \tag{6.54}$$

The static component will be defined in section 6.3.3 and the fatigue component in section 6.3.4.

The existence and distinction between these components of the rate of total damage can be seen in figure 6.23 which shows three displacement 'loads' applied to a single interface spring during a time interval $t_1 \leq t \leq t_2$.

For a monotonically increasing displacement, shown in figure 6.23(a), there is no fatigue damage and so the rate of damage only has a static component.

For a cyclic applied displacement with constant amplitude, shown in figure 6.23(b), in the interval $t_1 \leq t \leq t_2$ the $\dot{D}_s$ is zero and there is only a fatigue component $\dot{D}_f$ (of course at some time prior to t_1 the initial application of the displacement loading will have induced a static rate component).

Finally if the spring is subjected to an oscillating displacement of increasing amplitude, as shown in figure 6.23(c), then the total damage rate will now include static and fatigue components.

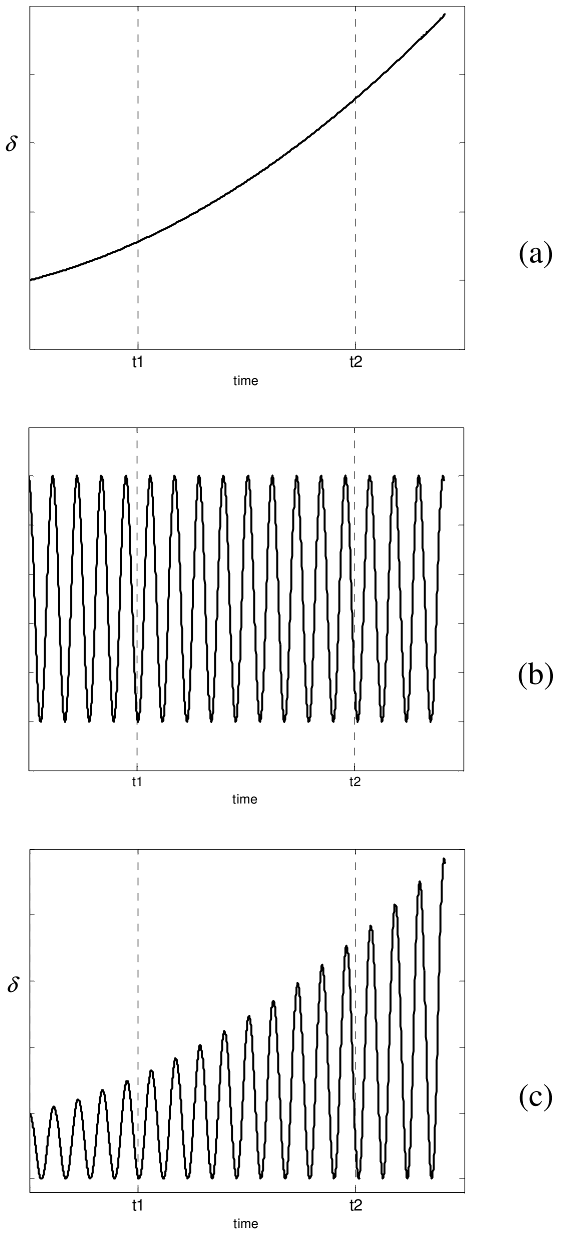

Figure 6.23 - (a) monotonic increasing displacement characterised by $\dot{D}_S \neq 0$, $\dot{D}_f = 0$; (b) cyclic displacement characterised by $\dot{D}_S = 0$, $\dot{D}_f \neq 0$; (c) displacement characterised by $\dot{D}_S \neq 0$, $\dot{D}_f \neq 0$

6.3.3 Rate of change of the static damage

This section describes how to consider the static damage during the fatigue loading. Considering the stiffness degradation damage with the bilinear interface constitutive law, the equation 6.37 can be differentiated with respect to time in order to obtain the rate of static damage

$$\frac{\partial D_s}{\partial t} = \dot{D}_s = \frac{\delta_0 \delta_c}{\delta_c - \delta_0} \frac{\dot{\delta}}{\delta^2} \qquad \delta_0 < \delta < \delta_c \tag{6.55}$$

A cycle based formulation can be obtained from equation 6.55 by integrating over a number of loading cycles (ΔN), giving the following expression:

$$D_s(N + \Delta N) - D_s(N) = \frac{\delta_0 \delta_c}{\delta_c - \delta_0} \left(\frac{1}{\delta(N)} - \frac{1}{\delta(N + \Delta N)} \right) \tag{6.56}$$

where $\delta(N)$ is the value of the amplitude of the displacement at N cycles and $\delta(N+\Delta N)$ is the value at $N+\Delta N$ cycles.

The relative displacement $\delta(N+\Delta N) \geq \delta(N)$ is considered to be monotonically increasing. In a similar way $D_s(N)$ and $D_s(N+\Delta N)$ are the values of the static damage after N or $N+\Delta N$ cycles respectively.

Equation 6.56 could have been obtained in a simpler way by expressing $D_s(N+\Delta N)$ and $D_s(N)$ with equation 6.37 and by computing the difference of the two expressions.

The procedure adopted here shows the dependence of the static damage on the number of cycles rather than simply on the displacement amplitude.

Adopting the stiffness degradation damage with the polynomial interface constitutive law, equation 6.38 can be used to obtain an expression for the damage increment due to an increment of the number of loading cycles (*ΔN*), as following:

$$D_s(N+\Delta N)-D_s(N)=\frac{\delta(N+\Delta N)-\delta(N)}{\delta_c}\left(2-\frac{\delta(N+\Delta N)+\delta(N)}{\delta_c}\right) \tag{6.57}$$

Adopting, instead, the energy-consumed damage with the bilinear interface constitutive law, an increment of damage can be easily computed from the equation 6.40:

$$D_s(N+\Delta N)-D_s(N)=\frac{\delta(N+\Delta N)-\delta(N)}{\delta_c-\delta_0} \tag{6.58}$$

If finally the work-done damage is adopted with the bilinear interface constitutive law, then equation 6.47 can be used to derive the damage increment due to an increment of the number of loading cycles (*ΔN*):

$$D_s(N+\Delta N)-D_s(N)=\frac{\left(\delta(N)-\delta(N+\Delta N)\right)\left(\delta(N)+\delta(N+\Delta N)-2\delta_c\right)}{(\delta_c-\delta_0)^2} \tag{6.59}$$

6.3.4 Rate of change of the fatigue damage

The expression for the fatigue damage rate was assumed, as it is possible to see in reference [RGTBV05], to have the following form:

$$\dot{D}_f = \frac{\partial D_f}{\partial t} = Ce^{\lambda D}\left(\frac{\delta}{\delta_a}\right)^{\beta} \tag{6.60}$$

where C, λ and β are parameters which can be evaluated by comparison with interlaminar fatigue data and δ_a is a displacement-like quantity introduced for dimensional reasons. This was based on a formulation proposed in reference [PBDG00] for fatigue damage of continua.

Following reference [RGTBV05] it is possible to obtain an expression for the increment of the damage due to fatigue over a number of cycles ΔN:

$$D_f(N+\Delta N) - D_f(N) = \Delta N \frac{C}{1+\beta} e^{\lambda D_\mu}\left(\frac{\delta_\mu}{\delta_c}\right)^{1+\beta} \tag{6.61}$$

In the equation 6.61 δ_a has been chosen equal to the failure displacement δ_c, and D_μ and δ_μ are defined according to reference [RGTBV05] as:

$$\begin{aligned} D_\mu &= (1-\mu)D(N) + \mu D(N+\Delta N) \\ \delta_\mu &= (1-\mu)\delta(N) + \mu\delta(N+\Delta N) \end{aligned} \tag{6.62}$$

The value of the parameter μ has been chosen as 0.7.

At this point it is possible to obtain the increment of total damage due to an increment ΔN of the number of cycles by combining equations 6.54, 6.56, which are related to the case of bilinear constitutive law and stiffness degradation damage, and equation 6.61. The resultant expression is the following:

$$D(N+\varDelta N)-D(N)=\underbrace{\frac{\delta_0\delta_c}{\delta_c-\delta_0}\left(\frac{1}{\delta(N)}-\frac{1}{\delta(N+\varDelta N)}\right)}_{static}+\underbrace{\varDelta N\frac{C}{1+\beta}e^{\lambda D_\mu}\left(\frac{\delta_\mu}{\delta_c}\right)^{1+\beta}}_{fatigue} \tag{6.63}$$

Equation 6.63 defines implicitly the value of D after $N+\varDelta N$ cycles since D appears on both sides of the equation. The value of the damage can be found by solving the following nonlinear algebraic equation:

$$D(N+\varDelta N)-D(N)-\frac{\delta_0\delta_c}{\delta_c-\delta_0}\left(\frac{1}{\delta(N)}-\frac{1}{\delta(N+\varDelta N)}\right)-\varDelta N\frac{C}{1+\beta}e^{\lambda D_\mu}\left(\frac{\delta_\mu}{\delta_c}\right)^{1+\beta}=0 \tag{6.64}$$

The previous equation 6.64 is valid only for the case of bilinear constitutive law with stiffness degradation based static damage definition, because equation 6.56 was used to obtain the static component of the damage in equation 6.63.

The static component of damage increment should be substituted by the expressions 6.57 or 6.58 or 6.59 in order to make the expression valid for the relevant formulation of the damage. The stress in a damaged interface will be computed in general with equations 6.36 or 6.41 or 6.48, depending on the adopted static damage definition, where the total damage D is used rather than D_s.

For all the static damage formulations the value of the damage variable is zero if $\delta < \delta_0$. However the application of Peerlings fatigue degradation strategy allows the degradation of the interface even for $\delta < \delta_0$.

Therefore there is a problem about how to define the stress when $\delta < \delta_0$ and only fatigue damage has taken place, since equations 6.41 and 6.48 would provide meaningless values if used in such a range. It was then decided to use equation 6.36 also for the energy-consumed and work-done static damage formulations in the range $\delta < \delta_0$. A clear advantage of such a choice is that at the transition for $\delta = \delta_0$ it provides a continuous, even if not smooth, stress variation.

6.3.5 Implementation

The cylinder model presented in this chapter, with one of the constitutive law, a damage formulation and the fatigue strategy already described in the past sections can be implemented in a computer code in order to compute the crack length x_{con} generated by a cyclic moment of amplitude M_a ($<M_c$) applied for a certain number of cycles N_{tot}.

An incremental approach is adopted in which an important parameter is ΔN, the number of cycles for a load step. All the relevant parameter values are assumed to be known at the beginning of the load step corresponding to the total number of cycles N, applied in the previous load steps, where $N < N_{tot}$. At the beginning of the computation, the total number of cycle is $N = 0$.

The parameters necessary for the model are the followings:

- $\theta(N)$: rotation of the cylinder.
- n_o: number of springs with an extension bigger than zero.
- $\delta_i(N)$, i=1, … n_o, extension for every spring with nonzero extension.
- $D_i(N)$, i=1, … n_o, damage value for every spring with a non-zero extension (in general some of the springs will have D_i=1 and therefore σ_i=0).

At this point the computer program related to the implementation of the fatigue in the cylinder model is described. This program takes its input data from the computer program explained in the paragraph 6.2.6, that is related to the quasi-static application of the load.

The computer program for the fatigue implementation makes some steps for each increment ΔN of the number of cycles, until the imposed total number of cycles is reached.

The steps for an increment ΔN are the followings:

- The number of cycles is increased by the increment ΔN.
- The corresponding increment of rotation $\Delta\theta$ is guessed.
- The new value of the rotation ($\theta(N+\Delta N)=\theta(N)+\Delta\theta$) is used to evaluate the new number of springs (n_n) which have an extension greater than zero and the corresponding extensions $\delta_i(N+\Delta N)$ with $i=1, \ldots n_n$, are calculated.
- Equation 6.64 is solved, for every active spring with $0<D<1$, to find the new values of all damage variables $D_i(N+\Delta N)$, $i=1, \ldots n_n$. When equation 6.64 is solved the only unknown is $D_i(N+\Delta N)$, whereas all other variables are given.
- $D_i(N+\Delta N)$ and $\delta_i(N+\Delta N)$ are used in the constitutive equations (6.36 or 6.41 or 6.48, in which the total damage is used if $\delta>\delta_0$, whereas if $\delta<\delta_0$ equation 6.36 is used as explained at the end of paragraph 6.3.4) to compute the stress associated with each spring and the contribution of each spring to the reacting moment M_t is calculated as required by equations 6.8, 6.9 and 6.10.
- If the normalised out-of-balance moment $|(M_t-M_a)/M_a|$ is smaller than a given tolerance then a new increment of cycles ΔN is applied and the procedure is repeated from the first step. If the tolerance limit is exceeded the increment of rotation $\Delta\theta$ has to be corrected according to a convenient type of nonlinear solution procedure (Newton-Raphson for example) and the numerical solution returns to the second step, where the increment of rotation $\Delta\theta$ is guessed, without increasing the number of cycles.
- The solution ends when the current number of cycles N reaches the specified maximum value N_{tot}.

6.3.6 Examples of fatigue behaviour prediction

Once the program was implemented, some examples were generated and compared with reference [L08]. Those examples were generated with the cylinder model, characterized by the following parameters:

- R=100 mm
- G_c=0.26 N/mm
- δ_c=0.017333 mm

The value of the critical moment per unit width can be calculated using equation 6.12, and it is M_c=26 Nmm/mm.

For the first examples the bilinear constitutive law with the stiffness degradation based damage is used. Therefore the value of σ_0 is calculated as 30N/mm^2 and the value of δ_0 is set at 10^{-6} mm.

The parameters of the fatigue law, as described in reference [RGTBV05], have to be determined to reach a good fit to the Paris law. In that reference the following values were determined using a FE implementation of the interface fatigue degradation strategy with the same bilinear interface law used in this thesis:

- C=2 x 10^{-6}
- λ=0.5
- β=2

For the cylinder model the distance between the springs (Δl) and the increment (ΔN) in the number of cycles were set, respectively, at:

- Δl=0.005mm
- ΔN=100

The performance of the cylinder model is investigated for a cyclic moment of amplitude M_a=0.2M_c. Firstly the moment is applied statically, the equilibrium position of the cylinder is determined and then the position of the cylinder as a function of the number of cycles is evaluated. The resulting value of x_{con}, which is the x-coordinate of the cylinder contact point, is shown, in figure 6.24(a), as a function of the number of cycles N.

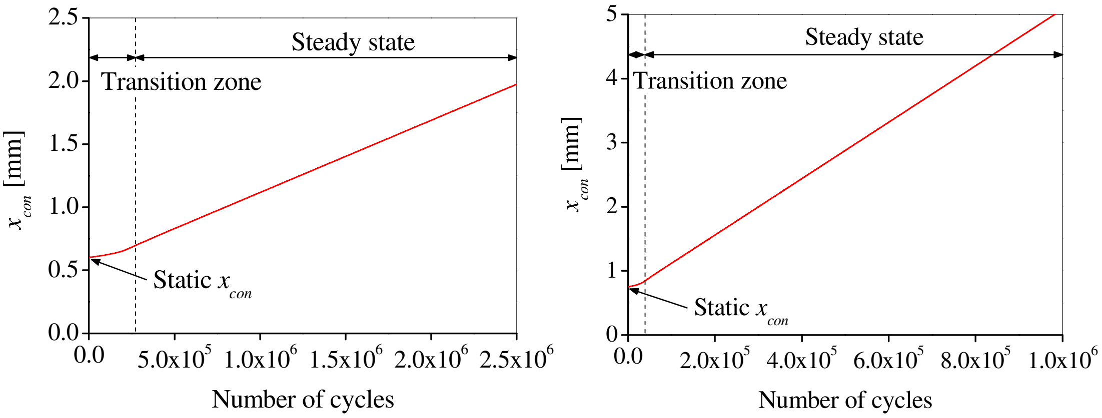

(a) (b)

Figure 6.24 - Crack length x_{con} for (a) $M_a = 0.2\ M_c$ and (b) $M_a = 0.3\ M_c$ using bilinear constitutive law with stiffness degradation damage. The vertical scales of (a) and (b) are different

It is possible to observe that at the beginning of the fatigue loading the cylinder displacement rate starts to grow slowly until it reaches a constant value.

This means that there is a transition zone from static to fatigue loading and then steady state fatigue behaviour is reached. In the steady state the fatigue growth rate is given by the slope (dx_{con}/dN).

The figure 6.24(b) is related, instead, to an applied moment increased to M_a=0.3M_c. In this case the initial static-only component of the displacement and the steady state crack growth rate are larger, as expected.

At this point the behaviour of individual springs is examined. In order to do so a spring located in the steady state zone is arbitrarily chosen and monitored. The relative displacement and stress values are plotted in Figure 6.25 for a range of values of applied moments M_a. For each value of M_a the area delimited by the stress-displacement curve is equal to the applied energy release rate (G_a) which can be derived in an identical way to equations 6.11 and 6.12 giving:

$$G_a = M_a / R \tag{6.65}$$

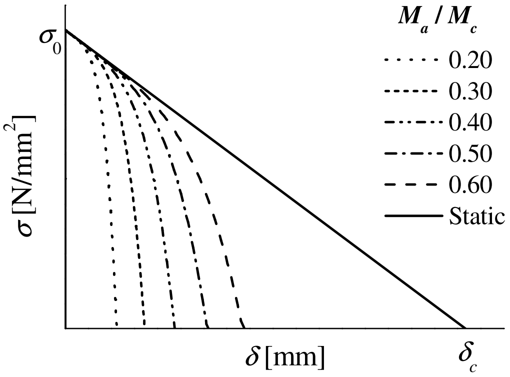

Figure 6.25 - Single spring behaviour under static and fatigue loading

The figure 6.26 shows the crack growth rate (dx_{con}/dN) for a range of values of the applied moment, plotted in a log-log scale, against (M_a/M_c) and the result is very close to the straight line form of the Paris law.

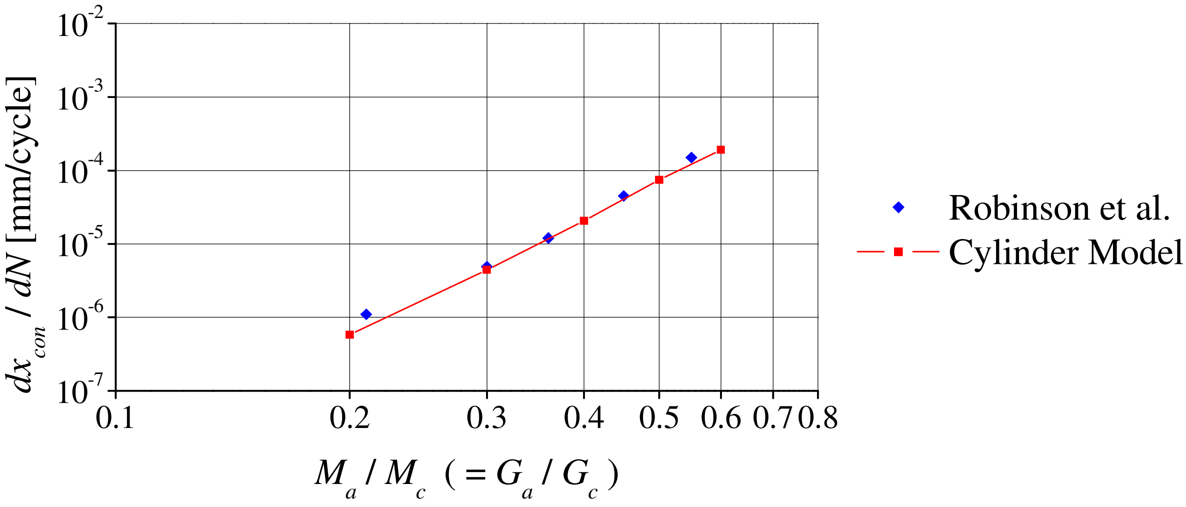

Figure 6.26 - Comparison of the results of Robinson et al. [RGTBV05] with the ones obtained using the cylinder model

In the figure 6.26 are also shown the results predicted with a FE model for a fatigue loaded DCB specimen using the same interface and degradation parameter values [RGTBV05]. It can be seen there is a good agreement between the two implementations.

Paris plots can be obtained by adopting any of the constitutive laws and damage definitions introduced previously. However to achieve similar Paris plots the values of the parameters of the fatigue law have to be changed according to table 6.1.

	C	β	λ	μ
Bilinear law, stiffness-degradation damage	2×10^{-6}	2.0	0.5	0.7
Polynomial law*, stiffness- degradation damage	2.94×10^{-1}	5.5	0.5	0.7
Bilinear law, 'energy consumed' damage	6.35×10^{-2}	2.9	0.5	0.7
Bilinear law, 'work done' damage	2.78×10^{-2}	2.65	0.5	0.7
*The values of the constitutive parameters for the third order polynomial law are: G_c=0.26N/mm, δ_c=0.017333mm.				

Table 6.1 - Parameter values of the fatigue law to be adopted with the different constitutive laws or damage definitions in order to obtain similar Paris plots

6.3.7 Estimation of parameter sensitivities

This paragraph shows how the cylinder model can be used to evaluate the performance of interface elements with the different constitutive laws and damage definitions introduced in the past sections.

In particular the sensitivity of the model is investigated by varying two important discretisation parameters, Δl and ΔN. The best performing formulation will be the one which will allow the largest values for Δl and ΔN with the smallest variation in the slope of the curve x_{con} vs. N, which is the curve shown in figure 6.24.

The value of the applied moment chosen was $M_a = 0.2\ M_c$ and the 'exact slope' ($\mathrm{d}x_{con}/\mathrm{d}N$) was computed using a small value of Δl, equal to 0.005 mm, and a small value of ΔN, equal to 100. The fatigue law parameters were set as shown in table 6.1, in order to provide the same Paris plot for all four investigated formulations. The value of the 'exact slope' is approximately the same for all four formulations of table 6.1.

After a few preliminary simulations it was decided to investigate the behaviour of the different formulations in the parameter field defined by the following ranges:

- $0.005\text{mm} < \Delta l < 0.2\text{mm}$;
- $100 < \Delta N < 60000$.

The range of Δl values has been divided in 200 uniform subintervals and the range of ΔN values in 600 uniform subintervals so that 120000 different parameter combinations have been considered for each constitutive law.

In figure 6.27 is shown a comparison between the performance of the bilinear constitutive law and of the polynomial constitutive law, both with the stiffness degradation static damage definition.

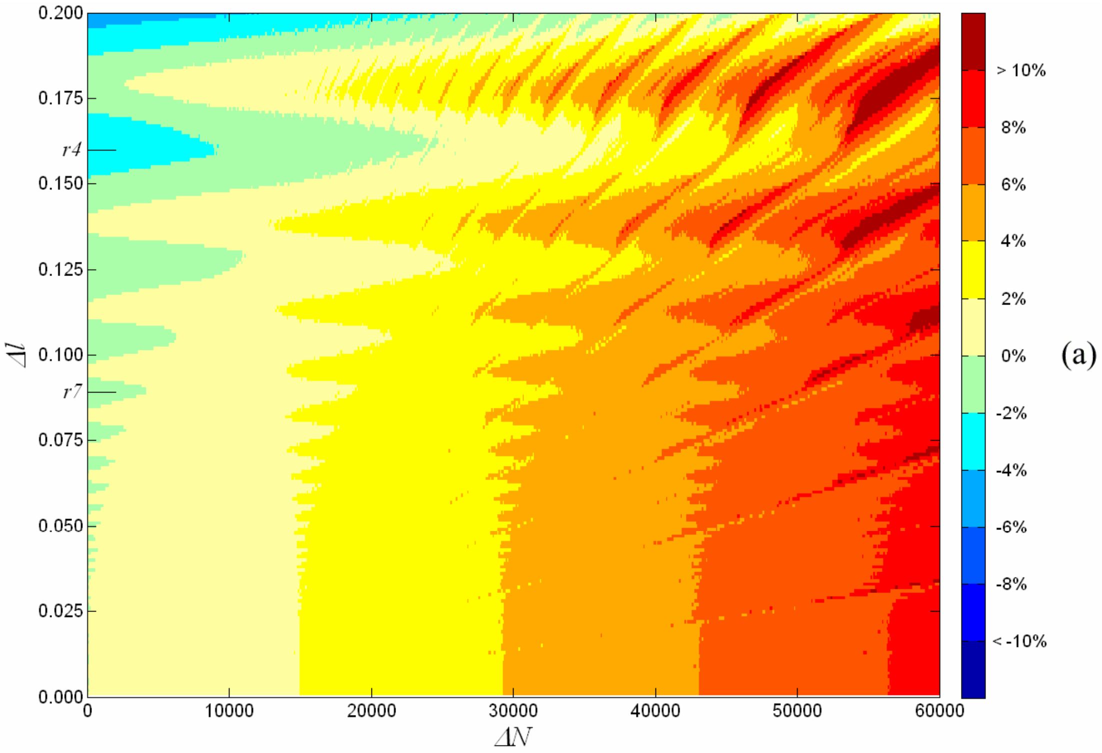

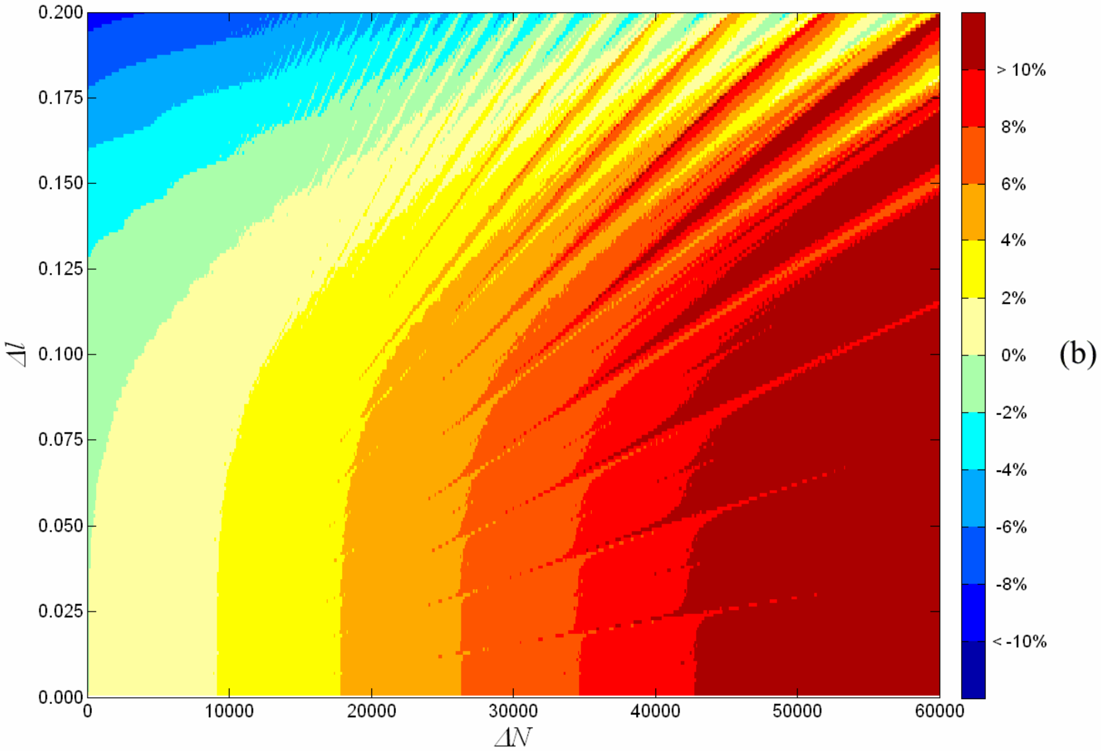

Figure 6.27 - Error plots for (a) bilinear and (b) polynomial constitutive laws with stiffness degradation damage. The two short horizontal lines in (a) indicate two integer values of the ratio ($l_d/\Delta l$)

Different colours represent different errors in the computed slope with respect to that of the ‘exact solution’. For every formulation the error is computed with respect to the ‘exact slope’ of that formulation.

Some interesting features can be observed in figure 6.27 and they are highlighted in figure 6.28. The first feature is the formation of vertical bands with increasing *ΔN* at low values of *Δl*. These bands go from low errors in the slope ($\mathrm{d}x_{con}/\mathrm{d}N$) on the left to higher errors on the right, where the slope computed is significantly greater than the ‘exact solution’, as it is possible to see in figure 6.27and 6.28. The bands simply indicate that for small *Δl* the error grows linearly with *ΔN*.

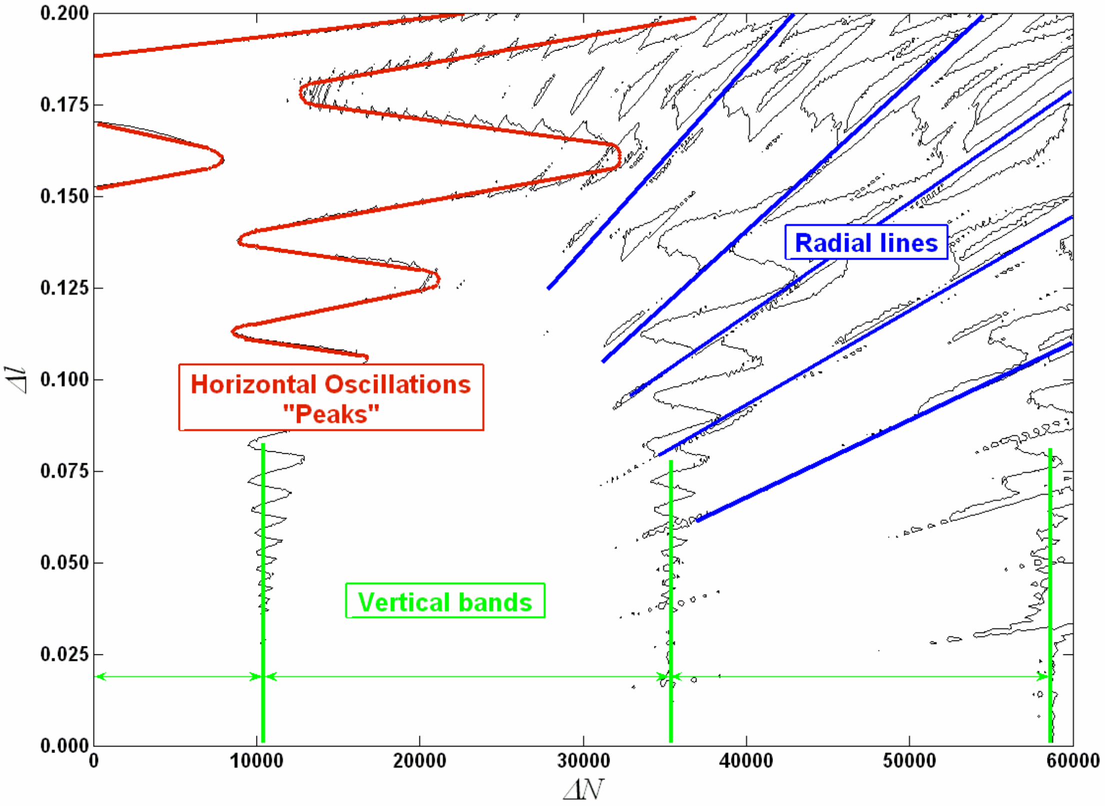

Figure 6.28 - Main features of the error plots shown in figure 6.27 and 6.29

A second feature that it is possible to observe, particularly in figure 6.27(a), as Δl increases, is that the vertical bands are broken up by oscillations with amplitudes that increase with increasing Δl.

There is some indication that these oscillations depend on the occurrence of an integer number of Δl intervals between the position where $\delta = \delta_c$ (failure extension) and the contact point [L08].

For the example of figure 6.27(a) this distance l_a calculated for $\Delta l = 0.005$ mm is 0.66 mm.

Using these values, the positions of two integer values of the ratio $l_a/\Delta l$ are indicated in figure 6.27(a), using short horizontal lines, and they correspond approximately to peaks in the observed oscillations.

In particular, the r4 mark indicates a value of $l_a/\Delta l$ equal to 4 and the r7 mark indicates a value of $l_a/\Delta l$ equal to 7.

In the same way other peaks of the horizontal oscillations correspond to integer values of the ratio $l_a/\Delta l$.

The third feature that can be observed is the pattern of many radial lines that seem to converge to the origin of the plot. These lines are made of ‘better’ results that are embedded in zones of ‘worse’ ones. These lines blur into the horizontal peaks mentioned in the previous paragraph generating zones of ‘good’ results surrounded by ‘bad’ results.

Further analysis was done of these radial features [L08].

The main conclusion was that the ‘good’ results surrounded by ‘bad’ results do not correspond to reliable behaviour of the springs.

They simply represent zones of bad parameter values in which different sources of error cancel each other out to provide a good result.

It is evident, observing figure 6.27, that the polynomial constitutive law is more sensitive than the bilinear constitutive law to changes in Δl and ΔN.

In fact the vertical bands of figure 6.27(b) are narrower than those of figure 6.27(a), which means that for a given value of Δl the error associated to a value of ΔN is usually bigger for the polynomial constitutive law than for the bilinear constitutive law.

In general the small-error parameter combinations in figure 6.27(b) cover a smaller area than in figure 6.27(a). It can be concluded that the bilinear constitutive law is 'better' than the polynomial law.

At this point, after have observed the better performance of the bilinear constitutive law, it was decided to investigate this law with the two other static damage formulations proposed in section 6.2.5, the energy consumed based damage and the work done based damage.

The same investigation of the sensitivity of the model with respect to the two discretisation parameters, Δl and ΔN, was done, with the same modalities.

The error plots resulting from this last analysis, shown in figure 6.29, can be compared to those shown in figure 6.27(a).

There are similar features that can be seen, as previously observed in figure 6.27(a). The performance of the stiffness degradation damage formulation seems less sensitive to the parameter variations than of the two other damage formulations.

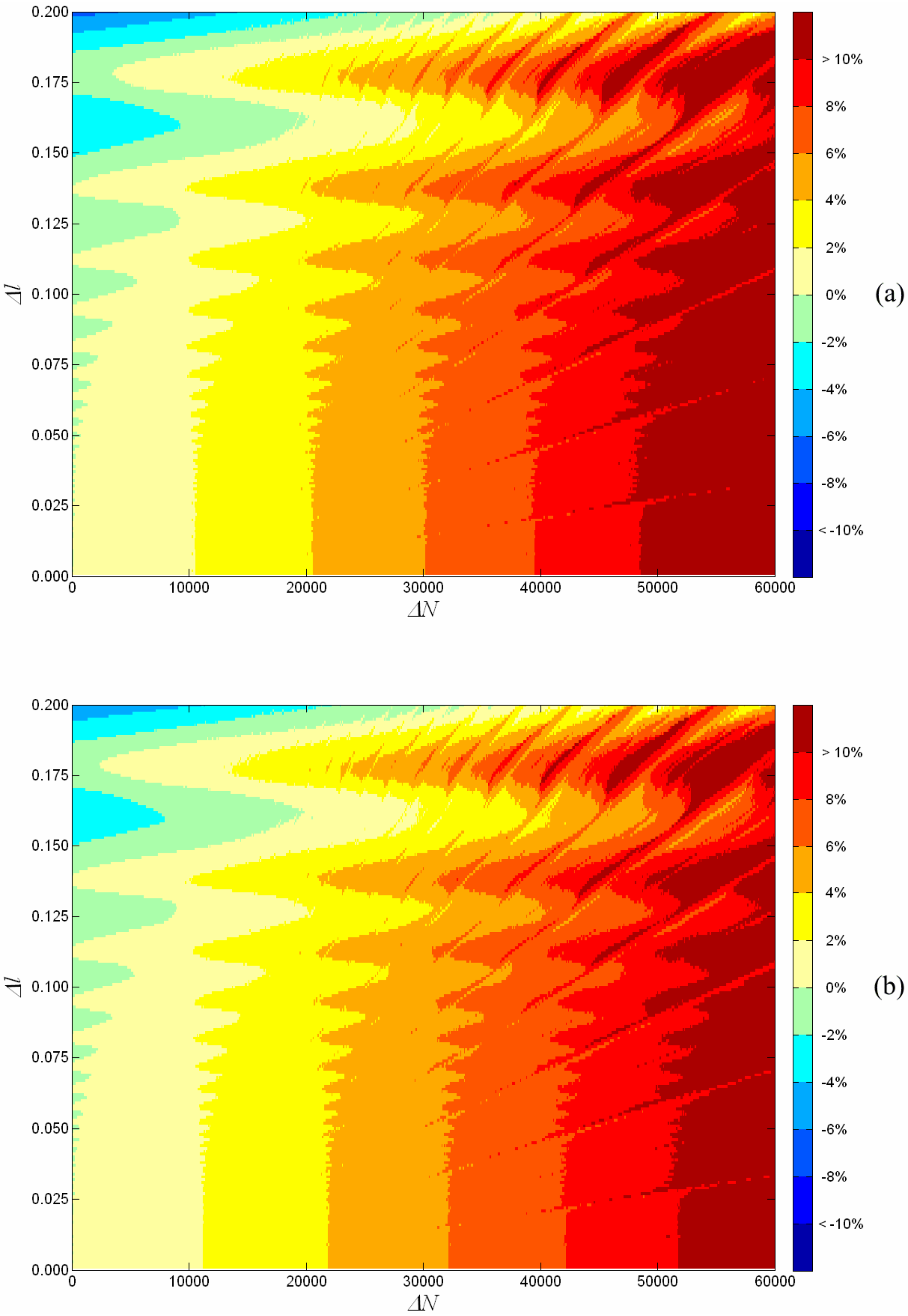

Figure 6.29 - Error plots for the bilinear constitutive law with (a) Energy consumed damage and (b) work done damage definitions

6.4 Comments

The cylinder model described and implemented in this chapter has shown to be a rational and fast method to evaluate the behavior of interface elements used to simulate fatigue crack propagation in composite materials.

This model is able to predict the delamination both under static and cyclic loading and its behaviour has been evaluated under both the conditions.

Under static loading the model has been evaluated with three different constitutive laws, a bilinear law, a mixed law and a third-order polynomial law. Each of the previous laws has been used with all the three formulations of the damage, stiffness degradation, energy consumed and work done.

For each of the previous laws, coupled with all the damage formulations, the rotation of the cylinder (directly related to the length of the crack) versus the applied load has been evaluated.

Other quantities were evaluated in a generic spring of the model: the damage parameter versus the displacement, the stress versus the displacement and the release energy rate versus the displacement.

In the static loading there is no difference in the global behavior of the model in dependence on the damage formulation, because, whichever is the damage formulation, the equation of the constitutive law globally does not change in the static problem.

There is instead a difference in the static behavior of the three constitutive laws. The bilinear and the mixed laws present a small difference in predicting the length of the crack, because they have the elastic branch in common. The polynomial law, instead, is quite different, because in it the damage starts from the beginning of the curve.

Moreover the model has shown that a rather large number of springs are required in the active area in order to have a good accuracy.

Under fatigue loading, instead, the model was evaluated with the bilinear law with all the three damage formulations and with the polynomial law with the stiffness degradation based damage, and one fatigue degradation strategy has been coupled to the various formulations.

In this case, the length of the crack versus the number of cycles has been evaluated for each law, but the main point of the analysis has been the sensitivity of the model with respect to two key parameters: the element length (represented by the distance between the springs) and the increment in the number of cycles between consecutive steps of analysis. As the obtained error plots showed, the bilinear constitutive law with the stiffness degradation damage formulation provides the best performance among all the tested formulations.

Chapter 7

Conclusions

This thesis is a dissertation focussing on some aspects of interlaminar delamination in fibro-reinforced composite materials. At the beginning, possible approaches to this problem are presented. This section examines the generality of fibro-reinforced composite materials and their delamination, with the modalities for approaching the study of the propagation of the delamination under quasi-static and cyclic loading.

The most relevant achievements reached in this thesis can be summarized as following.

First of all, experimental tests have been carried out on carbon fibre laminated for mode I (DCB test), mode II (4ENF test), and mixed mode (SLB test) loading.

Each test allowed evaluating the propagation of the delamination crack in the specimen with respect to the applied displacement and it allowed the calculation of the interlaminar fracture toughness for the mode I and mode II only.

The experimental tests showed accordance with the typical results of these tests and they can be considered a good starting point for the subsequent comparison with the finite element modelling with cohesive elements.

The finite element modelling carried out in this work allowed studying the potential of the cohesive interface elements for the prediction of delamination propagation under quasi-static loading.

The three modelled tests, DCB, 4ENF and SLB showed that a rather good accordance may be obtained between experimental data and numerical simulations with a proper choice of the main model parameters (critical fracture energies G_{IC} and G_{IIC}, interface stiffness and mesh density, in particular). The accordance has been evaluated with regard to both the force versus displacement curves and the displacement versus crack length curve.

Subsequently, the sensitivity to the cohesive stiffness interface has been evaluated for all the models with a parametric analysis with respect to the stiffness.

It has been shown that the response of the laminates analyzed is only slightly affected by the initial stiffness of the cohesive interface for the pure modes, whereas for the mixed mode the influence is small if the interface stiffness is reduced by dividing the values of both the two modes by the same quantity. Also the criterion chosen to describe the propagation of the delamination is important in the mixed mode. Therefore this model has been tested with a linear and quadratic law. The linear law showed a good accordance with the experimental tests, and then it was chosen also for its simplicity.

For the study of the delamination under fatigue loading, a simple cylinder model has been implemented and investigated. This model, for its simplicity, is very useful to compare, in a systematic, fast and rational manner, the behaviour of interface elements with different interface constitutive laws and damage formulations, both for static and fatigue delamination.

The response of the model has been evaluated under both static and fatigue loading.

Under static loading, the prediction of the propagation of the crack has been evaluated with three different constitutive laws: a bilinear law, a mixed law and a third-order polynomial law. Each of the previous laws has been used with all the three formulations of the damage, stiffness degradation, energy consumed and work done.

Under static loading there is no difference in the global behaviour of the model in dependence of the damage formulation, since, whichever is the damage formulation, the equation of the constitutive law does not change in the static problem.

There is instead a difference in the static behaviour of the three constitutive laws. The bilinear and the mixed laws present a small difference in predicting the length of the crack, because they have the elastic branch in common. The polynomial law, on the other hand, is quite different, since in this case the damage starts from the beginning of the curve.

Under fatigue loading, on the contrary, the model was evaluated only with the bilinear law with all the three damage formulations and with the polynomial law with the stiffness degradation based damage. One single fatigue degradation strategy has been coupled to the various formulations.

The model under fatigue loading has been evaluated with the different constitutive laws with respect to the prediction of the length of the crack, but especially with reference to its sensitivity to two key parameters: the element length and the increment in the number of cycles between consecutive steps of analysis.

The results produced by the cylinder model suggest that the bilinear constitutive law with the stiffness degradation damage formulation provides the best performance among all the tested formulations.

Altogether the dissertation about the delamination presented in this thesis has covered many interesting aspects of this problem, in consideration of the importance that fibre-reinforced composite materials have at present. The availability of numerical tools able to provide reliable predictions of delamination growth it is in fact nowadays extremely important in order reduce the experimental tests necessary to assess the safety of a structure.

References

[A94] ASTM St.. Standard test method for mode I interlaminar fracture toughness of unidirectional fiber-reinforced polymer matrix composites. *ASTM* **D5528-94a**.

[Ab] Abaqus release 6.5 documentation.

[AB86] C. G. Aronsson, J. Bäcklund. Damage mechanics analysis of matrix effects in notched laminates. *ASTM* **STP907** (Composite Materials: Fatigue and Fracture), *H. T. Hahn Ed.*, *American Society for Testing and Materials*, *Philadelphia*, 134-157, 1986.

[ACB02] D. F. Adams, L. A. Carlsson, R. Byron Pipes. Experimental characterization of advanced composite materials. *CRC*, **Third Edition**: 2002.

[ADMP06] F. Aymerich, F. Dore, D. Meloni, P. Priolo. Modellazione del danneggiamento da impatto in laminati compositi mediante elementi coesivi. *Associazione Italiana per l'Analisi delle Sollecitazioni (AIAS)*, *XXXV Convegno Nazionale*, *Università Politecnica delle Marche*: 13-16 settembre 2006.

[B04] N. Blanco Villaverde. Variable mixed-mode delamination in composite laminates under fatigue conditions: testing & analysis. *PhD thesis*, *Universitat de Girona*, *Dept. d'Engin. Mecànica i de la Constr. Industr.*: 2004.

[B62] G. I. Barenblatt. Mathematical theory of equilibrium cracks in brittle failure. *Advances in Applied Mechanics*, **7**: 1962.

[B87] D. Broek. Elementary engineering fracture mechanics. *Martinus Nijhoff Publishers*, 1987.

[CCKBMQ99] J. Chen, M. A. Crisfield, A. J. Kinloch, E. P. Busso, F. L. Matthews, Y. Qiu. Predicting progressive delamination of composite material specimens via interface elements. *Mechanics of Composite Materials and Structures*, **6**: 301-317, 1999.

[CD02] P. P. Camanho, C. G. Dàvila. Mixed-mode decohesion finite elements for the simulation of delamination in composite materials. *NASA/TM*-2002-**211737**.

[CDA01] P. P. Camanho, C. G. Dàvila, D. R. Ambur. Numerical simulation of delamination growth in composite materials. *NASA/TP*-2001-**211041**.

[CDD03] P. P. Camanho, C. G. Dàvila, M. F. De Moura. Numerical simulation of mixed-mode progressive delamination in composite materials. *J. of Composite Materials*, **37** (16): 1415-1438, 2003.

[CH06] S. Cauchi Savona, P. J. Hogg . Effect of fracture toughness properties on the crushing of flat composite plates. *Composites. Sci. Technol.*, **66**: 2317-2328, 2006.

[D60] D. S. Dugdale. Yielding of steel sheets containing slits. *J. of Mechanics and Physics of Solids*, **8**: 100-104, 1960.

[DAL95] L. Daudeville, O. Allix, P. Ladevèze. Delamination analysis by damage mechanics: some applications. *Composites Engineering*, **5** (1): 17-24, 1995.

[DS96] B. D. Davidson, V. Sundararaman. A single leg bending test for interfacial fracture toughness determination. *Int. J. Fracture*, **78** (2): 193-210, 1996.

[G21] A. A. Griffith. The phenomena of rupture and flow in solids. *Philosophical Transactions of the Royal Society of London*, *Series A*, **221**: 163-198, 1921.

[G90] E. E. Gdoutos. Fracture mechanics criteria and applications. *Kluwer Academic Publishers*, *Dordrecht*, *The Netherlands*: 1990.

[GRCL08] U. Galvanetto, P. Robinson, A. Cerioni, C. Lopez Armas. Evaluation of costitutive laws for the computer simulation of fatigue-driven delamination in composite materials. *Int. J. Fatigue*, **D-08-00277**: submitted Sep 10, 2008.

[K04] R. Krueger. Virtual crack closure technique: history, approach and applications. *Applied Mechanics Review*, **57** (2): 109-143, 2004.

[KO01] R. Krueger, T. K. O'Brien. A shell/3D modelling technique fort he analysis of delamined composite laminates. *Composites Part A*: *Applied Science and Manufacturing*, **32** (1): 25-44, 2001.

[L08] C. A. Lopez Armas. Evaluation of costitutive laws for the computer simulation of fatigue-driven delamination in composite materials. *PhD thesis*, *Imperial College of London*, *Dept. Aeronautics*: 2008.

[LC94] J. Lemaitre, J. L. Chaboche. Mechanics of solid materials. *Cambridge University Press*, *Cambridge*: 1994.

[LGR07] C. A. Lopez Armas, U. Galvanetto, P. Robinson. A simple model for the evaluation of fatigue degradation laws for interface elements. *16th International Conference on Composite Materials*, *Kyoto – Japan*: 2007.

[MGR06] J. J. Muñoz, U. Galvanetto, P. Robinson. On the numerical simulation of fatigue driven delamination with interface elements. *Int. J. Fatigue*, **28**: 1136-1146, 2006.

[N87] A. Needleman. A continuum model for void nucleation by inclusion debonding. *Journal of Applied Mechanics*, **54**: 525-531, 1987.

[O98] T. K. O'Brien. Composite interlaminar shear fracture toughness, GIIC: shear measurement of sheer myth?. *ASTM* **STP1330-98**: 3-18.

[PAM06] P. Priolo, F. Aymerich, D. Meloni. La delaminazione nei compositi: prospettive e limiti di metodi locali ad elementi finiti. *Associazione Italiana per l'Analisi delle Sollecitazioni (AIAS)*, *XXXV Convegno Nazionale*, *Università Politecnica delle Marche*: 13-16 settembre 2006.

[PBDG00] R. H. J. Peerlings, W. A. M. Brekelmans, R. de Borst, M. G. D. Geers. Gradient-enhanced damage modelling of high-cycle fatigue. *Int. J. Numer. Meth. Engng.*, **49** (12): 1547-1569, 2000.

[PE63] P. Paris, F. Erdogan. Critical analysis of propagation laws. *Journal of Basic Engineering*, **85**: 528-534, 1963.

[PGA61] P. Paris, M. Gomez, W. Anderson. A rational analytical theory of fatigue. *Trend in Engineering*, **13**: 9-14, 1961.

[PIR06] S. T. Pinho, L. Iannucci, P. Robinson. Formulation and implementation of decohesion elements in an explicit finite element code. *Composites Part A*: *Applied Science and Manufacturing*, **37** (5): 778-789, 2006.

[R68] J. R. Rice. A path independent integral and the approximate analysis of strain concentration by notches and cracks. *J. of Applied Mechanics.*: 379-386, 1968.

[R92] J. R. Reeder. An evaluation of mixed-mode delamination failure criteria. *NASA/TM*-1992-**104210**.

[R93] J. R. Reeder. A bilinear failure criterion for mixed-mode delamination. *ASTM* **STP1206-93** (Composite materials: testing and design).

[RGTBV05] P. Robinson, U. Galvanetto, D. Tumino, G. Bellucci, D. Violeau. Numerical simulation of fatigue-driven delamination using interface elements. *Int. J. Numer. Meth. Engng.*, **63**: 1824-1848, 2005.

[RK77] E. F. Rybicki, M. F. Kanninen. A finite element calculation of stress intensity factors by a modified crack closure integral. *Engineering Fracture Mechanics.*, **9**: 931-938, 1977.

[S05] A. Szekrényes. Delamination of composite specimens. *PhD Dissertation*, *Budapest University of Technology and Economics*, *Dept. Appl. Mechanics*: 2005.

[SU04] A. Szekrényes, J. Uj. Beam and finite element analysis of quasi-unidirectional composite SLB and ELS specimens. *Composites Sci. Technol.*, **64**: 2393-2406, 2004.

[T03] T. E. Tay. Characterization and analysis of delamination fracture in composites: an overview of developments from 1990 to 2001. *Applied Mechanics Review*, **56** (1): 1-32, 2003.

[T06] A. Turon Travesa. Simulation of delamination in composites under quasi-static and fatigue loading using coesive zone models. *PhD thesis*, *Universitat de Girona*, *Dept. d'Engin. Mecànica i de la Constr. Industr.*: 2006.

[YH90] S. H. Yoon, C. S. Hong. Modified end notched flexure specimen for mixed mode interlaminar fracture in laminated composites. *Int. J. Fracture*, **43**: 3-9, 1990.